# Some geological implications of the flow of clay-water mixtures

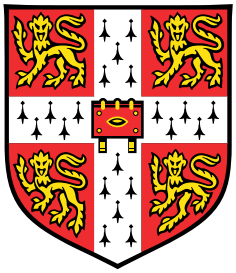

**Stefano Rocco**

Department of Earth Sciences
University of Cambridge

This dissertation is submitted for the degree of
*Doctor of Philosophy*

Wolfson College

January 2018

To my mother, father and brother ...

# Declaration

I hereby declare that except where specific reference is made to the work of others, the contents of this dissertation are original and have not been submitted in whole or in part for consideration for any other degree or qualification in this, or any other university. This dissertation is my own work and contains nothing which is the outcome of work done in collaboration with others, except as specified in the text and Acknowledgements. This dissertation contains fewer than 275 numbered pages of which not more than 225 pages are text, appendices, illustrations and bibliography

Stefano Rocco
January 2018

# Acknowledgements

This thesis is the conclusion of four years work, which would have not been possible without the help of a great many people. All of who I am grateful to.

Firstly I would like to thank my supervisor Professor Andrew Woods, for the time taken and help given to me during our many meetings. His advice and expertise have deeply contributed to my work, and also shaped and developed my research skills. I would also like to thank Jon Harrington and Simon Norris, their opinions and suggestions were held in high regard and have helped shape this thesis.

The whole project is based on experimental results which would have not been possible without the help of the BPI staff, in particular thanks to Andrew Pluck, Lotty Gladstone, Chris Richardson and Dudley Simons. I would also like to thank my colleagues and friends, our "deep" and "meaningful" conversations about fluid-dynamics and foreign politics during elegant wine tasting evenings or the occasional "quick" pint have made my work so productive especially the following mornings. Particular merit goes to Neeraja Bhamidipati, Joanna Starkie, Peeradon Samasiri, Merlin Etzold and Fin Allen.

I have to acknowledge my field work team Peter Dudfield, Richard Alloway, Martin Lippert, Tim Beeson-Jones and Marcus Horsley. Our cultural studies in the French Alps and in the surroundings of Copenhagen have taught me things that I will (regrettably) never forget. A special thank goes to my English tutors Finn Box and Marcus Horsley, without their influence my English grammar would be much worse than it already is (although I would probably be a much better human being).

My Italian crew in Cambridge: Alessandra Navarro, Nicoletta Bruno, Elisa Pandolfi, Gloria Liguori, Katerina Katsarou (not much of an Italian), Francesco Giove and Cristian Lella. They made me feel at home in a country where is legally acceptable to eat pineapple pizza. Also without the work of important people like Gennaro Dello Ioio and Carlo Greco, I would have probably never started a PhD in Cambridge so I need to thank them (or possibly blame them).

I would also like to thank the Cantabs rugby team, my housemates, and all my friends for looking after (not always with success) my physical and mental health during my PhD.

I finally want to thank Chloe for being by my side when it was most needed.

# Abstract

This thesis investigates three problems in the general area of environmental fluid mechanics. The first two problems are related to liquid or gas flow through clay-water suspensions, with relevance for the underground storage of radioactive waste and also for understanding the mechanism of eruption in mud volcanoes. The third problem centres on the different problem of mixing in a turbulent buoyant plume.

First, the injection of gas and water from a central source into a two-dimensional layer of clay confined between two circular horizontal plates is investigated. This provides a model of the potential pressurisation and failure of the seal rock around a radioactive waste repository as may arise if gas is continuously generated in the repository. As the gas injection pressure is gradually increased the cell walls deform and the clay moves radially outwards. However, at a critical radius, the liquid-clay interface becomes unstable and a series of channels propagate through the clay. When one of the channels reaches the edge of the domain the gas escapes and the pressure is released. As a result, the domain relaxes by elastic deformation and the clay seals the channel. In this way, continuous fluid injection leads to episodic release of gas from the cell.

The second problem concerns the flow of mud along a vertical conduit driven by the combined effect of reservoir pressure and buoyancy associated with the gas injected at the base of the conduit. This represents an analogue model of the eruption of a mud volcano, in which mud rises from a deep reservoir to the surface. I find that the pressure associated with the reservoir and any buoyancy force produced by the migration of gas from deep in the reservoir to the surface leads to a continuous eruption if the net pressure is greater than the yield stress of the clay. If the reservoir pressure falls during such an event, the eruption will eventually stop, once the pressure reaches a dynamic yield stress condition. Only later, if the reservoir pressure increases to the static yield stress of the clay will the eruption start again, and this can lead to a series of eruption cycles which depend on the non-newtonian rheology of the clay. In contrast, if this pressure is smaller than the yield stress of the clay, a series of episodic gas burst events can occur until the conduit is cleared of mud.

The third problem relates to the mixing in a turbulent buoyant plume. Through a series of new experiments and some complementary theoretical modelling I show that the mixing in a turbulent plume is strongly affected by the eddies and leads to significant longitudinal dispersion in the flow. The implications of the modelling for determining the residence time distribution of the fluid in the plume is discussed.

# Publications

The work discussed in chapters 2 and 4 has been summarised into two papers which have been published in peer-reviewed journals. The papers are as follows:

- Rocco, S., Woods, A. W., Harrington, J. and Norris, S. (2017). An experimental model of episodic gas release through fracture of fluid confined within a pressurised elastic reservoir. *Geophysical Research Letters,* 44(2):751-759.
- Rocco, S. and Woods, A. W. (2015). Dispersion in two-dimensional turbulent buoyant plumes. *Journal of Fluid Mechanics,* 774, R1.

# Table of contents

# List of figures

# List of tables

# Chapter 1

# Introduction

This thesis investigates the dynamics of clay water mixtures and their displacement by gas in the context of a clay barrier rock or in the context of mud volcanoes. The motivation and area of interest are described in §1.1 while the structure of the thesis is described in §1.2. The thesis is based on new experimental results and consists of three main topics. The flow of gas or water in a clay domain is initially studied with particular application to engineered barriers for radioactive waste disposal. The discussion then focuses on buoyancy driven gas flow through a clay-water mixture and the flow of clay-water mixtures through a narrow conduit driven by pressurisation of the fluid or a gas flux. Such flows are naturally experienced during mud volcano eruptions. Finally the thesis explores dynamics of mixing of a release of buoyant gas into the atmosphere. The density difference leads to formation of a plume and we examine the buoyancy driven mixing between the fluids. Turbulent plumes are separately introduced in §1.3.

## 1.1 Motivation

Gas and water migration in clay based soils and rocks or clay mixtures are extremely interesting and occur in a wide range of subjects such as environmental engineering, soil mechanics, marine science, petroleum geology, $CO_2$ geological storage (Cevatoglu et al. [13]) , waste management and environmental engineering.

The project discussed in the following chapters is an experimental analysis of fluid migration in a clay-like matrix aiming to investigate the pathways of the fluids involved. Knowledge of gas migration in clay-water mixtures is particularly important for planning the design of radioactive waste repositories and also in enhancing our understand of the dynamics of mud volcanoes. In the case of radioactive waste disposal

the gas produced by decomposition of organic material may affect the efficiency of the engineered barrier causing the leakage of products harmful for the environment. Eruptions of mud volcanoes are also characterised by the combined flow of gas, mainly methane, and mud breccia originated from deep underground reservoirs (Dimitrov [21]). The pressurization of the reservoir combined with any background gas flow affect the eruption pattern of the volcano. The following sections include a brief description of radioactive waste disposal (§1.1.1) and mud volcanism (§1.1.2).

§1.1.3 summarises some of the properties of clay relevant for the work in this thesis. As described by Graham et al. [26] , fluid migration in clays may arise through different processes including advection, diffusion, deformation and fracturing. In each situation the dominant pathway is controlled by the fluid pressure and soil composition. This project focuses on advection and fracturing of clay with particular interest in the effect of the yield stress on the flow. Pneumatic and hydraulic fracturing are common phenomenon in clay. These have been analysed experimentally (Alfaro and Wong [2], Chang and Huang [14]) and numerically (Brown [10]) but the high pressure required for fracturing highly compacted material is usually too high to allow direct visualisation of the experiment. Using high water-concentration clay mixtures at atmospheric pressure, the present experiments allow to track the transition in behaviour between the liquid and plastic regimes (Holtzman et al. [30]). The results provide complementary information about how more highly compacted material may react to fluid pressurisation.

### 1.1.1 Radioactive Waste disposal

Nuclear power plants are an effective energy production system and there is great interest in nuclear energy especially given the challenge of global warming associated with the production of carbon dioxide from burning fossil fuels. One of the main issues with nuclear energy is the discharge of products because of the high risk of radioactivity and chemical toxicity. According to the level of radioactivity the waste products can be divided into high level waste (HLW), mainly consisting of the reaction fuel and reaction products, and intermediate level waste (ILW), which present a lower risk for the environment but still need to be managed with care (Delage et al. [20]). These waste products need to be kept in isolation for about $10^6$ years before the radioactivity decays to a negligible level and during this period it should be contained in absolute isolation. The geological disposal in subsurface repositories is the preferred solution to dispose of radioactive waste in the United Kingdom.

Although the specifics of each repository may vary for different nationalities, the general concept of geological disposal is based on a multiple barrier system so that

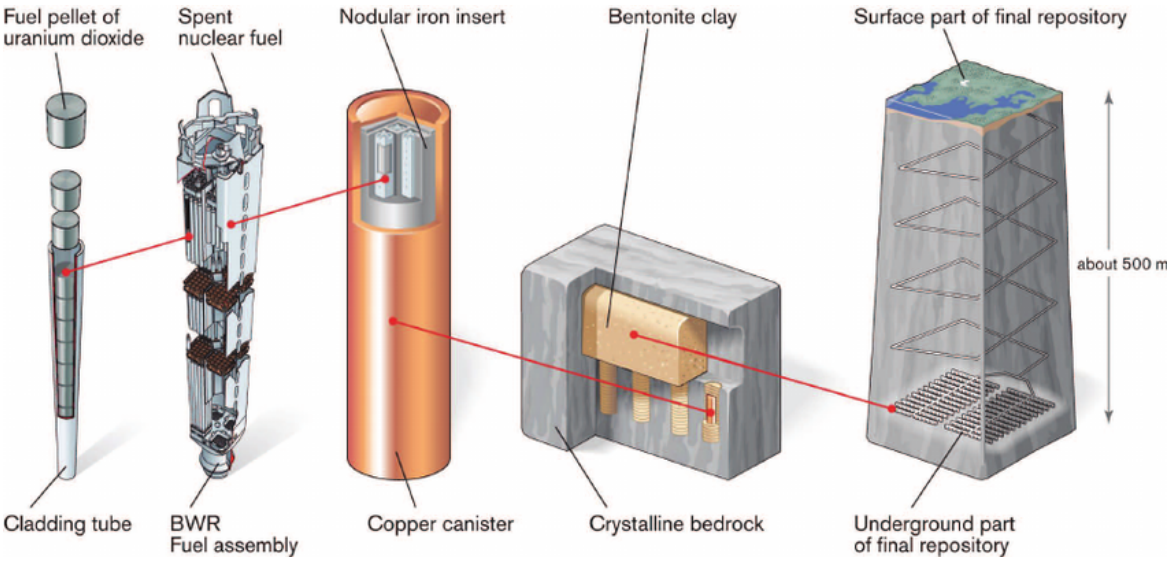


Fig. 1.1 The KBS3 concept used in Sweden and Finland. Metal and copper canister containing the radioactive fuel are placed in 500 m deep galleries and back-filled in clay. Image published in Sellin and Leupin [69].

when one system deteriorates or fails the next one comes into effect (Sellin and Leupin [69], figure 1.1). HLW is compacted into high density ceramic pellets, which is durable, resistant to high temperature and does not dissolve in water. It is then sealed in a strong corrosion-resistant metal bundle (about 30 pellets in each bundle). The external container consists of 2 layers, the inner is a 100 mm thick steel laminate, able to resist high pressures, and the outer layer, 50 mm thick, is made of a particular copper especially resistant to corrosion; this container can remain intact for $10^5$ years. The containers are stored in holes placed along a web of galleries excavated about 500 meters below the surface and then buried in clay in order to keep it protected from natural events or human intrusion. The use of clay as a seal between the canister and the rock is useful to protect the canister from water intrusion and in limiting the displacement of radionuclide in case of failure of one of the containers. For these reasons it is necessary for the clay to have low hydraulic permeability and to have self sealing abilities. This concept for radioactive waste management has already been demonstrated to be effective in natural environments such as Cigar Lake in Saskatchewan, where natural uranium deposits buried under 500 m clay rock showed no trace of radioactivity on the surface (Cramer and Smellie [16]).

My project focuses particularly on the effectiveness of clay as a seal in such repositories. I have particular interest in the possible intrusion of gas and water into the systems and how this might affect the seal efficiency. In the KBS3 concept

(Figure 1.1) the container is buried in the hole using bentonite clay and then the gallery is sealed with a mixture of bentonite, sand and water. Pure bentonite and a mixture of bentonite and sand are the most common material for such seal material because of its low conductivity (conductivity coefficient=$10^{-14}$ m/s) and diffusivity (diffusion coefficient $10^{-12}$ $m^2$/s), and high thermal conductivity but also for its swelling properties (Komine and Ogata [35]). Bentonite-sand mixtures are usually placed in non saturated blocks. The ingress of water to these blocks leads to swelling which fills the gaps around the canister and the seal in the rock (Pusch [64]). The possible decay of organic waste products, corrosion of steel and radiolysis of water over time may lead to gas production. This can increase the pressure in the repository which may eventually fracture the clay and compromise its sealing efficiency. In order to generate a robust safety case, it is key to have a good understanding of the interaction of fluids with clay. This is the aim of this research. It is also important to note that the clay is subject to many other challenges in terms of being an effective seal (Sellin and Leupin [69]) including non uniform water absorption (Delage et al. [20]), freeze-thaw cycles, rock movements and heating from radioactive decay which are still the subject of research.

### 1.1.2 Mud Volcanoes

Mud volcanoes are geological phenomena which result from the eruption of clay-like material and gas originating from a source reservoir about 1 Km deep in the ground. Although mud volcanoes present with several different surface structures, composition and eruption styles it is possible to track their generation to some common factors. The main source of mud breccia consists of a low density material (of order 1500 kg/$m^3$) buried under a thick layer of dense sediments (usually these sources are at least 1.5 km deep in the ground). The deep reservoir of mud and water may have possibly been caused by water intrusion and rapid overloading resulting from tectonic activity, as most mud volcanoes are located along compressional belts characterised by frequent tectonic activity and deep aquifers (Shirzaei et al. [73]). During a mud volcano eruption, mud is pushed to the surface through a main vent and some satellite vents by buoyancy, pore fluid pressure, tectonic compression and gas generation (Kopf [37]). The mud outflow is always accompanied by gas release which accumulates in the deep reservoir, and increases the pressure of the reservoir. For this reason mud volcanoes are often considered as effective markers of an oil or natural gas reservoir. The sum of these factors may cause passive eruptions with a uniform and constant release of gas, or random violent eruptions with frequent ignition of the emitted gas.

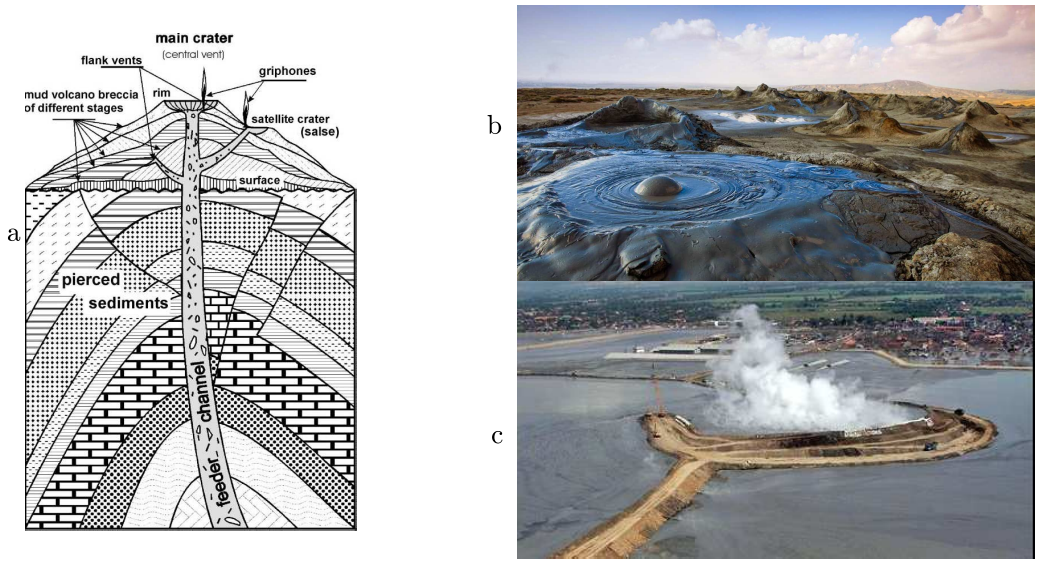


Fig. 1.2 (a) Schematic of a generic mud volcano structure (image published in Dimitrov [21]). (b) Image of the slow extrusion of mud in the Gobustan National Park in Azerbaijan (image downloaded from http://www. discoverazerbaijan.az/discover/discover-azerbaijan/mud-volcanos/ in 2017). (c) Eruption of the Lusi mud volcano, Indonesia (image downloaded from http://www.peoplenewstime.com/a-mud-volcano-has-been-erupting-since-11-years-in-indonesia/ in 2017).

It has been estimated that almost $10^{12}$ g/year of natural gasses (mainly methane) is released by quiescent and eruptive phases of mud volcanoes (Milkov et al. [51]). The mud breccia and gas erupted contain interesting geological information such as the composition of the underground soils and the nature and formation of geological layers overlapping the mud reservoir. The formation and fluid dynamics involved in mud volcano eruptions is the subject of extensive research. Previous works (Manga and Bonini [47] and Vona et al. [82]) have involved the study of the convection occurring during ascent of the mud from depth measurements of the mud rheology, such as yield stress and shear properties, and the size of clasts erupted. The driving force for the mud volcano eruptions is given by the buoyancy of the clay with the surrounding rock, the high pore pressure of the reservoir (Dimitrov [21]) caused by gas expansion, structural stresses and tectonic activity. The triggers of the eruptions are considered to be high pressure fracturing, fault generation and seismic activity.

The Lusi mud volcano in Indonesia is of special interest. Here occasional violent mud eruptions started in 2006 and it is still active with an average discharge of $10^5$ $m^3$/day of mud. The volcano has caused the evacuation of the local population and a total of £4 billion of damage (Mazzini et al. [50]). The Lusi eruptive episode has consisted of a continuous eruption phase which lasted for almost 4 months, followed by

a series of short eruptions which are randomly distributed in time. Previous literature has focused on the effects of external factors, such as earthquakes (Bonini et al. [7]) and internal factors, such as the mud rheology (Manga and Bonini [47] and Vona et al. [82]) in triggering the eruptions. Predictions of eruptions have been made bearing in mind the historical evolution of each system (Rudolph et al. [67]) combined with numerical modelling (Murton and Biggs [54], and Zoporowski and Miller [85]). In contrast the present work focuses on an experimental study of the effects of the reservoir pressurization, fracturing and gas intrusion in the vent in causing mud volcano eruptions as suggested by Mazzini et al. [50].

### 1.1.3 Bentonite clay

The clay used for the experimental analysis discussed in the following chapters is a mixture of bentonite and water. Bentonite is a clay consisting of smectites, principally montmorillonite, and minerals such as quartz, calcite and micas (Besq et al. [6]). Bentonite is an absorbent clay and is the main material used in the radioactive waste disposal industry (as described in §1.1.1). Bentonite is also frequently used as a drilling mud during borehole drilling (water, hydrocarbons, shale gas, radioactive waste and general geology) to lubricate and cool the drilling system and stabilise and seal the drilling cavity.

Depending on the water content of the mixture the solution may present liquid-like or gel-like physical properties. Relatively high bentonite content mixtures form hydrogen bonds with the water which arranges the clay platelets into a mesh and the material reacts to stress as a gel (Kawatra and Ripke [33]). A sufficient applied stress can partially break the bonding allowing the platelets to move; the gel then deforms and flows if the stress is high enough. Reducing the stress allows the clay to rebuild the mesh of platelets and strengthen. The high thixotropy of the material also influences its physical properties so that the critical stress to break the bonds vary with time. The minimum stress causing deformation and flow of the material is defined as a yield stress $\sigma_y$. In addition the clay mixture is shear thinning (the viscosity of the clay reduces with the magnitude of the applied stress). I am interested in exploring the reaction of the clay to pressure gradients applied to the clay mixtures. This may lead to a plastic flow regime or a fracturing regime (Marques [48]). The stress during the experiments is caused by water or gas injection into the clay.

Unsaturated clay mixtures are highly absorbent and the water intruding the platelet mesh increases the distance between the molecules causing swelling of the clay. This swelling property of the clay makes bentonite particularly useful for waste disposal and

the flow of water through the clay media is very interesting. The water absorption is not necessarily homogeneous throughout the material and may cause local tension of the material affecting its mechanical behaviour. Also high water flow rates may cause hydraulic fracturing of the material and erosion (Baik et al. [3]).

As discussed by Graham et al. [26] and Marschall et al. [49] the gas flow through clays occurs with four main mechanisms:

- two-phase advective flow;
- fissuring and hydraulic fracturing;
- deformation of the pores of the clay;
- gas diffusion.

The experiments focus on the first two mechanisms and neglect the last two as the gas flow rate associated with those mechanisms is low compared to the gas injection flow rates used during the experiments. Fracture propagation through bentonite due to gas injection has been subject of experimental projects (Donohew et al. [22]) and numerical modelling (Brown [10]). The results suggest that the flow is dominated by gas pressurisation but the mechanism of gas propagation through the clay requires further investigation. The experiments discussed in §2 use a high water content mixture and the clay is between the liquid and plastic regime. The water-rich clay has been used to run some low pressure experiments in order to have visual information of the degassing pattern of clay. The clay within the plastic regime showed rheological properties (yield stress and shear thinning behaviour) similar to water-poor clays used in radioactive waste repositories. The results of these experiments gave a further insight of the behaviour of pneumatic and hydraulic fracturing within significant drier clays.

## 1.2 Fluid flow through clay

As described by Brown [10] gas injection into clay exhibits an entry pressure threshold which identifies when gas first penetrates into the clay (Figure 1.3 ). Cyclic gas injection on the same specimen shows similar behaviour but the threshold entry pressure decreases on successive gas injection phases, suggesting that the clay does not fully heal during the period between successive gas injection phases (Horseman et al. [31]). The sealing process is not fully understood, especially the time required for the entry pressure to return to the undisturbed value. The high pressures involved

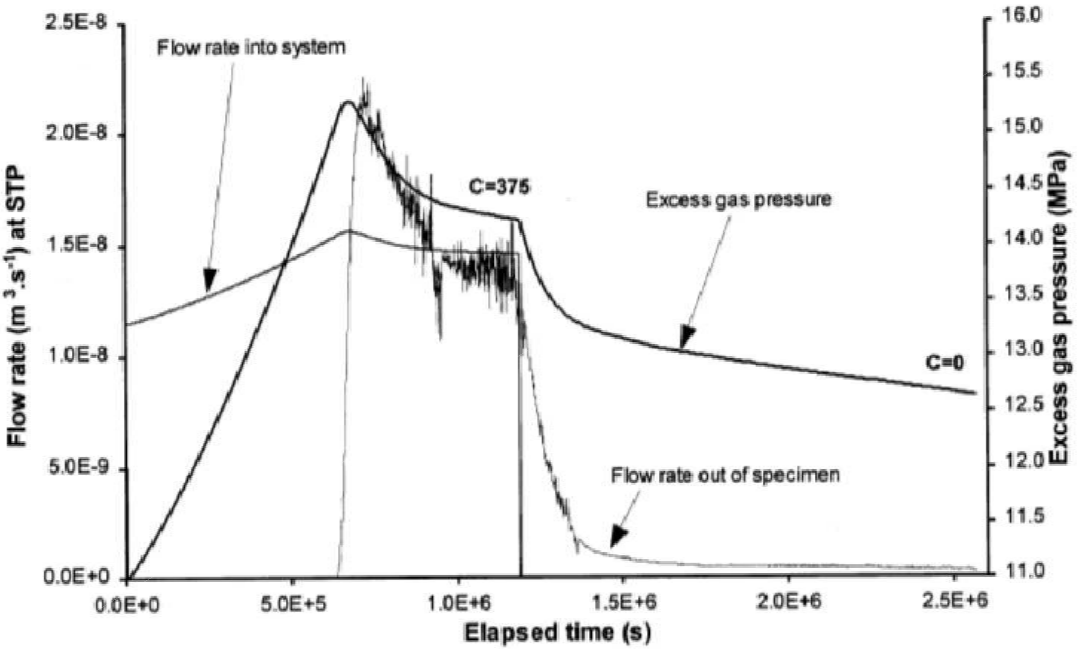


Fig. 1.3 Plot of the data obtained during a gas injection into a clay core published by Horseman et al. [31].

and the complexity of the process do not allow direct visual observations of the gas penetration so inferences about the gas migration process are made from indirect data such as the flow rate and gas pressure evolution with time. **Chapter 2** describes a series of new experiments at much lower pressures where it is possible to observe the process by which gas migrates through clay in detail. By analogy, this provides some insight into gas intrusion into high density clays. The injection of gas or water into the centre of a Hele-Shaw cell filled with a bentonite-water mixture leads to an increase in the pressure in the domain. The pressure deforms the plates of the Hele-Shaw cell and displaces the clay forming a hole at the injection point. The continuous injection of gas increases the pressure and the gas volume of the hole enlarges by further deforming the top plate and displacing the clay further from the injection point in an axis-symmetric deformation. When the pressure reaches a critical value channels develop in the clay which allow the gas to expand in the direction of the edge of the domain.

The unstable pattern differs from viscous-fingering (Paterson [58]), for high water content clay mixtures, to fracture-like channels for thicker clays. The onset of the deformation depends on the water content of the clay. Once the unstable channel reaches the edge of the domain, the pressure is released and the elastic top plate relaxes. The relaxation of the top plate displaces the clay, re-sealing the initial fracture. The

continued gas injection increases the pressure in the domain fracturing the clay and the cycle repeats. After each cycle the clay is weakened. The gas therefore requires gradually lower pressure on each successive cycle to fracture the clay. However the relationship between the pressure relative to this critical value and the gas volume collapse on a common profile for each cycle allowing development of a physical model.

The model of episodic release of a continuous source of gas has relevance for the periodic release of gas in the eruption of mud volcanoes. As discussed in §1.1.2 eruptions of mud breccia are a wide-spread phenomenon. The mud and gas erupted from mud volcanoes allow investigation of the underground geology (Kopf [37]) and the dynamics involved in the process (Manga and Bonini [47]). Extensive field work has enabled mapping of these geological anomalies (Dimitrov [21]) and widens our knowledge about the physics involving volcanic eruptions. Reservoir pressure, gas migration and seismic activity are strongly linked and each play an important role in the physics of mud volcano eruptions (Kopf et al. [36]). The historic records of the Lusi mud volcano (Indonesia, Figure1.1) suggest that the eruption began with a continuous phase which lasted for about 11 weeks followed by more irregular pulsating events (Mazzini et al. [50]). While seismic activity clearly influences the outflow and affects the frequency of the pulsations there is still some uncertainty around the origin of the eruptions. From the work published by Shirzaei et al. [73] it follows that the Lusi eruptions are fed by a shallow source and a deep source which lead to some uncertainty about the pressurisation process and its mechanism.

**Chapter 3** explores the simultaneous effect of yield stress, reservoir pressure and gas flux through a vertical vent on mud eruptions. The discussion begins considering the flow which develops when gas is injected into a circular, two-dimensional cell filled with clay. The flow generated by the gas is recorded by video to determine the gas flow and clay displacement processes. The gas flow is strongly influenced by the water content of the mixture and for relatively fluid-like clays the gas rises through the clay as a series of buoyant bubbles. Increasing the consistency of the mixture changes the shape of the bubbles from almost circular into an elongated vertical slug shape. Further increase of the clay thickness causes the gas pressure to fracture the clay forming a vertical channel which rises to the top of the clay and releases the gas. For low rates of gas flow into the clay, the rising bubbles arrange themselves into a train with bubbles of uniform volume and a regular distance between successive bubbles. Increasing the gas flow rate reduces the distance between bubbles until the bubbles eventually begin to merge while rising through the clay.

The discussion then focuses on the results obtained during experiments with a pressurised vent. The gas is injected from the base of a vertical conduit filled with clay. Increasing the height of the reservoir storing the clay which is connected to the bottom of the conduit increases the hydrostatic pressure of the vent. Pressure gradients in excess of the yield stress displace the clay from the reservoir to the conduit driving the eruption. The eruption rate is further increased if a gas flow is supplied to the up-flowing stream of clay. Once the pressure is greater than the yield stress the eruption starts and the flow of clay drains the reservoir and leads to a decrease in the pressure. The data suggest that the yield stress gradually decreases from one eruption to the next. The gradual increase of the reservoir pressure once the eruption has stopped causes a cyclic eruptive activity. After identifying the regimes of the eruptive activity (dormant and active, Figure 3.22 ) a numerical model is described considering the influence of a gas flux and reservoir pressurisation on the eruption of mud volcanoes.

## 1.3 Turbulent plumes

**Chapter 4** focuses on a somewhat different problem related to turbulent plumes which develop from the release of high temperature and low density gas into the atmosphere. The formation of a plume is a phenomenon which occurs frequently in nature (Woods [83]). In §4.4 I present a series of new results concerning the mixing within a turbulent plume. This is important for quantifying the rate of reaction of material within a plume since it quantifies how quickly the fluid elements in a plume come into contact, and also the range of residence times of passive particles in the plume, relevant for modelling droplet size distributions.

A turbulent plume develops when a fluid of one density is injected from a source into a fluid with a greater density. The buoyancy of the injected fluid drives the flow through the environment in an unstable fashion and the eddies generated by the instability cause the mixing between the two fluids. A plume differs from a jet in terms of the driving force. While the jet is driven by its momentum at the source, the plume is driven by the buoyancy forces and the flow persists until the two fluid densities are the same (List [45]).

Buoyancy driven mixing is involved in various natural events. Volcanic eruptions generate gas plumes which rise from the vent entraining volcanic dust. The source of the plume in some cases is thermal, such as hydrothermal plumes and plumes beneath the ice in polar ocean, where the buoyancy is generated by a temperature difference

which locally alters the density of the fluid (Carazzo et al. [12]). Gas bubble plumes are caused by the formation or injection of gas in liquid such as gas sources from a sea or lake floor (Woods [83]). Buoyancy drives the mixing between fluids also in exhaust fumes and some reactors. The turbulent mixing generated by buoyancy is a topic of interest for both industrial and environmental problems (Paillat and Kaminski [56]).

The mixing occurring within plumes is of particular interest for environmental problems in which plumes may carry pollutants emitted from industrial processes into the atmosphere. Knowledge of the mixing within the plume may help in improving the efficiency of these systems. The mixing occurring in plumes is also of interest for natural ventilation processes, whereby hot air may be used to generate a natural ventilation in a confined environment (Li [44]).

The dynamics of turbulent buoyant plumes have been well studied (Morton et al. [53]). Plumes have a similar behaviour which is modelled by the conservation of mass, momentum and buoyancy (Morton [52]). The entrainment assumption (Turner [79]) describes the rate of mixing between the plume and ambient fluid but the local mixing within the plume produced by the eddies requires further investigations. In particular, the details of the mixing within the plume are less well characterised and this is the topic of chapter 4. The mixing within a plume is important in the case that a reaction occurs within the plume, as this mixing regulates the contact between the reactants. The mixing between the fluids is a topic of interest in both industrial and environmental applications.

Chapter 4 describes the longitudinal mixing within a plume investigated by applying a light attenuation technique to a systematic series of experiments to measure the change in concentration of a tracer with the plume, and from this to infer the mixing rate. This technique was used to study the mixing occurring in two-dimensional jets by Landel et al. [43]. The chapter discusses the mixing using a similar protocol but focuses on plumes. The description of the experimental apparatus follows a brief summary of the physics involved in buoyancy driven flows developed by Morton et al. [53] but in two-dimensions (Paillat and Kaminski [56]). The plume flow consists of eddies which rise from the plume source and cause the plume fluid to fluctuate about the vertical line of symmetry and mix with environmental fluid and other plume fluid. Variations in the rise speed between eddies often results in merging between consecutive eddies which causes the growth of the turbulence along the height of the plume. Analysis of the oscillation frequency and rise speed of the eddies allows a deeper understanding of the local turbulent mixing processes. The discussion is then concluded by formulation of a mathematical model for the longitudinal mixing where the turbulence is considered in

terms of diffusion coefficients (Vanderwel and Tavoularis [81]) measured by comparison between experimental data and a numerical model. This longitudinal mixing in a plume is important if we are modelling reacting particles in a plume for which the residence time distribution is required.

**Chapter 5** finally summarises the main results of the projects discussed in the preceding chapters and suggests some possible developments for future studies.

# Chapter 2

# An experimental model of episodic gas release through fracture of fluid confined within a pressurised elastic reservoir

## 2.1 Abstract

I present new experiments that identify a mechanism for episodic release of gas from a pressurised, deformable reservoir confined by a clay seal, as a result of the transition from bulk deformation to channel growth through the clay. Air is injected into the centre of a thin cylindrical cell initially filled with a mixture of bentonite clay and water. For sufficiently dry mixtures, the pressure initially increases with little volume change. On reaching the yield stress of the clay-water mixture, the lid of the cell then deforms elastically and an air-filled void forms in the centre of the cell as the clay is driven radially outwards. With continued supply of air, the pressure continues to increase until reaching the fracture strength of the clay. A fracture-like channel then forms and migrates to the outer edge of the cell, enabling the air to escape. The pressure then falls, the clay flows back towards the centre of the cell and seals the channel so the cycle can repeat. The phenomena may be relevant at mud volcanoes.

## 2.2 Introduction

Gas migration through clay is of considerable interest for environmental engineering, marine science, petroleum geology and soil mechanics. The accumulation and migration of gas through clay deposits can lead to mud volcano flows and release of bubbles on the sea-floor (Barry et al. [4]; Boudreau [8]) , and is relevant for the stability of methane hydrates and clathrates (Buffett [11]). One interesting application relates to the use of bentonite clay as a seal for geological disposal facilities, including radioactive waste repositories (Pusch et al. [65]) where it has been proposed that bentonite seal layers could confine the waste. A considerable body of research has explored the potential behaviour of such clay in geological waste repositories (eg. Madsen [46]; Komine and Ogata [34]), investigating the effects of temperature changes, controls on interactions of clay and pore water including suction pressures, and the mechanical and flow properties of the clay (Cui et al. [17]). However, in some cases, as water contacts disposed material in the waste inventory, gas may be produced, primarily by corrosion of metals and degradation of organic materials, leading to pressurisation and gas-clay interactions (Sellin and Leupin [69]). The dynamics and stability of such gas-clay interfaces are of considerable interest, especially if, over time, the gas pressure builds through continued production (Harrington and Horseman [29]; Shaw [71]).

Much of the research on the dynamics of gas migrating through clay has been carried out in high pressure systems, in which direct visualisation of the flow is extremely difficult, and the detailed motion of the clay and gas has been inferred by measurements of stress, porewater pressure, flux or gas breakthrough in opaque high pressure cells (Horseman et al. [31] and Gutierrez-Rodrigo et al. [27]). Such measurements have led to the generation of numerical models to describe the process of gas migration through clay (Shao et al. [70]) although there are relatively few direct measurements of gas migrating through clay. As a complement to this body of work, I have developed a simplified experimental model to explore the processes that arise when gas is injected into the centre of a thin cylindrical cell initially filled with a clay-water mixture. These experiments explore the response of the clay-water mixture to pressurisation and displacement by the gas. Although the experiments are conducted at relatively low pressures, of the order of 1 atmosphere, they have exposed a potential cyclic gas release process that arises when a material with a finite yield strength is contained within an elastically deformable vessel.

In §2.3, I describe the experimental apparatus and some details about the rheology of the bentonite-water mixtures used in the experiments. I report on a series of systematic experiments in which the clay fraction of the clay-water mixture was varied,

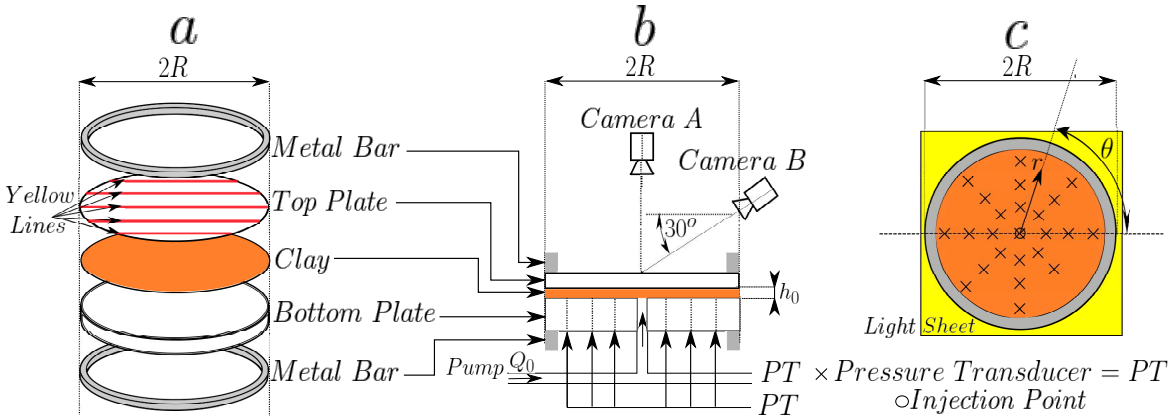


Fig. 2.1 Schematic of the experimental apparatus

from a dilute fluid-like mixture to a drier mixture which exhibits a yield stress (Lagaly [41]) or which may fracture (Alfaro and Wong [2]). These experiments demonstrate that there is a cyclic gas release mechanism that occurs with the clay-rich mixture, and involves a series of pressurisation-depressurisation cycles, resulting from the balance between the slow elastic deformation of the cell and concomitant flow of clay as the system is pressurised, and the opening of a channel through the clay at a higher pressure, leading to very fast release of gas as the system decompresses. I draw some conclusions and discuss the relevance for subsurface geological waste repositories and also for observations of discrete bubble-bursts at mud-volcanoes.

## 2.3 Experimental Method

The experiments were carried out in a circular cylindrical cell composed of two perspex plates, each of radius of 25 cm ($R_0$) with a gap of 4 mm ($h_0$). The bottom plate is 5 cm thick while the top one is 9.1 mm thick. The bending coefficient $B$ of the top plate has value $2.3 \times 10^2$ Pa m$^3$ which is much smaller than the bottom plate and so the main deformation of the cell occurs on the top plate. In setting up the experiment, the clay-water solution is spread on the bottom plate and levelled to a thickness of about 7 mm. The top plate is then placed on the mixture and the system compressed to produce a gap of approximately 4 mm. The two plates are pressed together using two metal rings of radius 24 cm and a 2 × 2 cm cross-section to spread the stress uniformly over the perimeter of the cell. This avoids the development of a variable stress at the edge of the tank when screwing the plates together. A schematic of the apparatus is shown in figure 2.1.

In order to visualise the deformation of the top plate, a grid of parallel lines has been painted on the top boundary of the cell using a bright yellow paint in order to be easily localised during the image analysis. During each experiment a series of photographs of the top surface was taken using a Canon D90 camera pointing at the top plate with an angle of $60^o$ to the vertical. The set up procedure described in the previous paragraph compresses the clay and this initial overpressure deforms the top plate. By comparing the position of the lines with respect to the initial pre-pressurisation location, the vertical deformation ($\Delta h(r, \theta)$) can be estimated.

The experiment is backlit by an electroluminescent sheet (W&Co LED panel 60 $\times$ 60 cm) and recorded from directly above the tank using a second Canon D90 camera with a 1 Hz image acquisition frequency. As air or water invades the cell and displaces the clay-water mixture, the light intensity increases so that the central cavity and, at later stages, fractures or channels can be visualised. In the experiments, I used a muslin with a relatively coarse mesh on the outer radial boundary of the cell in order to prevent clay loss from the cell, while allowing air or water to leave the cell.

The clay-water solution is prepared with a food mixer which exerts a high shear stress on the clay. This breaks the bentonite platelet structures and so before running the experiment, once the clay has been placed in the cell, the system is left for 3 hours so that the clay structures can become re-established.

The clay consists of bentonite (provided by Sigma-Aldrich) mixed with water and its physical properties are dependent on the mass fraction of clay in the mixture, $S = M_B/M_{tot}$ where $M_B$ is the bentonite mass and $M_{tot}$ is the total mass of the solution. In the present suite of experiments, $S$ lies in the range $0.05 \leq S \leq 0.16$. I used an oscillatory rheometer (Bohlin rheometer CS-50) to measure the rheology of the clay-water mixtures (figure 2.2 a-b). At low shear stress, the bentonite behaves as an elastic material with a high and relatively constant elastic modulus ($G'$) which increases from $1 - 10^5$ Pa as $S$ increases from 0.1 to 0.2 (solid lines in figure 2a). Once the shear stress exceeds a critical value, the yield stress ($\sigma_y$), then the mixture deforms and the elastic modulus becomes much smaller (figure 2.2a). The yield stress increases approximately exponentially with the clay content of the mixture, from about 25 Pa when $S = 0.1$ to about 2 KPa when $S = 0.2$ (figure 2.2b). Beyond the yield point, the material becomes shear thinning and the effective viscosity, as measured by the rheometer, falls as the shear stress increases (dotted lines in figure 2.2a).

On starting an experiment, air or water is pumped into a port at the centre of the tank using two syringe pumps (NE-1050: World Precision Instruments) working in alternate cycles to provide an almost constant volume flow rate $Q_0 \simeq 1$ cc/s. The

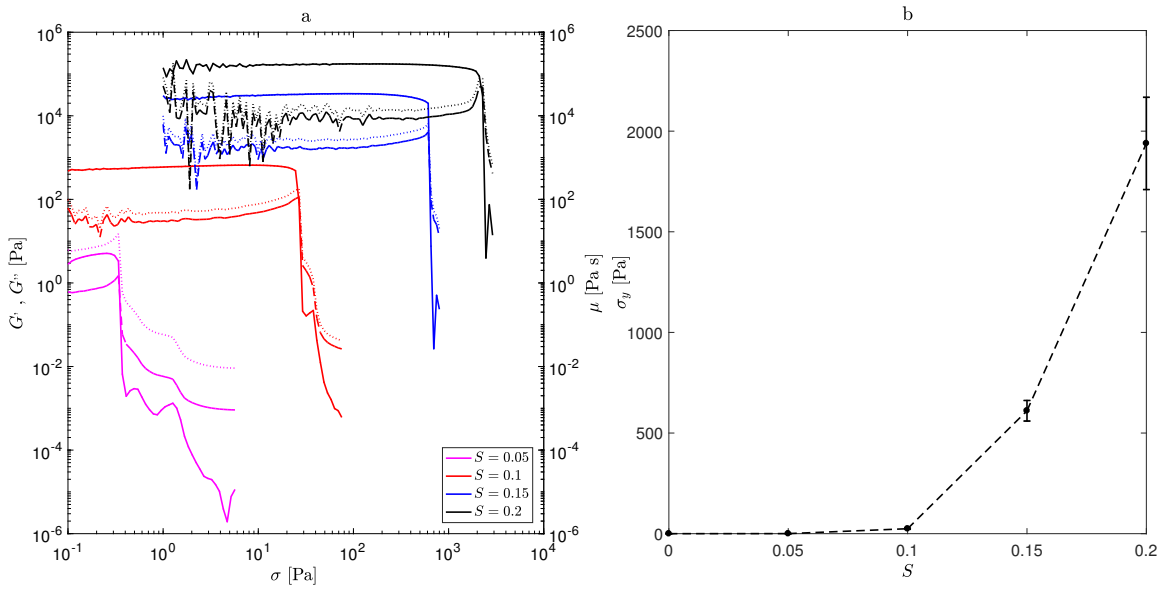


Fig. 2.2 (a) Plot of the elastic modulus ($G'$, solid line), the viscous modulus ($G''$, dashed line) and the dynamic viscosity ($\mu$, dotted lines) measured by the rheometer at various shear stress ($\sigma$) for four different bentonite content mixtures. (b) Plot of the yield stress as a function of the clay mass fraction $S$.

| Exp. | S | injection | filter | Exp. | S | injection | filter |
|---|---|---|---|---|---|---|---|
| 1 | 0.05 | a | × | 17 | 0.12 | a | × |
| 2 | 0.07 | a | × | 18 | 0.13 | a | × |
| 3 | 0.08 | a | × | 19 | 0.15 | a | ✓ |
| 4 | 0.09 | a | × | 20 | 0.15 | a | ✓ |
| 5 | 0.1 | a | × | 21 | 0.05 | a | ✓ |
| 6 | 0.1 | a | × | 22 | 0.07 | a | ✓ |
| 7 | 0.11 | a | × | 23 | 0.13 | a | ✓ |
| 8 | 0.12 | a | × | 24 | 0.05 | w | × |
| 9 | 0.13 | a | × | 25 | 0.07 | w | × |
| 10 | 0.13 | a | × | 26 | 0.08 | w | × |
| 11 | 0.14 | a | × | 27 | 0.09 | w | × |
| 12 | 0.14 | a | × | 28 | 0.1 | w | × |
| 13 | 0.15 | a | × | 29 | 0.11 | w | × |
| 14 | 0.15 | a | × | 30 | 0.12 | w | × |
| 15 | 0.16 | a | × | 31 | 0.13 | w | × |
| 16 | 0.13 | a | × | 32 | 0.15 | w | × |

Table 2.1 A summary of the experiments carried out specifying the mass fraction of clay ($S$), the fluid injected, air (a) or water (w), and presence of the outer low permeability filter.

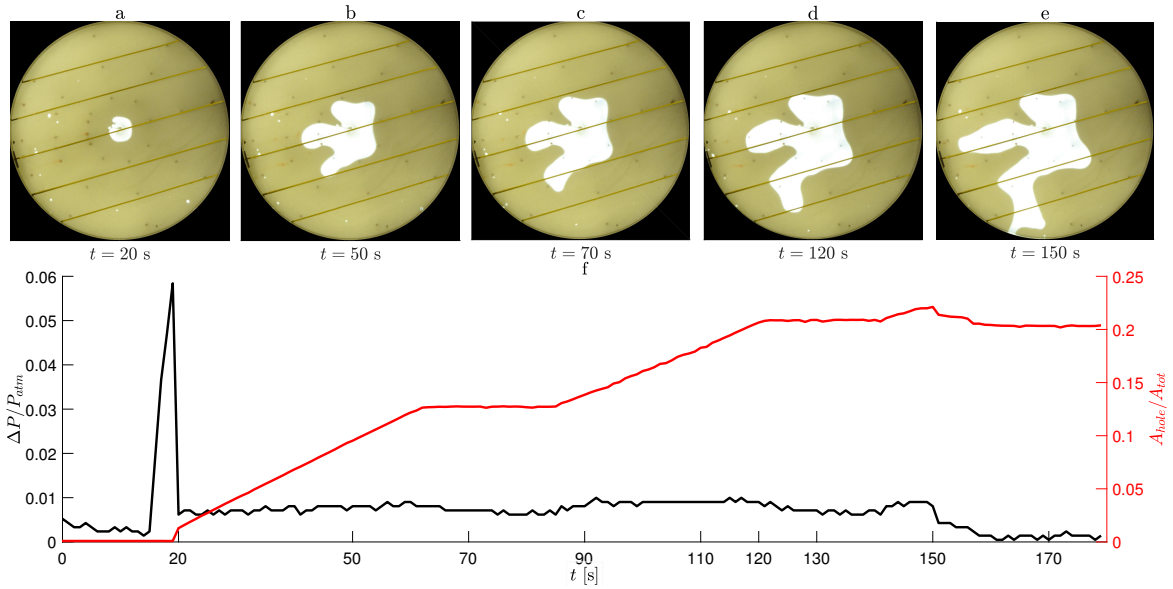


Fig. 2.3 (a-e) Images showing the growth of the air void in an experiment for which $S = 0.07$. The clay migrates radially outwards, but the interface becomes unstable and develops fingers, with a dominant finger eventually growing to the boundary of the domain allowing the gas to escape. (f) Plot of the pressure at the injection point (Black line) and area of the hole occupied by the gas injected (Red line) over time.

pressure ($P$) in the domain is measured by 24 pressure transducers with range ±30 KPa, and provided by Honeywell. These are connected to holes at different positions on the rigid bottom plate, one of which is located at the injection point in the center of the cell. The pressure transducers were scaled by connecting them to a vertical cylinder which was then filled with water at different heights. The results obtained from 32 experiments, listed in table 2.1 describing the behaviour of the system show a substantial difference between mixtures of (§2.4.1) low and (§2.4.1) high clay content.

## 2.4 Experimental Results

### 2.4.1 Low clay content

With clay content $S$ smaller than about 0.10, the yield stress in the clay mixture is very small, and the clay begins to flow and migrate radially outwards soon after the air is injected into the centre of the cell (*e.g.* figure 2.3, panel a). Owing to the viscosity contrast with the air, this leads to development of a fingering instability, somewhat analogous to the Saffman-Taylor instability (Saffman and Taylor [68]) as the air displaces the clay-water mixture (*e.g.* figure 2.3, panel b-e). Since the clay is

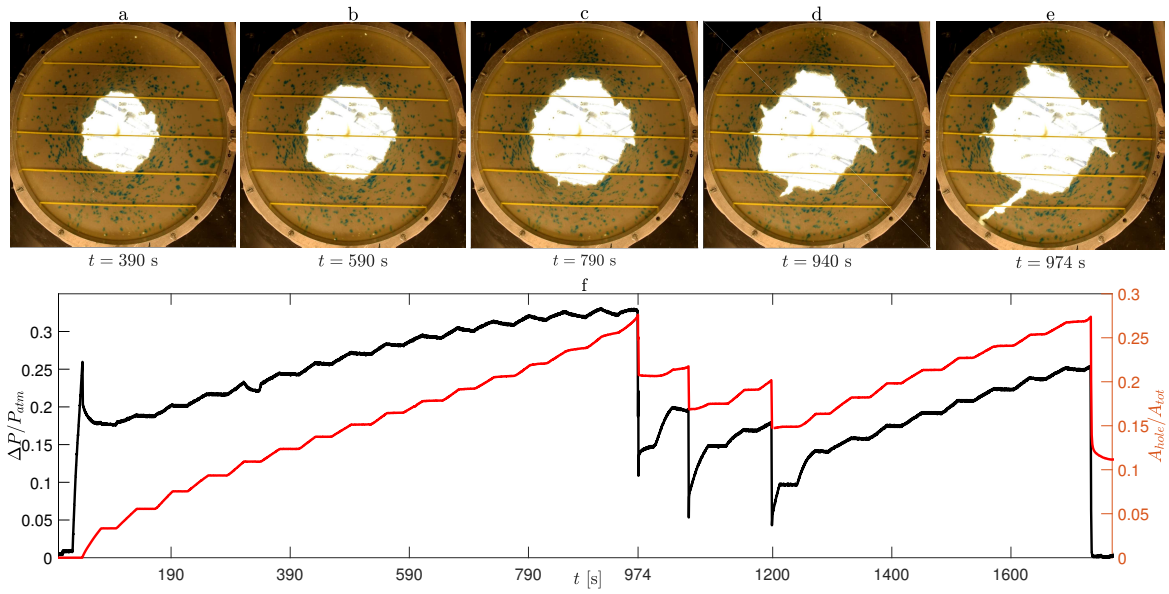


Fig. 2.4 (a-e) Series of images showing the initial nearly radial deformation of a clay-water mixture with $S = 0.13$ (panels a-c) followed by formation of a fracture-like channel (panels c-e) once the pressure surpasses a critical pressure ($P_{cr}$). (f) Plot of the pressure at the injection point (Black line) and area of the hole occupied by the gas injected (Red line) over time.

relatively mobile, the pressure in the cell remains relatively low (figure 2.3 f) and the cell deformation is small. Such fingering has been observed in earlier experiments of clay displacement in a narrow gap (*cf.* Holtzman et al. [30]).

### 2.4.2 High clay content

With clay content $S$ in excess of about 0.10, the initial viscosity of the clay mixture becomes progressively higher and the yield stress larger (figure 2.2 a and 2.2 b). Figure 2.4 panel a-e illustrates the evolution of a clay-water mix ($S = 0.13$) as air is injected into the cell. After reaching the yield stress the clay spreads out in a near radial pattern with an air-void forming in the centre of the cell (panels a-c). However, in panel c and d a small fracture-like feature can also be seen to be developing in the lower left hand side of the cell and by panel e the fracture-like feature has reached the outer edge of the domain. It then releases the highly pressurized gas from the centre of the cell. The clay flows back to fill the fracture-like channel and the central air-void shrinks and becomes confined again (figure 2.6). With further injection of gas the system can repressurize (figure 2.4 f). These observations of a yield stress and a fracture stress in

a clay-water mixture are consistent with earlier experiments (Marques [48], Shen and Miura [72] and Besq et al. [6]).

In order to analyse the evolution of these cycles in more detail, in figures 2.5 and 2.6 I present data from another experiment using clay for which $S = 0.14$. Figure 2.5a illustrates the evolution with time of the pressure at the centre of the cell and the average radius of the central air-void, $\bar{R} = \frac{1}{2\pi}\int_0^{2\pi} R(\theta)d\theta$, where $R(\theta)$ is the radius of the air-void from the centre of the cell at angle $\theta$. $R(\theta)$ was measured applying a threshold on the light intensity captured by the top camera during the experiments. The figure shows a series of five pressurisation cycles which develop while air is supplied to the centre of the cell at a near constant rate (approximately $1\text{cm}^3/\text{s}$). I also show the variation of the area of the air-filled region in the centre of the cell, as measured by the average value $\bar{R^2} = (1/2\pi)\int_0^{2\pi} R^2(\theta)d\theta$, as a function of the pressure in the centre of the cell (figure 2.5b). To complement these data, in figure 2.6a-e we show a series of photographs of the deformation of the clay with time during the fifth cycle of figure 2.5a, and in figure 2.6f-g we illustrate the variation of the area of the air-filled zone as a function of the pressure at the centre of the cell and as a function of the height at the centre of the cell to identify the conditions at which each photograph (figure 2.6a-e) was taken.

At the end of each cycle, the cell has a high pressure and large air void in the centre of the cell, while a narrow channel can be seen connecting this air void to the exterior (figure 2.6a). As the air escapes from the centre of the cell, there is a rapid drop in pressure and in the size of the void as the deformation of the top plate decreases and clay flows back towards the centre. During this phase, the channel to the exterior also becomes closed by the clay, sealing the channel and isolating the remaining air void in the centre of the cell (figure 2.6b). Once the pressure has fallen to point B then as more air is supplied to the centre of the cell, the pressure in the air-filled void builds up again. During the transition B-C, the clay is non-yielding and the air-filled void does not grow. However, on reaching point C, the pressure has become sufficient that the clay can flow and it moves outwards while the upper plate of the cell deforms, as shown by points (D) and (E). As the cell deforms the narrow channel which connected the central air-void to the outer edge of the tank gradually re-opens. Eventually, just beyond point (E), the channel reaches the outer edge of the cell, the air escapes and the cycle repeats.

Figure 2.5b shows that there is a jump in the relation between the pressure and the size of the air-void between the first pressurisation cycle and the subsequent cycles. On the first cycle, the initial manually filled cell is pressurised. The clay is then

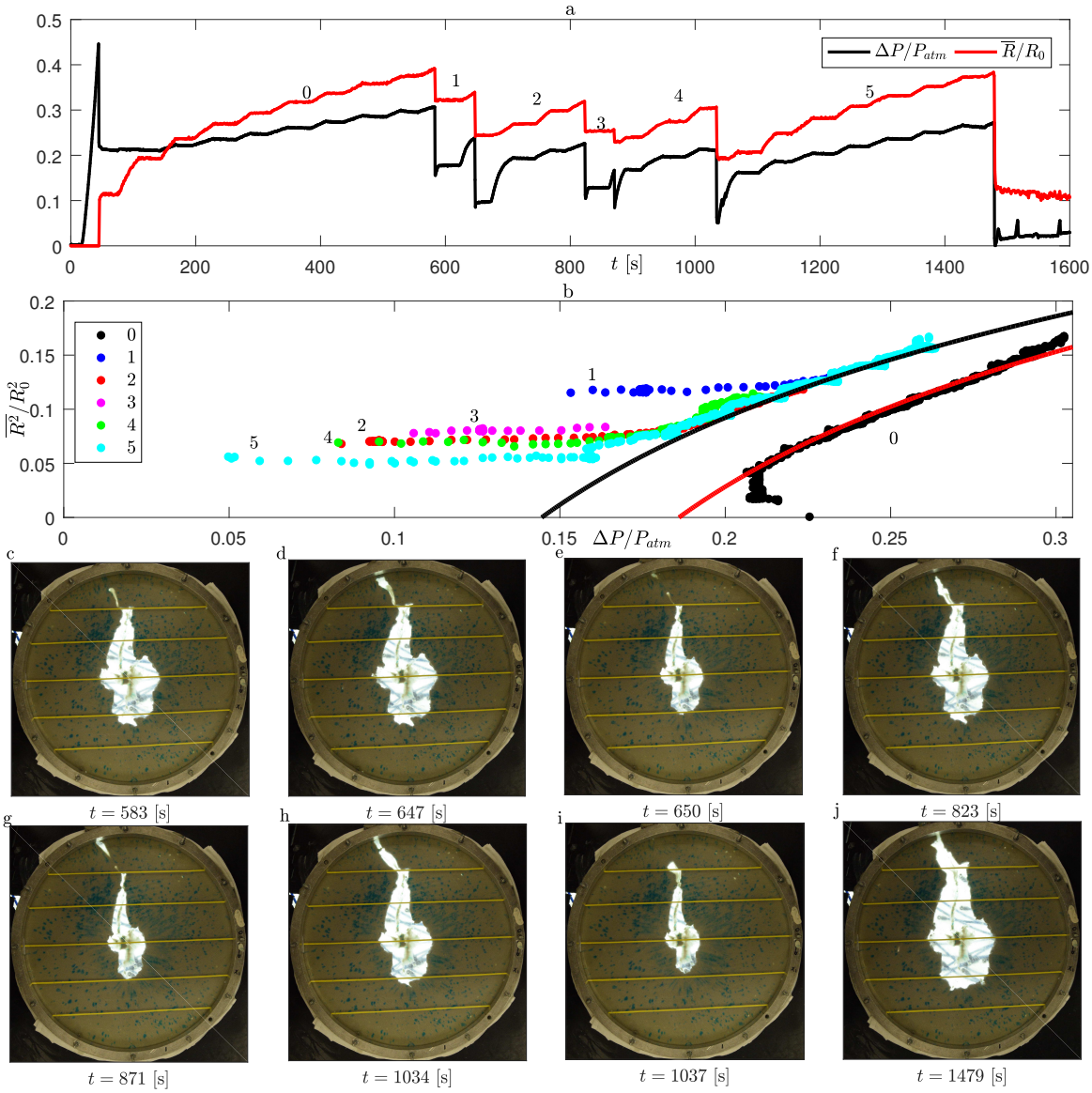


Fig. 2.5 (a) Variation of the pressure (black) and mean radius (red), $\bar{R}$, scaled with the radius of the cell, $R_0$, as a function of time during an experiment in which air is injected into a clay-water mixture with $S = 0.14$. Five pressurisation-depressurisation cycles may be seen. (b) Variation of the area of the void space in the centre of the cell, $\pi\bar{R}^2$, scaled with the area of the cell, $\pi R_0^2$, as a function of the pressure at the centre of the cell for the experiment shown in panel a. (c-j) Frames of the experiment plotted in panel a and b showing the gas volume in the cell at the initial and final stages of the cycles 1,2,4 and 5 (defined in panel a and b). After the first cycle, the system evolves along a common $\bar{R}^2 - P$ curve during the pressurisation phase of the cycles, once the clay begins to yield and deform. The red and black lines in figure 2.5b are predicted by equations 2.8 using the value $B = 2.3 \times 10^2$ Pa m$^3$.

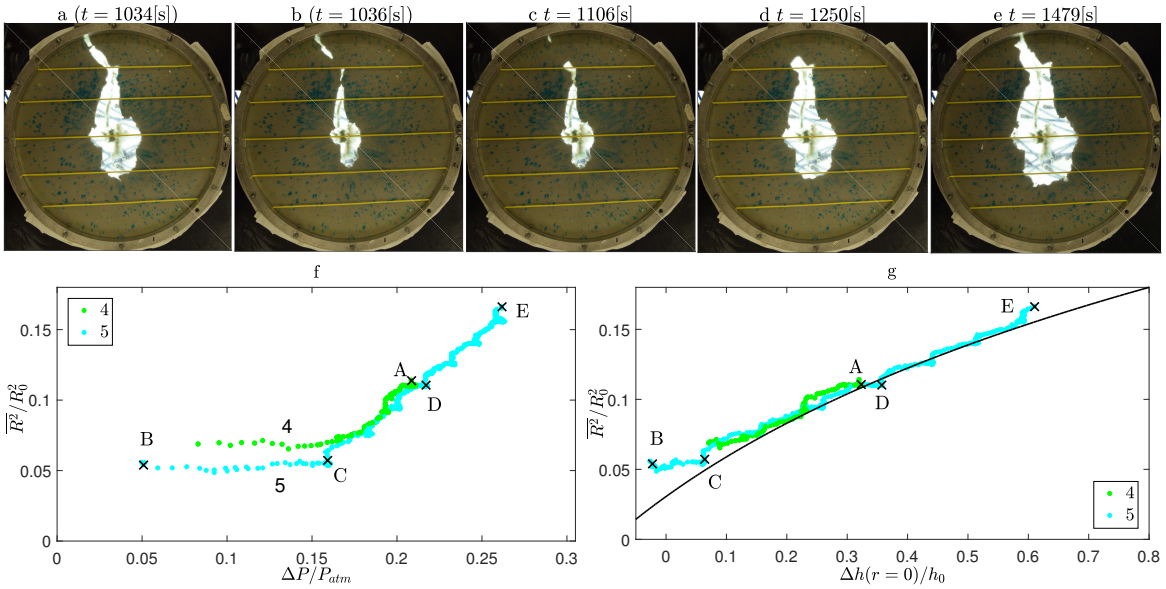


Fig. 2.6 (a-e) Series of photographs showing the evolution of the air-void and clay during cycle 5 of figure 2.5. The points marked (A-E) correspond to (panel 2.6a) the end of a pressurisation cycle; (panel 2.6b) the state just after the channel reaches the outer edge of the cell and the decompression has occurred; (panel 2.6c) the state once the pressure has built up to the yield stress; (panel 2.6d) a state part way through the evolution as the clay spreads radially outwards and the upper plate deforms; (panel 2.6e) the final pressurised state just before the fracture-like channel has reached the outer edge of the cell. Variation of the area of the air-void in the centre of the cell, $\pi\bar{R}^2$, scaled with the area of the cell, $\pi R_0^2$, during cycle 5, as a function of (f) the pressure at the centre of the cell and (g) the deformation at the centre of the cell, showing the conditions for each of the photographs 2.6a-e.

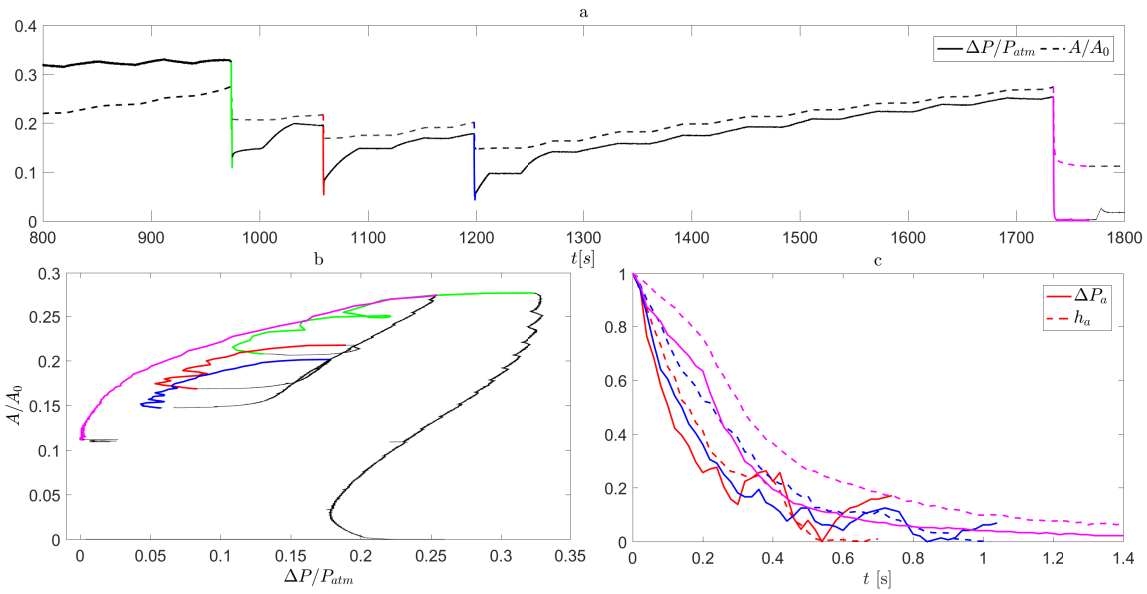


Fig. 2.7 (a) Plot of pressure (solid line) and air gap surface (dashed lines) over time for an experiment recorded by a high speed camera. The successive stages are identified by colours (green, red, blue and purple lines); the clay used in this experiment has $S = 0.13$. (b) Variation of the area of the void space in the centre of the cell, $A$, scaled with the area of the cell, $A_0$, as a function of the pressure at the centre of the cell for the experiment shown in panel a. (c) Non-dimensional pressure (solid lines) and top plate deformation (dashed lines) at the injection point for the last three stages of pressure release described in panel a where the suffix $i$ is the initial stage before the gas is released in the atmosphere and $f$ the final one when the fracture is clogged.

re-distributed and compacted within the cell during the first cycle and towards the end of this cycle, the mesh filter at the edge of the cell fills with clay, preventing further loss of clay from the cell. As seen in figure 2.5b, on subsequent cycles, the system follows a very similar deformation-pressurisation path. Figure 2.6b also illustrates that the pressure at which the channel to the outside edge of the clay breaks through, leading to the decompression phase, varies from cycle to cycle. It is thought that this depends on the degree of closure of the channel in the previous decompression phase. The inner pressure and the degree of closure from each experiment significantly varies from each experiment which makes it difficult to identify a correlation between the two data. Also, the pressure at which the clay yields and the cell begins to deform varies from cycle to cycle (figure 2.7b). This is interpreted as a result of the somewhat irregular shape of the void which varies in detail from cycle to cycle. However, there is a well-defined trend relating the pressure and area of the void which is discussed later.

Using a higher frame acquisition frequency with both cameras, approximately 50 Hz, it was possible to collect data of the decompression stage once air is able to escape the domain through a fracture like channel as shown in figure 2.7. When the pressure drops the elastic plate relaxes and its vertical deformation decreases to a steady condition. Both the pressure drop and the top plate relaxation take a couple of seconds to reach the steady condition but the high frequency data showed that the pressure drop acts faster than the top plate relaxation time. When the pressure drops the elastic reaction of the plate displaces the viscous clay but this reaction requires a longer period to reach the relaxation state than the actual pressure drop, figure 2.7b. In order to analyse the relaxation stages, the pressure and deformation of the top plate at the injection point were measured as $\Delta P_a = \frac{\Delta P - \Delta P_i}{\Delta P_f - \Delta P_i}$ and $h_a = \frac{h - h_i}{h_f - h_i}$. Here $\Delta P_i$ and $h_i$ are respectively the pressure and top plate deformation before the fracture-like channel reaches the edge of the domain, allowing the gas to escape. $\Delta P_f$ and $h_f$ are the pressure and top plate deformation after the channel is clogged due to the clay displacement caused by the pressure release. The data of the gas release can be modelled as an exponential decay ($\Delta P_a = e^{-\lambda_P t}, h_a = e^{-\lambda_h t}$). The data show that $\lambda_P = 7.7 \pm 3.6$ while $\lambda_h = 3.5 \pm 1.6$, and that, during each of the decompression cycles, $\lambda_P > \lambda_h$ and their ratio lies in the range $6 \geq \lambda_P/\lambda_h \leq 1.5$. This result confirms the high difference in speed between the pressure release and the volume contraction which depends on the elastic properties of the top plate and the viscosity of the fluid. In order to study the behaviour of a relatively slow gas release compared to the elastic relaxation of the top plate I ran some experiments with a low permeability filter which will be discussed in the following section.

### 2.4.3 Effect of an outer low permeability filter ring

The origin of the cycles lies in the different times scales for injection of air, which is slow, and the release of air from the air-void once the fracture-like channel reaches the outer edge of the cell, which is fast. The closure of the channel during the decompression provides a mechanism for isolating the air-void during the recharge process. In order to demonstrate the dependence of the cycles on the fast release of gas along the channel, I placed a very low permeability ring around the outer edge of the cell such that the pressure jump required to drive the gas across this ring is comparable to the pressure required for the clay to yield, and I then repeated the experiments. This polyethylene ring filter (Vyon® D provided by Porvair filtration group) has a mean pore size of 16 $\mu$m and permeability estimated to be $\kappa_f \simeq 10^{-12}$ m$^2$. The variations of the filter permeability caused by the stresses in the domain were neglected because of the low

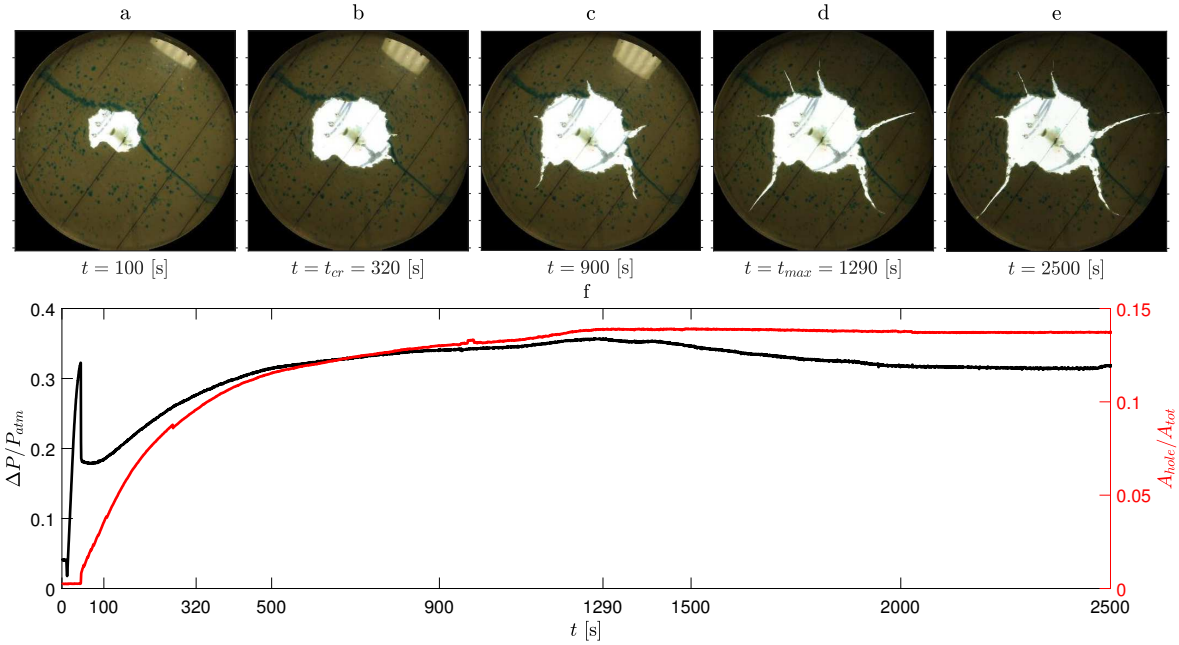


Fig. 2.8 (a-e) Series of images showing the low permeability filter case with the initial nearly radial deformation of a clay-water mixture with $S = 0.15$ (panels a-b) followed by formation of a fracture-like channel (panels b-e) once the pressure surpasses a critical pressure ($P_{cr}$). Panel d and e show the top view of the experiment at the time the pressure at the injection point reaches the maximum value ($t = t_{max}$) and once the steady state case, characterised by an air outflow equal to the inflow. (f) Plot of the pressure at the injection point (Black line) and area of the hole occupied by the gas injected (Red line) over time.

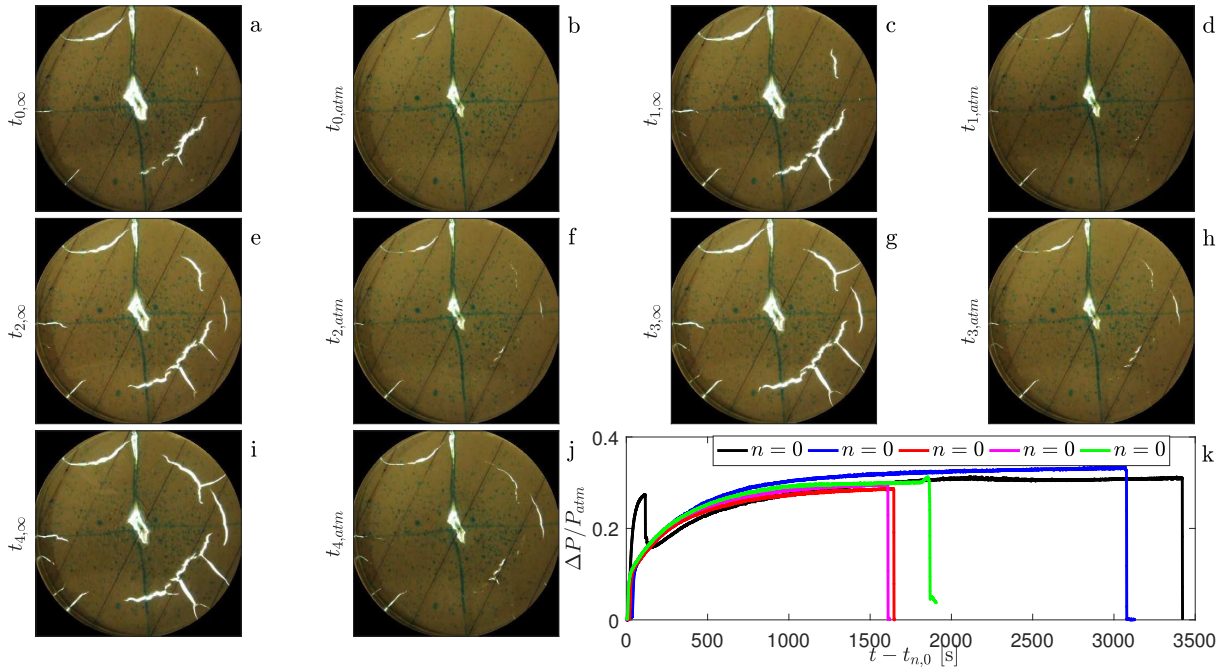


Fig. 2.9 (a-j) Top view images of a cyclic air injection once reached the steady state ($t_{n,\infty}$) and after the pressure at the injection point is released before starting the next cycle injection ($t_{n,atm}$) to the atmospheric pressure in clay-water mixture $S = 0.15$ and confined by a low permeability filter. (k) Plot of pressure at the injection point for each of the five cycles ($n$), where $t_{n,0}$ is the gas injection starting time for the $n$ cycle.

pressure measured during the experiments (lower than 50 kPa). Figure 2.8 shows top-view images and a plot of pressure and size of the area occupied by the gas injected at different stage of an experiment with an outer low permeability filter. On supplying air to the cell, the pressure gradually built up (figure 2.8f) within the cell and, as before,a radial displacement of the clay (figure 2.8 panels a and b) is followed by a fracture-like channel growth to the outer edge of the cell (figure 2.8 b-d). At this point however the flux of gas through the low permeability filter was smaller than the supply rate from the pump and so the pressure initially continued to increase until the leakage rate through the filter matched the supply rate (figure 2.8 panels d and e).

During an experiment with the low permeability filter, after reaching the steady state condition, the injection point was opened letting the gas escape the domain and causing an instant drop of pressure to the atmospheric value. The sudden decrease in pressure causes the elastic top plate to displace the clay towards the center of the cell. Once the displacement stopped, the gas injection was started again and the cycle was repeated four times. Figure 2.9 a-j show frames for each cycle ($0 \leq n \leq 4$ where $n$

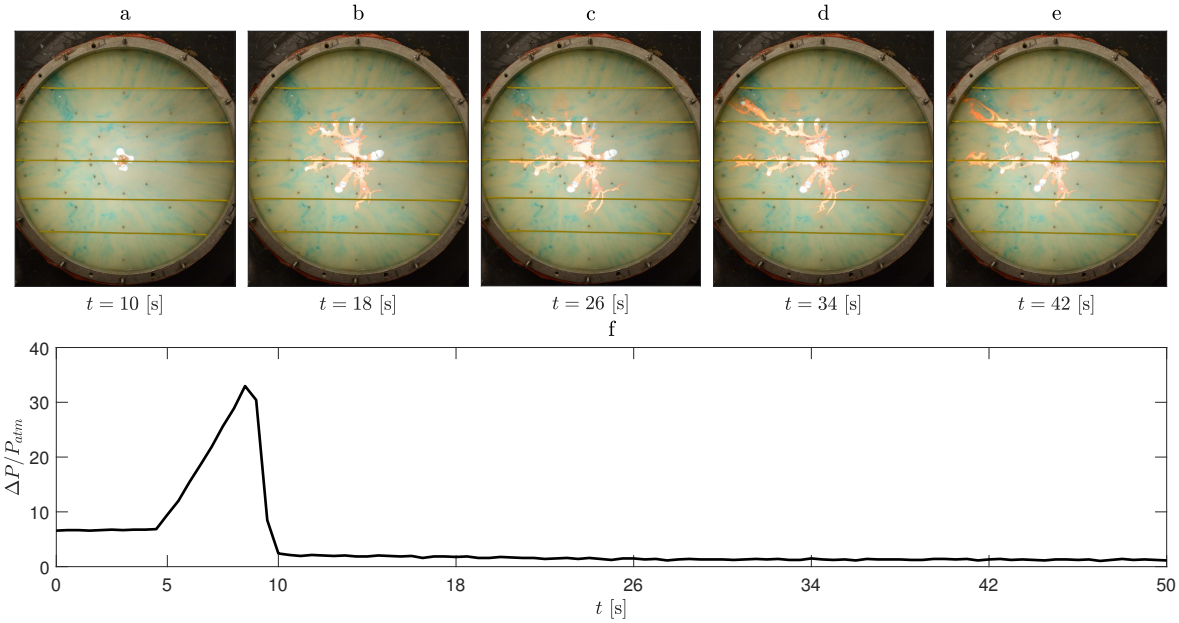


Fig. 2.10 (a-e) Images showing the growth of the water void in an experiment for which S = 0.07. The water-clay interface becomes unstable and develops fingers. Once a finger eventually reaches the boundary of the domain the water can escape. (f) Plot of the pressure at the injection point.

is the cycle number) at the stage before ($t_{n,\infty}$) and after ($t_{n,atm}$) the pressure release. Although the pressurisation path is similar for each cycle (figure 2.9k), after each pressure drop ($t_{n,\infty}$) some fractures persist even after the relaxation of the top plate (figure 2.9b,d,f,h and j). The total area occupied by the fractures after each pressure drop increases with each cycle suggesting a non reversibility of the experiment. The high gas pressure may locally compact the clay or cause dewatering of the clay near the gas-filled fracture. This would explain the persistence of fractures after the release of the high pressure.

### 2.4.4 Water injection

Some experiments were performed in which water was injected into the clay. The water was dyed red to enable visualization of the flow path of the water through the clay. Water infiltration on clay reservoirs is occasionally caused in nature by a deep high pressure aquifer in the proximity of a buried clay domain. With no surface tension between the two fluids, the radial displacement of the clay and formation of the central hole, as experienced during the air injection experiments (Figure2.4a-c), is unstable

and the water flows through the clay-water mixture in a series of finger/fracture like channels.

As with the air injection described in §2.4.4, high water content clays, $S < 0.1$, are displaced by a relatively low injection pressure and water penetrates the clay in a finger shaped pattern as shown in figure 2.10.

In case of high mass fraction clays, the injection of water pressurises the cell causing the clay to fracture. The fractures initially expand from the injection point in the radial direction while the pressure remains approximately constant (figure 2.11i). The pressure depends on the water content of the clay mixture (Figure2.12). The original radial spreading of the fracture is arrested close to the boundary ($r \approx 0.8R_0$) where the water flux starts eroding the clay along the outer perimeter of the cell. Similarly to the air injection cases, once a fracture reaches the edge of the domain, water rapidly flows out of the fracture and the consequent drop in pressure allows the fracture to clog. Once the flow out of the domain is stopped the persistent water injection cracks the clay and the cycle repeats. This cycle differs from the air injection case in three ways. Firstly the contraction of the fracture width, after reaching the boundary of the domain, affects only the fracture reaching the edge of the domain and mainly the final part of the fracture. On the other hand, during the air injection cases, the entire volume occupied by air shrank once air was free to escape the volume. Secondly the clogging and opening of fractures is more frequent than the air injection case and it is mainly focused along the peripheral area of the domain ($0.5 \leq r \leq 1$, figure2.11b-f). Finally the pressure sensor at the injection point did not measure any significant change in pressure (figure2.11i, $90 \leq t \leq 170$). These three results suggest that the pressure fluctuation is localised and concentrated in the outer part of the flow domain. The frequent cycles of clogging and opening of new fractures starts from the edge of the domain (figure2.11c, $1 \leq r \leq 0.8$) and slowly grows towards the center (figure2.11c-d $1 \leq r \leq 0.6$ and figure2.11e-f $1 \leq r \leq 0.45$). The water injection erodes the clay until it forms one single wide channel transporting most of the water flow out of the domain (figure2.11f) with a low pressure from one end of this channel to the other as compared to the environment ($\Delta P < 5$ kPa). Before reaching this final steady condition, the wider channels show the same cycles discussed before. When these wider fracture reach the edge of the domain water flows rapidly and causes a drop in pressure of about 5 kPa (figure2.11i, $t > 200$ s) and clogging.

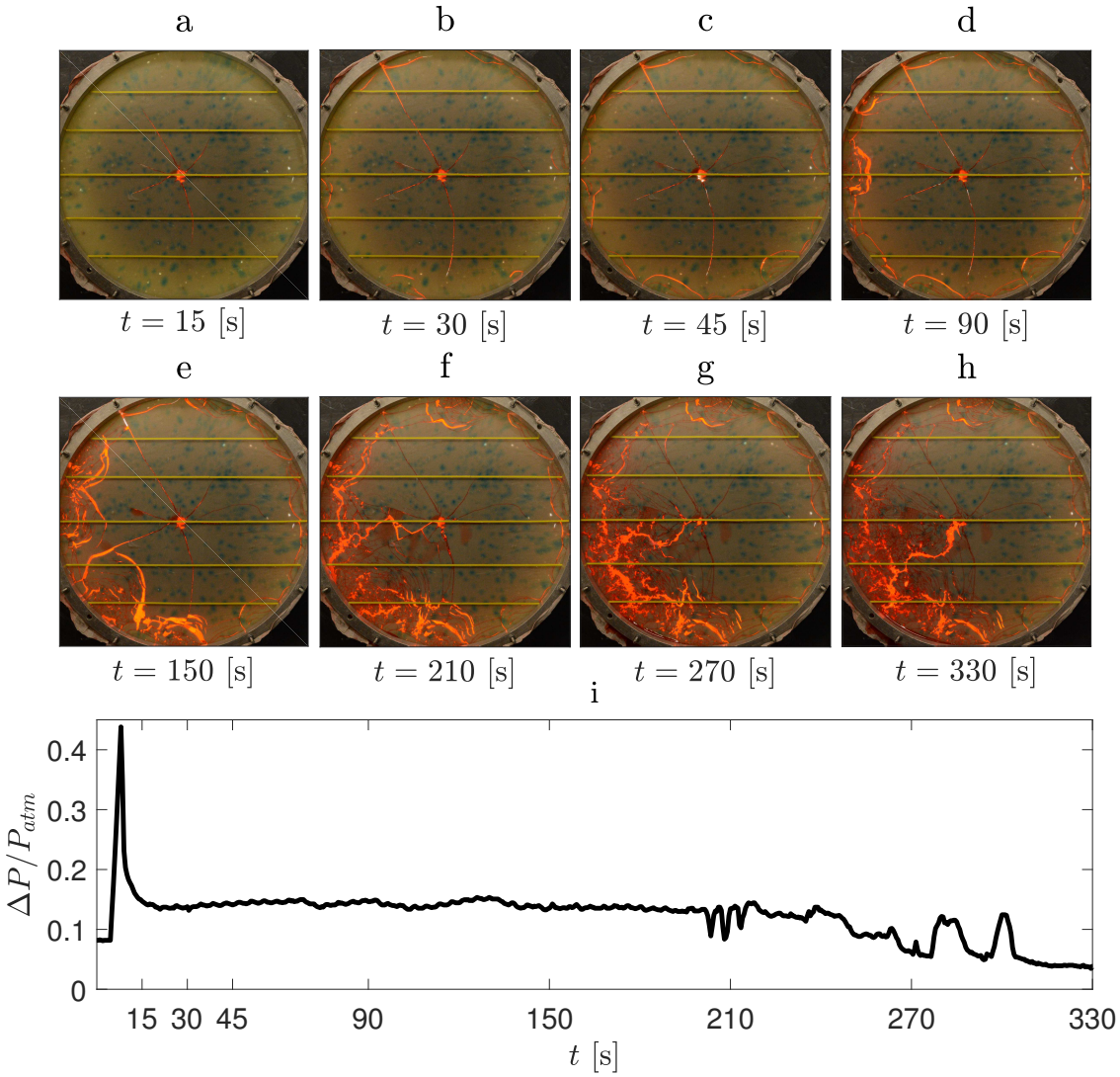


Fig. 2.11 (a-h) Frames capturing the evolution of an experiment injecting water in a high bentonite clay mixture, $S = 0.13$. Water starts fracturing the clay in radial direction (panels a and b) before eroding the peripheral area of the domain (panels c-f) until finally builds up a preferential channel connecting the injection point with the boundary of the cell (panel f-h). (i) plot of the overpressure at the injection point over time.

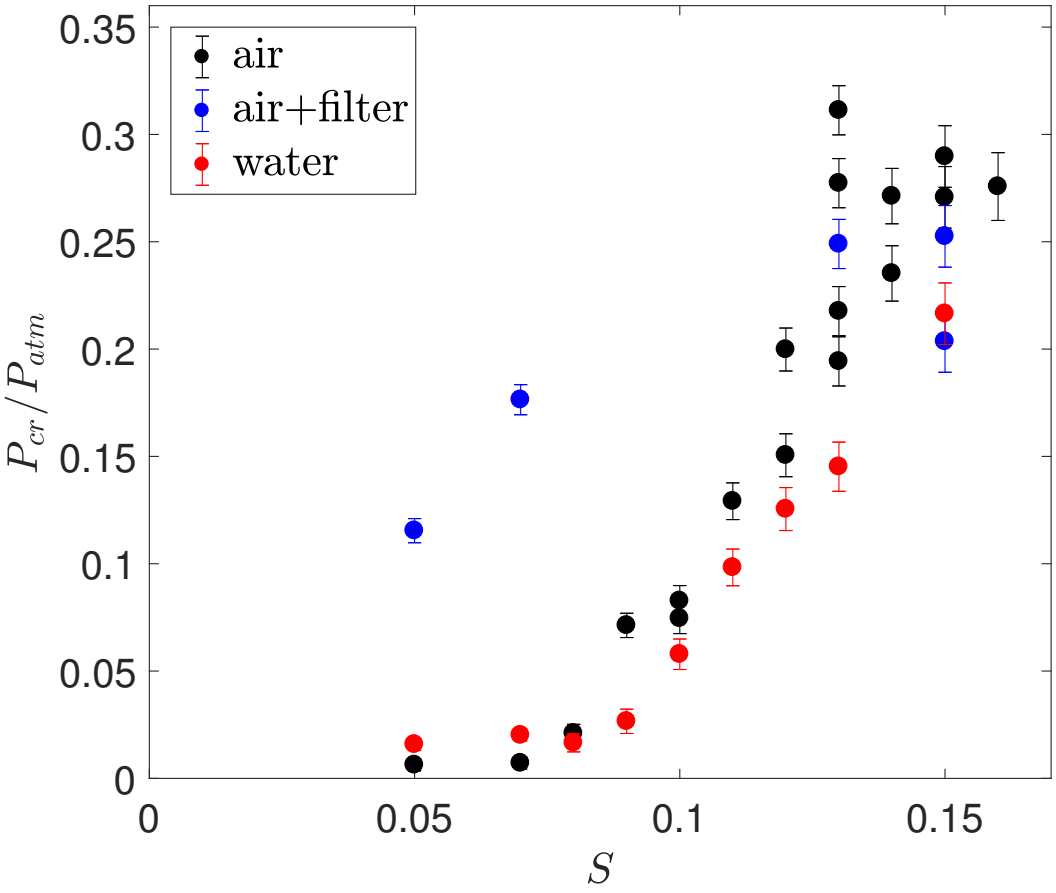


Fig. 2.12 Graph describing the relation between the pressure at which the fracture-like channel begins to migrate through the clay as a function of the clay mass fraction $S$.

### 2.4.5 Variation of breakthrough pressure as a function of the clay content

For the air injection experiments, during the first cycle of each experiment it is possible to identify a transition from a nearly axisymmetric deformation where the clay is displaced radially (figure 2.4a-c) to a second phase (figure 2.4c-e) in which a narrow fracture-like channel migrates through the clay ahead of this deformation front. It is possible to identify a fracturing pressure $P_{cr}$, (figure 2.12) as the minimum pressure at which the channel begins to form. In contrast, for the water injection experiments, the channels open up with an almost constant critical pressure, $P_{cr,w}$. A systematic series of experiments was carried out to determine the pressure $P_{cr}$ as a function of the bentonite content $S$. Figure 2.12 shows that $P_{cr}$ and $P_{cr,w}$ increase nearly exponentially

with clay content, from about 8 KPa with $S = 0.1$ to about 30 KPa with $S = 0.15$. Although a similar dependence of the fracture strength for water injection the critical pressure resulted consistently smaller than the air injection case provided $S \geq 0.08$ ($0.74 \leq P_{cr,w}/P_{cr} \leq 0.84$). When using a high water content clay the experiments using the low permeability filter show a critical pressure significantly higher than the non-filter cases. Due to the high water content the liquid-like clay was able to flow through the muslin and leak out of the domain. In this condition a low pressure gradient was sufficient to cause the outflow of clay from the edges of the cell. The low permeability filter did not allow the outflow of high water content clays from the domain. The gas enters the cell by deforming the top plate and expanding the domain. The expansion of the cell volume requires a much higher pressure that the one required to drive the flow out of the domain. It follows that, during experiments using high water content clays, the $P_{cr}$ with a low permeability filter is much higher than the non-filter case (figure 2.12)

## 2.5 Discussion

The slow deformation of the cell measured in terms of the increase in the gap width, $\Delta h(r)$, relative to the uniform gap width, $h_0$, with zero overpressure, as a function of radius, $r$, may be described in terms of the overpressure within the cell, $\Delta p(r)$, and the bending moment or flexural rigidity of the upper plate of the cell, $B = 2.3 \times 10^2$ Pa m$^3$, according to the relation

$$\Delta p(r) = B\nabla^4(\Delta h(r)) \tag{2.1}$$

In equilibrium, with uniform over-pressure $\Delta p$ associated with the pressurisation in the centre of the cell, this has solution for the increase in the gap width (Eq 62, Timoshenko and Woinowsky-Krieger [76])

$$\Delta h(r) = \frac{\Delta p}{64B}(R_0^2 - r^2)^2 \tag{2.2}$$

so that the increase in gap width at the centre of the cell is related to the overpressure according to

$$\Delta p = 64B\Delta h(0)/R_0^4 \tag{2.3}$$

The volume included between two radial position $R_A$ and $R_B$ (where $0 \leq R_A \leq R_B \leq R_0$), is given by $V = \int_{R_A}^{R_B} 2\pi r \left(h_0 + \Delta h(r)\right) \mathrm{d}r$ and using equations 2.2 and 2.3 results in the expression

$$V = -\frac{\Delta p \pi}{192B}\left[\left(R_0^2 - r^2\right)^3\right]_{R_A}^{R_B} + \pi\left(R_B^2 - R_A^2\right) = -\frac{\Delta h(0)\pi}{3R_0^4}\left[\left(R_0^2 - r^2\right)^3\right]_{R_A}^{R_B} + \pi\left(R_B^2 - R_A^2\right) \tag{2.4}$$

If the overpressure changes from value $\Delta p_1$ to value $\Delta p_2$, the gap between the plates changes according equation 2.4 (where $R_A = 0$ and $R_B = R_0$), leading to the expression for the change in the volume between the plates, $\Delta V = V(\Delta p_1) - V(\Delta p_2)$ given by

$$\Delta V = \frac{\pi R_0^6}{192B}(\Delta p_1 - \Delta p_2) = \frac{\pi R_0^2}{3}(\Delta h(0)_1 - \Delta h(0)_2) \tag{2.5}$$

where $R_0$ is the radius of the cell and $(\Delta h(0)_1 - \Delta h(0)_2)$ is the change in the gap width at the origin. Considering the clay incompressible because of the low pressure of the experiments, this change in volume leads to a change in the size of the air void in the centre of the cell. If the air void is modelled as being axis-symmetric in the region $0 < r < R(t)$, with the clay being displaced to the outer part of the cell, $R(t) < r < R_0$, then the volume of clay in the cell $V_c$ may be expressed as

$$V_c = \frac{\pi}{3}\Delta h(0) R_0^2 \left[1 - \left(\frac{R(t)}{R_0}\right)^2\right]^3 + \pi h_0 R_0^2 \left[1 - \left(\frac{R(t)}{R_0}\right)^2\right] \tag{2.6}$$

Assuming that the volume of clay in the cell remains fixed, this defines the relation between the top plate deformation and the radius of the air gap as

$$\Delta h(0) = \frac{3}{\pi R_0^2}\left\{V_c - \pi h_0 R_0^2 \left[1 - \left(\frac{R(t)}{R_0}\right)^2\right]\right\}\left[1 - \left(\frac{R(t)}{R_0}\right)^2\right]^{-3} \tag{2.7}$$

Providing that $R(t) << R_0$ and applying a binomial expansion to the last term in square brackets of equation 2.7 it follows that, as the clay is displaced outwards, the gap width at the centre of the cell is related to the radius of the void by the approximate relation

$$\Delta h(0) = \frac{3}{\pi R_0^2}\left\{\left[V_c - \pi h_0 R_0^2\right] + \left(3V_c - 2\pi h_0 R_0^2\right)\frac{R(t)^2}{R_0^2}\right\} \tag{2.8}$$

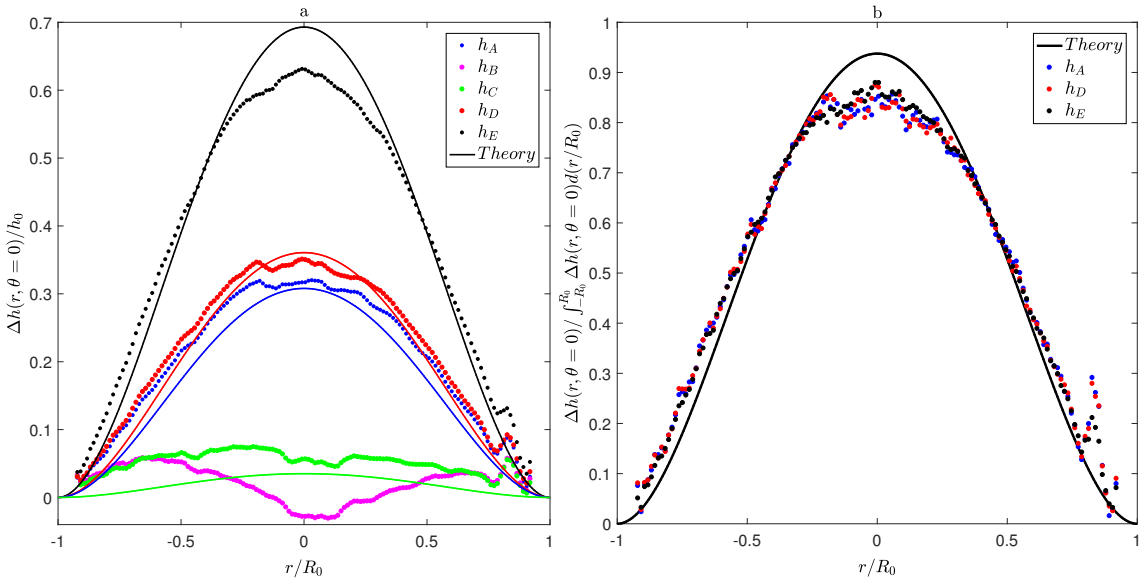


Fig. 2.13 (a) Variation of the shape of the upper plate of the cell at points A,B,C,D and E of cycle 5 shown in figure 2.5, illustrating the shape just prior the decompression (A), the shape following decompression (B), the onset of deformation once the clay becomes mobile (C), followed by the growth of the void space until the clay fractures (D and E). In each case the dashed line shows the prediction of equation 2.2 based on the measured pressure change at the centre of the cell. (b) The rescaled shape of the deformation for each of these times is shown in comparison to the model prediction.

In figure 2.5b, it may be seen that after the initial deformation cycle, defined as stage 0, once the clay becomes mobile, the overpressure and hence gap width at the centre of the cell (equation 2.3) varies in proportion to the area of the void and on each cycle, the data follows the same curve, of the form given by equation 2.8. The first term on the right hand side of equation 2.8, shown in square brackets, is a constant related to the fixed volume of clay in the cell and this can be estimated by fitting the curve to the data. I note that during the initial cycle of gas pressurization, defined as stage 0 in figure 2.5, once the clay becomes mobile and is displaced radially outwards from the centre of the cell, the relation between overpressure and area of the void follows the relation given by equation 2.8, but with a larger constant. This is because near the end of this initial cycle, as the overpressure reaches a maximum, there is some loss of clay from the edge of the cell into the filter which then suppresses any subsequent loss of clay. As a result, during the initial cycle there is more clay in the cell and so the constant has a larger value.

The relationship between $\Delta h(0)$ and $\bar{R}^2$, the size of the cavity, is consistent with the data as shown by comparison of the black line and the data in figure 2.5b and

2.6g. Using the value of the constant in equation 2.8 by matching with the data, I have compared the shape of the upper surface of the cell $\Delta h(r)$ with the model prediction (equation 2.2) and this is shown in figure 2.13a,b at points A,C,D and E during cycle 5 of the experiment shown in figure 2.5 and 2.6 (A, C, D and E). For clarity all the data has been rescaled in figure 2.13b, and compared with one dimensionless model profile. There is good agreement of the model prediction for the shape of the deformed lid with the actual data, especially given the complexity of the actual shape of the void (figure 2.13).

## 2.6 Summary

In a series of experiments in which air is injected into a confined two dimensional layer of clay, we have found that as the pressure exceeds the yield stress of the clay, the air can displace the clay-water mixture radially outwards and the upper plate of the cell deforms upwards elastically. This leads to a radially symmetric flow of the clay until, at a higher pressure, a fracture-like channel migrates through the clay to the outer edge of the cell. The pressurized air in the centre of the cell then escapes along this channel, with an associated rapid decrease in the pressure of the cell, closure of the channel and shrinking of the air void, as the clay spreads out. The continued injection of air into the cell then builds up the pressure of the isolated air-void until the clay becomes mobile and is displaced outwards again and the cycle repeats. The critical pressures at which the clay becomes mobile and at which the fracture-like channel opens up do vary from cycle to cycle, owing to the irregular shape of the air-void and to the non-uniqueness of the fracture healing process during decompression.

The experiments have implications for a number of geophysical processes involving the pressurisation of non-newtonian materials by injection or production of gas, and the ensuing episodic release of the gas. The process may be responsible for the periodic release of biogenic gas which accumulates in mud deposits on the sea-floor or for the episodic release of gas in mud volcano systems, as methane builds up in a sub-surface reservoir until reaching a critical pressure to fracture the mud. For example, Feseker et al. [24] report on four eruption events emitting about $10^4$ m$^3$ methane over a 430 day survey of the Hakon Mosby Sea Volcano. The fractional change in volume, $\Delta V$, required to pressurise the clay up to the fracturing pressure $\Delta P$ is given by $\Delta V/V = \Delta P/\beta$. If we assume the mud has a fracture stress with values of $10^5$ (Marques [48]) $-10^7$ Pa (Donohew et al. [22]), then if the gas accumulates at depths of a several hundred metres over a volume of $V \sim 10^8$ m$^3$ for example, perhaps extending of order $1 - 5 \times 10^3$ m in

lateral scale (Shirzaei et al. [73]), then with a bulk modulus of order $\beta = 3.6 \times 10^{10}$ Pa (table 4.2 in Poletto and Miranda [60]), we predict that the volume which can erupt, $\Delta V$ will be in the range $10^3 - 10^5$ m$^3$, analogous to observations. Following fracture of the confining clay, this excess gas may migrate and erupt at the surface. In the case of a geological waste repository in which the waste material is sealed within a clay layer or clay-based engineered barrier, the accumulation of gas following generation within the repository may lead to an increase in pressure until eventually fracturing of the confining clay occurs. This could generate transient high permeability pathways which enable relatively long-range gas transport even though the clay is an inherently low permeability medium. The experiments have also highlighted the self sealing property of the clay which is able to restore the high permeability after the pressure is released although the fracture strength of the material decreases with future pressurization cycles.

# Chapter 3

# An experimental study of the eruption of mud volcanoes

## 3.1 Abstract

This chapter reports experiments and modelling aimed at understanding some of the processes involved in mud volcanoes. Experiments were carried out to explore the role of pressurisation in the source reservoir, and also to explore the role of gas supplied to the reservoir in driving the eruption of the mud. Further experiments were carried out using a Hele-Shaw cell filled with clay in which air was injected at the base of the cell to explore the dynamics of bubbles rising through clay mixtures of different water content and hence rheology. The mud used during the experiment is a mixture of bentonite and water with various mass fraction of bentonite, $S$. The experiments have revealed a number of key features of the eruption of a non Newtonian fluid from a pressurised reservoir along a conduit. First, there is a major difference in behaviour between high water content 'fluid' like clay-water mixtures with a low yield stress, and clay-water mixtures with a low water content which have a high yield stress.

The fluid-like mixtures erupted in response to an increase in the reservoir pressure, and the eruption was enhanced by the addition of a gas flux. Also, the bubbles of gas tended to rise through the clay leading to intermittent small surface explosions superposed on a relatively steady outflow of clay. This eruption condition is defined as a type A eruption and is reminiscent of early phases of eruption at Lusi in Indonesia. In contrast, with the water-poor mixtures, no eruption occurs until the reservoir pressure reaches a critical value controlled by the yield stress. The clay mixture then issues from the reservoir and the flow persists until the reservoir pressure falls to a lower value at which there appears to be a dynamic yield stress condition and the flow stops.

In the case that gas is added to the reservoir this leads to additional pressurisation and in some cases horizontal fracture of the clay, with the overlying clay being lifted up the conduit and erupting from the conduit, thereby relieving the pressure. This eruption type is defined as type B which is characterised by a complex time history of episodic eruptions.

A simplified regime diagram is developed and used to help interpret some field observations in terms of the experimental results. The first three months of the Lusi activity were characterised by a continuous eruption which ejected about $3 \times 10^6$ m$^3$. This type of eruption is consistent with a relatively high reservoir pressure and possibly low viscosity fluids. The second stage of activity at Lusi fluctuates suggesting that the clay in the conduit is de-watering and strengthening and the reservoir pressure has decreased. The fluctuations of the yield stress, which depends on the shear $\Delta P$, cause a cyclic pattern of eruptions providing a mechanism which may be related to the episodic nature of eruption at some mud volcanoes.

## 3.2 Introduction

Gas flow through non-Newtonian media and in particular layers of clay is a subject of great interest in a wide range of fields such as petroleum geology, waste disposal engineering and marine science. One natural phenomenon of great interest is the process of eruption at a mud volcano.

Mud volcanoes are formed as a result of eruptions of argillaceous media stored deep underground in mud reservoirs (between 0.5 and 5 km, Dimitrov [21]). Although they present with a large variety of forms, such as geometry, eruption type, mud breccia, there are some common characteristics. Most of the volcanoes are located along the compressional belts where the mud reservoir consists of low density clay-water mixtures covered by dense sediments. There are often hydrocarbon sources near mud volcanoes (Dimitrov [21]). Mud eruptions are caused by a combination of effects such as mud buoyancy, pore fluid pressure, gas generation, tectonic compression and possibly seismic activity.

The scientific literature includes numerous investigations which explore these natural phenomena (Kopf [37]) and particular attention has been paid to the source feeding mud eruptions (Shirzaei et al. [73]) and the dynamics of mud breccia flowing from the conduits (Manga and Bonini [47]). Other work has focused on predictions of the future evolution or the identification of eruption patterns (Rudolph et al. [67]) including the influence of seismic activity (Bonini et al. [7], Rudolph and Manga [66]).

Methane emitted during eruptions suggests that mud volcanoes are frequently located near natural gas resources and that the gas flow, together with the pore fluid pressure, are important factors involved in formation and eruption of a mud volcano. The rise of bubbles in mud columns have been studied by a number of researchers. Talaia [74] investigated the gas rise speed through fluids of different viscosity identifying equations for the rising speed depending on the Reynolds number. Tran et al. [77] investigated the mobilization of gas and rigid particles as a function of yield stress in mud suspensions and Boudreau [8] considered the degassing process within soft cohesive sediments where the fracture toughness influenced the shape of bubbles which often formed oblate shapes. However, I am not aware of any experiments in which clay-water mixtures were driven by gas and pressure along a conduit, driving a mud-volcano type eruption and this forms the main theme of this chapter.

I explore some of the processes involved in the eruption of clay-water mixtures caused by reservoir pressurization and gas outflow through a conduit using a series of simplified experiments. The analysis of the results provides a classification of the processes in terms of some of the key controlling parameters in the experiments. After describing the experimental apparatus, the flow of gas through clay is described by initially discussing a two-dimensional experimental apparatus in which gas flows through a Hele-Shaw cell filled with clay. The experiments are run using different clay mixtures and various gas volume flow rates $Q_g$. The data from the experiments differ between high water content clays (liquid-like material) and low water content clays (gel-like material). These experiments are relevant for interpreting mud eruptions in systems in which there is a dominant release of gas relative to the mud erupted.

A second experimental apparatus is used to measure mud outflow from a conduit caused by pressurisation of the mud in a source reservoir and gas injection into the reservoir. The experiments illustrate three different flow regimes which may develop. (i) The over-pressured regime in which pure mud is pushed through the conduit by the pressure difference between the reservoir and the conduit. (ii) The over-pressured gas regime in which gas flow through the mud in the conduit produces a buoyancy force in addition to the reservoir overpressure. In this case both gas and mud erupt from the conduit. (iii) The gas-driven regime in which the buoyancy force of the gas drives the eruption even though the reservoir is under-pressured. The experiments are run using clay-water mixtures of different concentration and various flow rates $Q_g$. Particular interest is given to the effect of the yield stress distinguishing between the liquid-like and gel-like regimes. The discussion is concluded by comparing data from the Lusi mud eruptions with a numerical model derived from the experimental results.

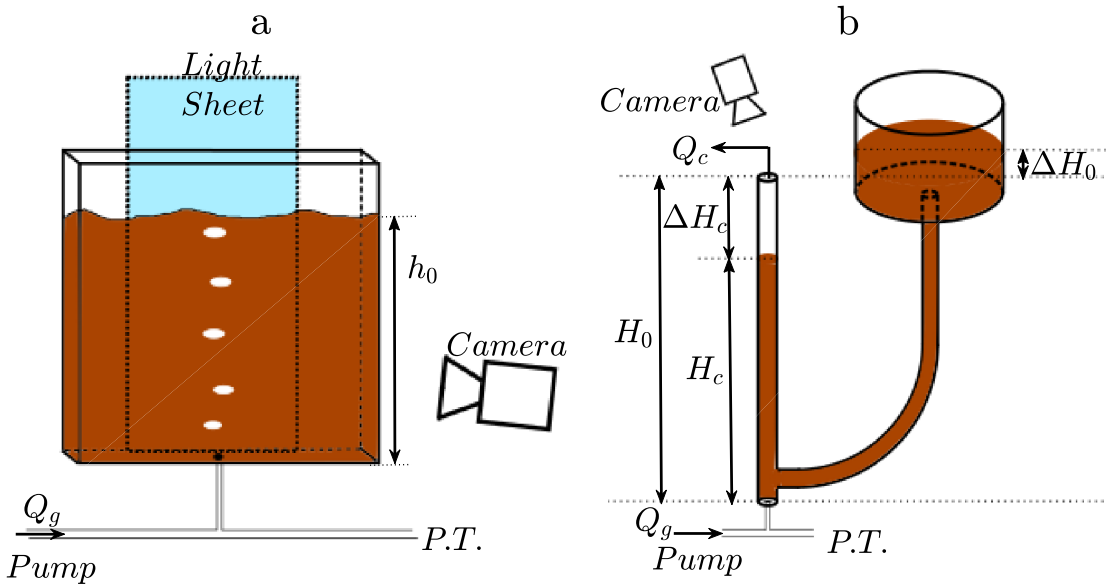


Fig. 3.1 (a) Schematic of the 2D cell for the bubble visualisation. (b) Schematic of the vertical pipe experimental apparatus.

## 3.3 Experimental apparatus

This section discusses the clay-water mixture (§3.3.1) used for the experimental study reported in this chapter before illustrating the two apparatuses used for the experiments (§3.3.2 and §3.3.3).

### 3.3.1 Clay-water mixture

The clay used during the experiments is a mixture of bentonite and water with a variable mass ratio ($0 \geq S \geq 0.15$), where $S$ is defined as the ratio between the mass of bentonite and the total mass of the mixture. Properties of the clay such as elastic modulus ($G'$), viscosity ($\mu$) and yield stress ($\sigma_y$) have already been discussed in chapter §2.3. It is important to note that the clay yield stress acts as a threshold which prevents fluid flow. Only when the pressure gradient is higher than the yield stress can the clay deform and flow.

| Exp | S | Exp | S | Exp | S | Exp | S |
|---|---|---|---|---|---|---|---|
| 1 | 0 | 5 | 0.04 | 9 | 0.08 | 13 | 0.12 |
| 2 | 0.01 | 6 | 0.05 | 10 | 0.09 | 14 | 0.13 |
| 3 | 0.02 | 7 | 0.06 | 11 | 0.1 | 15 | 0.14 |
| 4 | 0.03 | 8 | 0.07 | 12 | 0.11 | 16 | 0.15 |

Table 3.1 A summary of the experiments with the Hele-Shaw set up (Figure 3.1a) specifying the mass fraction of clay ($S$); each experiment was run for gas flow rates $Q_g = [0.1, 0.25, 0.5, 1, 2, 3, 4, 5]$ cm$^3$/s

### 3.3.2 Hele-Shaw experiments for gas explosions

In order to observe the gas flow through clay it was convenient to use a two-dimensional experimental apparatus (Figure 3.1a). This experimental system consists of a vertical Hele-Shaw cell of dimension $54 \times 54$ cm with a 5 mm gap filled with clay up to a height of about 45 cm ($h_0$). Gas is injected from a nozzle 2.4 mm in diameter ($d_0$) placed at the centre of the bottom of the cell. The gas source is connected to a pressure transducer, with range $\pm$30 kPa (*P.T.* Fig 3.1a), and two syringe pumps (NE-1050: World Precision Instruments) providing a constant gas volume flow ($0.1 \leq Q_g \leq 5$ cm$^3$/s). The experiments are backlit by a light sheet (W&Co LED panel $40 \times 60$ cm) and are recorded by a camera (Nikon D5300) with a 24 Hz video frame rate. This 2D experimental set up allows visualisation of the bubbles rising in clay and the flow generated by the bubbles. A systematic series of experiments were run in which the gas injection rate and the bentonite content of the clay-water mixture were varied. The experiments included the liquid-like regime ($0 \leq S \leq 0.07$) and the gel-like regime ($0.07 \leq S \leq 0.15$). The experiments discussed using this apparatus are listed in table 3.1.

### 3.3.3 Mud eruption experiments

In order to study mud eruptions, a different apparatus was developed to model the combined system of a deep mud reservoir and a conduit to the surface. The apparatus consists of a vertical perspex tube 1 m long ($H_0$) and of 2 cm inner radius ($R_0$) (Figure 3.1b). The mud is stored in a wider reservoir, 28 cm in diameter ($D_r$), which is connected to the base of the conduit by a flexible tube 1.6 m long and with inner diameter of 2.2 cm. The pressure at the base of the conduit is given by the hydrostatic pressure resulting from the elevation of the reservoir relative to the top of the pipe $\Delta H_0$ (see figure 3.1b). The gas injection source consists of a 5 mm diameter nozzle placed

at the center of the base of the pipe. Two syringe pumps (NE-1050: World Precision Instruments) connected to the nozzle push gas into the domain with alternating cycles in order to keep a constant flow rate ($0.1 \leq Q_g \leq 5$ cm$^3$/s). The injection point is also connected to a pressure transducer (*P.T.* Figure 3.1b), provided by Honeywell with range $\pm$30 kPa, for pressure readings. The clay outflow at the top of the pipe is collected on a digital balance which measures the weight of the erupted material ($M_c$) with an acquisition frequency of 1 Hz. The balance allows measurement of the erupted clay volume flux ($Q_c$). During each experiment the top of the conduit is recorded using a camera (Nikon 5300) with a 24 Hz frame speed in order to measure the frequency ($f$) of the bubbles bursting at the top of the clay column. A series of experiments were conducted to measure mud eruptions for different water content clays between the liquid and viscous regime ($0 \leq S \leq 0.15$). The experiments are also run for different reservoir heights ($H_0$) and gas injection flow rates ($Q_g$) to quantify the effects that mud pressurisation and gas flow have on the mud eruptions. Before starting the experiments the conduit is filled with clay up to a relative height from the conduit top $\Delta H_c$ (Figure 3.1b).The preparation before the experiments varies depending on the eruption regime and will be described in §3.5.1. The experiments run using this experimental equipment are listed in table 3.2.

## 3.4 Two-dimensional gas flow through clay

This section investigates cyclic gas eruptions at the top of a clay-water mixture resulting from a steady source of gas at the base of the layer, with the gas ascent through the clay driven by buoyancy. The discussion summarises the results obtained (§3.4.1) using the experimental apparatus described in §3.3.2 before giving an interpretation of the results obtained (§3.4.2) and their implications for natural phenomenon (§3.4.3).

### 3.4.1 Experimental results

The two-dimensional experimental apparatus, discussed in §3.3.2 (Figure 3.1a), allows a visual analysis of the fluid-dynamics involved in bubble rise through the bentonite-water mixture. The water content of the clay mixture has a strong influence on the flow (Figure 3.2, where $x$ and $z$ are the spanwise and streamwise distance from the injection point). Low viscosity clays ($0 \leq S \leq 0.07$) showed a liquid-like behaviour as a train of bubbles rises through the clay. However, the water content ($S$) of the clay affects the geometry and size of the bubbles. For $0.03 \leq S$, the bubbles seem to follow a specific

| Exp | S | $\Delta H_0$ | $\Delta H_c$ | Exp | S | $\Delta H_0$ | $\Delta H_c$ | Exp | S | $\Delta H_0$ | $\Delta H_c$ |
|---|---|---|---|---|---|---|---|---|---|---|---|
| 1 | 0 | -3 | -3 | 22 | 0.06 | -3 | -3 | 42 | 0.07 | 6 | 0 |
| 2 | 0 | -2.5 | -2.5 | 23 | 0.06 | -2.5 | -2.5 | 43 | 0.07 | 7 | N.A. |
| 3 | 0 | -2 | -2 | 24 | 0.06 | -2 | -2 | 44 | 0.07 | 8 | N.A. |
| 4 | 0 | -1.5 | -1.5 | 25 | 0.06 | -1.5 | -1.5 | 45 | 0.07 | 9 | N.A. |
| 5 | 0 | -1 | -1 | 26 | 0.06 | -1 | -1 | 46 | 0.08 | 18 | -5.5 |
| 6 | 0 | -0.5 | -0.5 | 27 | 0.06 | -0.5 | -0.5 | 47 | 0.08 | 18 | -5 |
| 7 | 0 | 0 | 0 | 28 | 0.06 | 0 | 0 | 48 | 0.08 | 18 | -4.5 |
| 8 | 0 | 0.5 | N.A. | 29 | 0.06 | 4.5 | N.A. | 49 | 0.08 | 18 | -4 |
| 9 | 0 | 1 | N.A. | 30 | 0.06 | 6 | N.A. | 50 | 0.08 | 18 | -3.5 |
| 10 | 0 | 1.5 | N.A. | 31 | 0.06 | 6.5 | N.A. | 51 | 0.08 | 18 | -3 |
| 11 | 0 | 2 | N.A. | 32 | 0.06 | 7 | N.A. | 52 | 0.08 | 18 | -2.5 |
| 12 | 0.05 | -3 | -3 | 33 | 0.06 | 7.5 | N.A. | 53 | 0.08 | 18 | -2 |
| 13 | 0.05 | -2.5 | -2.5 | 34 | 0.07 | 2 | -4 | 54 | 0.08 | 18 | -1.5 |
| 14 | 0.05 | -2 | -2 | 35 | 0.07 | 2.5 | -3.5 | 55 | 0.08 | 18 | -1 |
| 15 | 0.05 | -1.5 | -1.5 | 36 | 0.07 | 3 | -3 | 56 | 0.08 | 18 | -0.5 |
| 16 | 0.05 | -1 | -1 | 37 | 0.07 | 3.5 | -2.5 | 57 | 0.08 | 18 | 0 |
| 17 | 0.05 | -0.5 | -0.5 | 38 | 0.07 | 4 | -2 | 58 | 0.08 | 19 | N.A. |
| 18 | 0.05 | 0 | 0 | 39 | 0.07 | 4.5 | -1.5 | 59 | 0.08 | 21 | N.A. |
| 19 | 0.05 | 0.5 | N.A. | 40 | 0.07 | 5 | -1 | 60 | 0.08 | 23 | N.A. |
| 20 | 0.05 | 1 | N.A. | 41 | 0.07 | 5.5 | -0.5 | 61 | 0.08 | 24 | N.A. |
| 21 | 0.05 | 1.5 | N.A. | | | | | | | | |

Table 3.2 A summary of the experiments carried out in the vertical pipe apparatus (Figure 3.1b) specifying the mass fraction of clay ($S$), and the height relative to $H_0$ of the mud source ($\Delta H_0$) and the mud column ($\Delta H_c$) both reported in cm. Each experiment was run for gas flow rates $Q_g = [0, 0.1, 0.25, 0.5, 1, 2, 3, 4, 5]$ cm$^3$/s

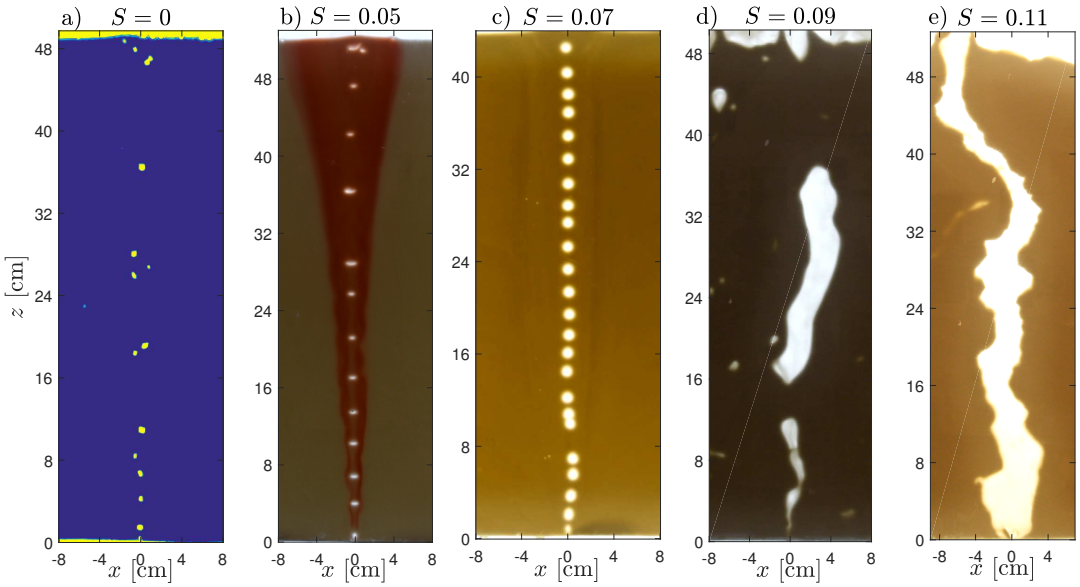


Fig. 3.2 (a-e) Front view frames of gas injections ($Q_g = 1$ [cm$^3$/s]) in various bentonite concentration mixtures ($S$) obtained during the two-dimensional experiments (Figure 3.1a). Figure 3.2a uses false colour resolution to better identify the volume occupied by gas compared to water ($S = 0$).

path (Figure 3.2b and c), while, for $0 \leq S < 0.03$ (Figure 3.2a), the horizontal position of bubbles is more variable. These results are similar to the results of Krishna and Van Baten [40] for bubbles rising in water. In the case of thicker clays ($0.08 \leq S \leq 0.1$) the fluid shows gel-like properties. The fracture strength of the fluid increases with $S$ and as a result the bubble shape changes from almost round shapes into long elongated slugs (Figure 3.2d). With higher clay content mixtures ($S > 0.1$) the gas seems to form fracture like channels in the clay along which it propagates. The slugs no longer migrate and instead remain open all the way to the top of the cell (Figure 3.2e).

The discussion now focuses on the liquid-like regime ($0 \leq S \leq 0.08$). A relatively small gas volume flow rate ($Q_g \leq 0.5$[cm$^3$/s]) consists of circular bubbles rising from the injection point at an almost constant speed and the bubbles behave independently from each other (Figure 3.3a and b). Increasing the gas flow rate reduces the distance between bubbles and, when it exceeds a critical flow rate, bubbles merge while rising along the conduit. The merging of bubbles also affects their geometry which switches from a circular shape (Figure 3.3a-c) into an half-cup geometry (Figure 3.3c-e). This is similar to rise of bubbles in water (Krishna and Van Baten [40]).

Integrating the light intensity captured by the camera during each experiment and applying an appropriate threshold it was possible to identify the vertical location of bubbles over time. Figure 3.4a is a grey-scale plot showing the vertical position of gas

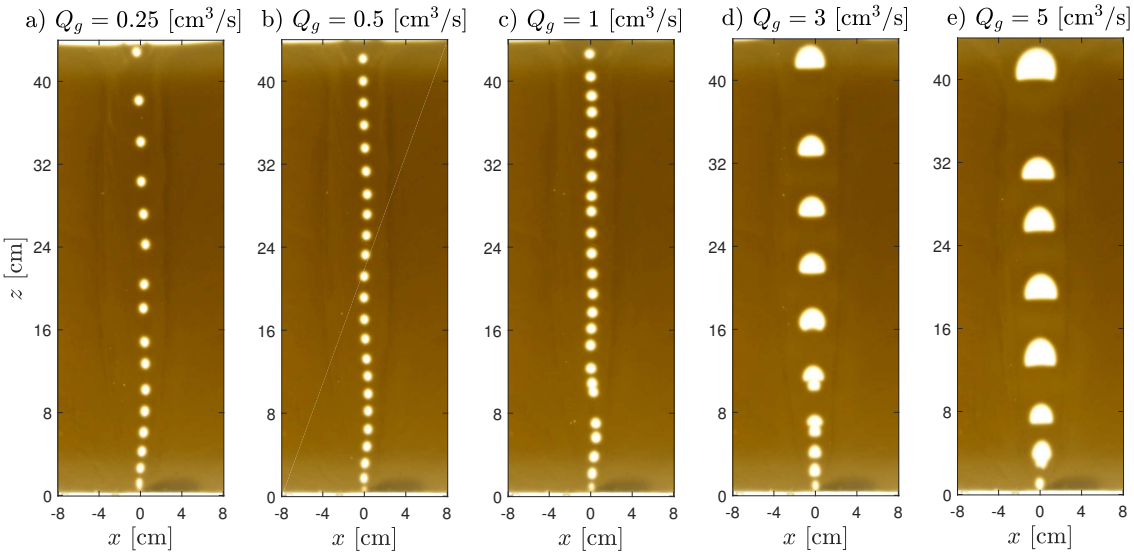


Fig. 3.3 (a-e) Sequence of images of the two-dimensional experiments (Figure 3.1b) with different gas injection flow rates ($0.25 \leq Q_g \leq 5$ [cm$^3$/s]). The frames were taken during an experiment using clay with $S = 0.07$.

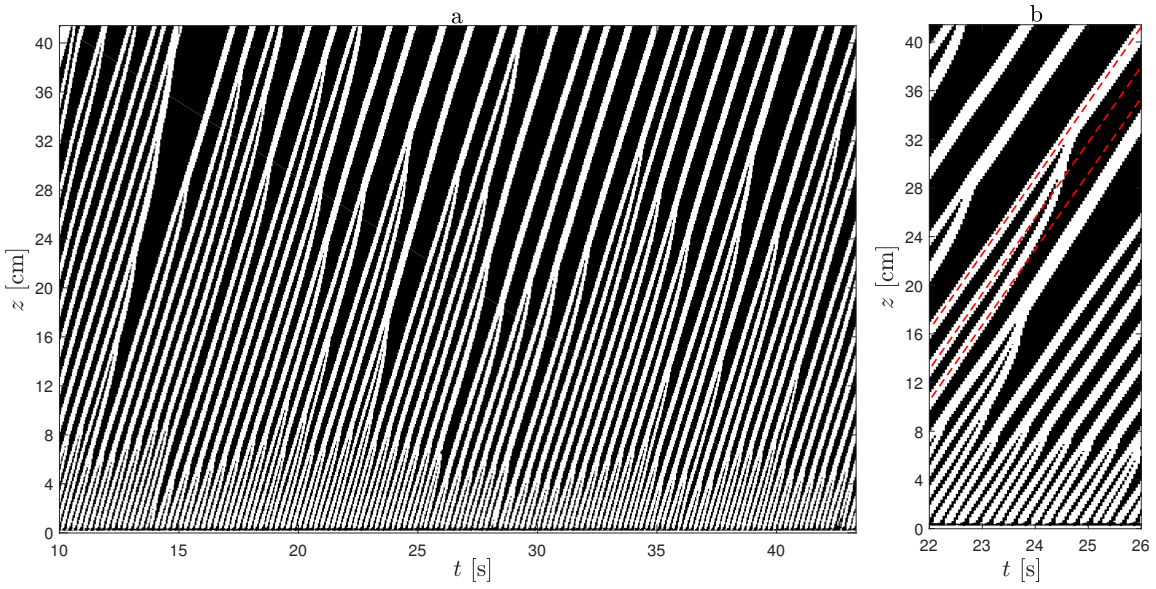


Fig. 3.4 (a) Time series of a vertical line through the train of bubbles, illustrating the rising position of the bubbles over time and their random merging. (b) Section of figure 3.4a focusing on the merging between bubbles and their speed variations compared to their initial speed (red dashed lines). The red dashed lines show the position of the bubbles in the case of constant rise speed for each bubble. The data shown in both figures have been obtained during an experiment with $Q_g = 2$ cm$^3$/s and $S = 0.07$.

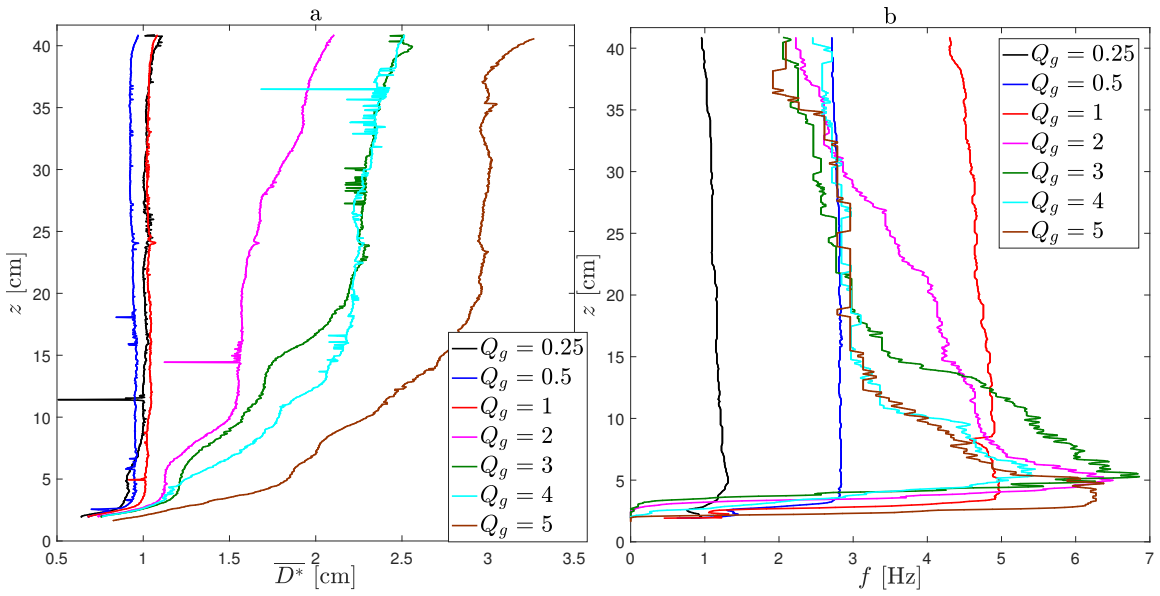


Fig. 3.5 (a) Plot of the bubbles averaged equivalent diameter $\overline{D^*}$ as a function of $z$ for a range of gas injection flow rates $Q_g$. (b) Plot of the time-averaged frequency $f$ of the bubbles as a function of $z$ measured during a series of experiments with different gas injection flow rates $Q_g$. The data shown in panels a and b was collected from a 2-D experiment with $S = 0.07$

bubbles as a function of time. Figure 3.4b suggests that the effect of the wake of a bubble on a following bubble causes the rise speed of the following bubble to increase leading to the merging. The merging causes variations of the bubble diameter along the conduit but it does not significantly affect the rise speed which remains nearly constant and similar to the speed of the bubble before the merging event. This result is consistent with the result for gas bubbles rising in newtonian fluids such as water (Haberman and Morton [28]).

Data concerning the geometry, frequency and speed of the bubbles will now be discussed in order to identify a pattern for the merging of bubbles. The frequency of the bubble as a function of height above the source, $z$, is measured by counting the number of bubbles passing through a horizontal line at height $z$ above the source of gas during the whole duration of the experiment and the equivalent diameter $D^*$ is given by $D^* = \sqrt{4A_b/\pi}$ where $A_b$ is the bubble area. Merging of bubbles reduces their frequency and increases their diameter $D^*$ along the height $z$. As shown in figure 3.5, the time averaged equivalent diameter ($\overline{D^*}$) and the frequency $f$ remain independent of $z$ for relatively low values of gas flow rates ($Q_g \leq 1$ [cm$^3$/s]) and while the frequency increases with $Q_g$ the diameter is almost independent of $Q_g$. With relatively high gas flow rate ($Q_g \geq 2$ in case of $S = 0.07$ as shown in figure 3.3 and 3.5) merging of bubbles

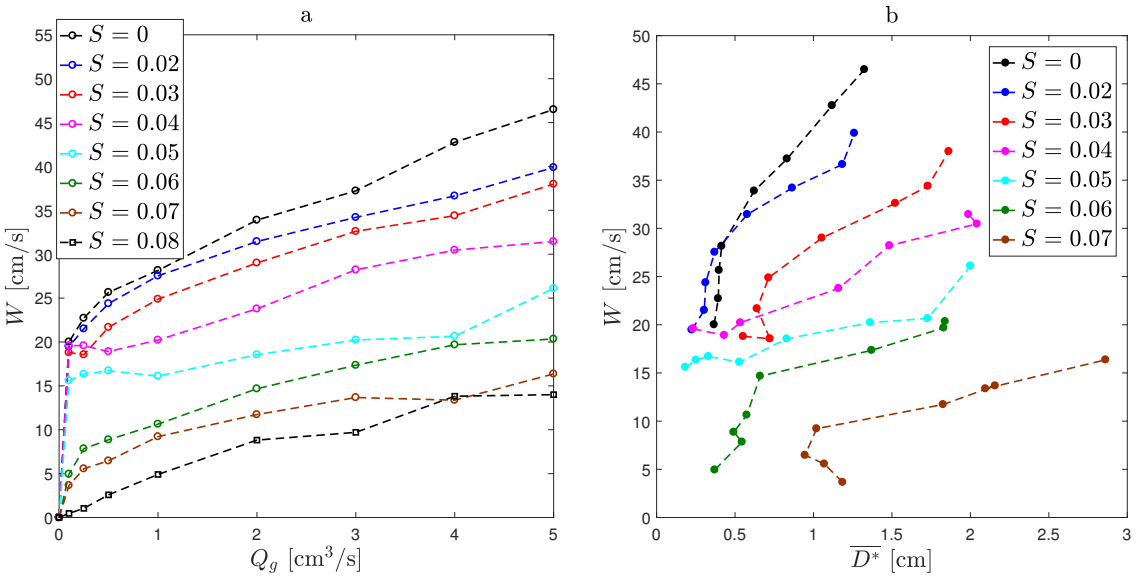


Fig. 3.6 (a) Plot of the vertical speed of the bubbles $W$ as a function of the gas flow rate $Q_g$ for various bentonite content clays $S$. (b) Plot of the vertical speed of the bubbles $W$ compared to the average diameter of the bubbles $\overline{D^*}$ bursting at the top of the domain ($z = h_0$).

is observed. The merging causes the averaged bubble diameter ($\overline{D^*}$) to increase with $z$ (Figure 3.5a) while the frequency $f$ reaches a maximum value, within the first 5cm from the injection source, before gradually decreasing with height (Figure 3.5b). The initial increase of frequency is caused by the establishment of the flow at the base of the domain.

Applying a Hough transform on the time lapse images (Figure 3.4) enables to determine the average rise speed $W$ of bubbles for each experiment as shown in figure 3.6. This figure shows that, as the bentonite content of the clay mixtures increases ($S$), the speed decreases. The increasing density and viscosity of the material reduces the bubble speed from $32 \pm 12$cm/s with $S = 0$ down to $8 \pm 7$ cm/s (figure 3.6a) when $S = 0.08$. The bubble rise speed increases with the bubble diameter and an increase in the gas flow rate causes a systematic increase in the bubbles' speed as shown in figure 3.6a and b.

### 3.4.2 Data interpretation

Figure 3.7 shows the averaged frequency ($f(z)$) of bubbles bursting at the top of the domain ($z = h_0$) and the time-averaged equivalent diameter ($\overline{D^*}(z = h_0)$). As described in §3.4.1, the frequency of bubbles, for relatively low gas injection flow rate,

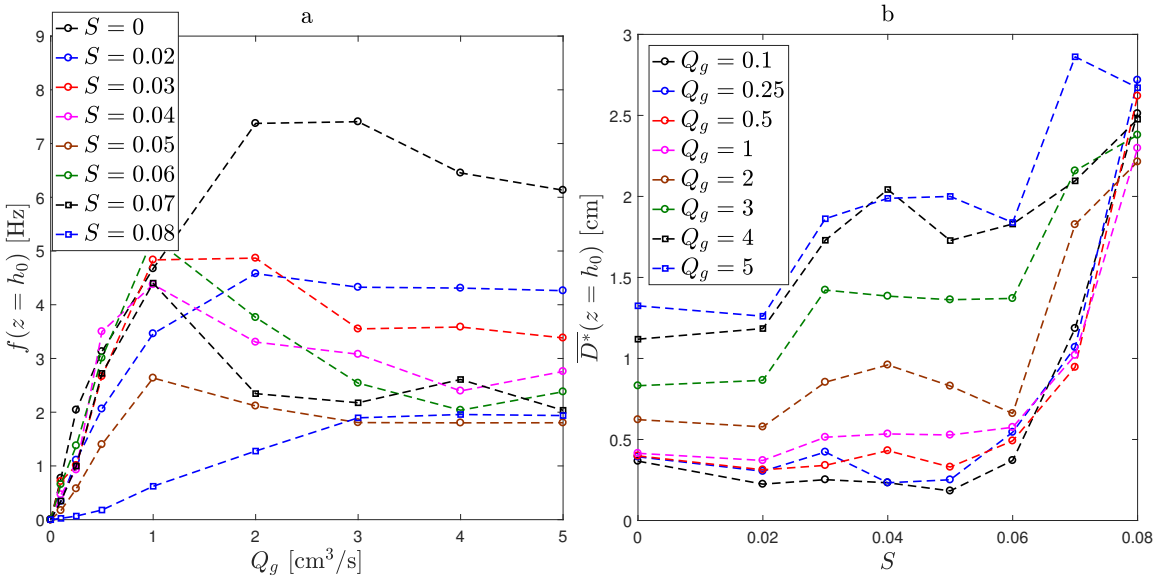


Fig. 3.7 (a) Time-averaged frequency $f$ of the gas bubbles bursting at the top of the domain ($z = h_0$) as a function of the gas injection flow rate $Q_g$ for various bentonite concentration mixtures ($S$). (b) Plot of the average diameter $\overline{D^*}$ of the bubbles reaching the top of the domain as a function of the clay content of the clay-water mixture, $S$, with various gas injection flow rates ($Q_g$).

increases proportionally with $Q_g$ because the bubbles rise independently from each other. The merging of bubbles with height causes the frequency of bubbles at $z = h_0$ to reduce (Figure 3.7a). It is then possible to identify the critical flow rate $Q_{cr}$ as the gas flow rate at which the frequency $f(z = h_0)$ reaches its maximum. The critical gas flow rate $Q_{cr}$ tends to decrease from 3 cm$^3$/s for $S = 0$ to 1 cm$^3$/s for $0.04 \leq S \leq 0.07$. The diameter of the bubbles reaching the top of the domain remains approximately constant for $S \leq 0.05$ and $Q_g \leq Q_{cr}$ (Figure 3.7b). Increasing the flow rate beyond the limit $Q_{cr}$ causes the final diameter to increase as bubbles merge while rising from the source. For more dense clays ($S > 0.05$) the diameter tends to increase because the clay-water mixture evolves from being a pure liquid to behaving as a gel-like material. This causes the bubbles to switch from an almost circular shape into an elongated slug shape (Figure 3.3).

The non dimensional distance between two bubbles at the top of the domain $L_{cr}/\overline{D^*}(z = h_0)$, where $L_{cr} = W/f(z = h_0)$, decreases significantly with the injection flow rate when $Q_g \leq Q_{cr}$. Above the limit $Q_{cr}$ the gas flow does not significantly affect the distance between bubbles which remains approximately constant (Figure 3.8).

Gas flow rates higher than $Q_{cr}$ lead to a short distance between bubbles at the injection point causing the bubbles to be affected by former bubbles. When one bubble

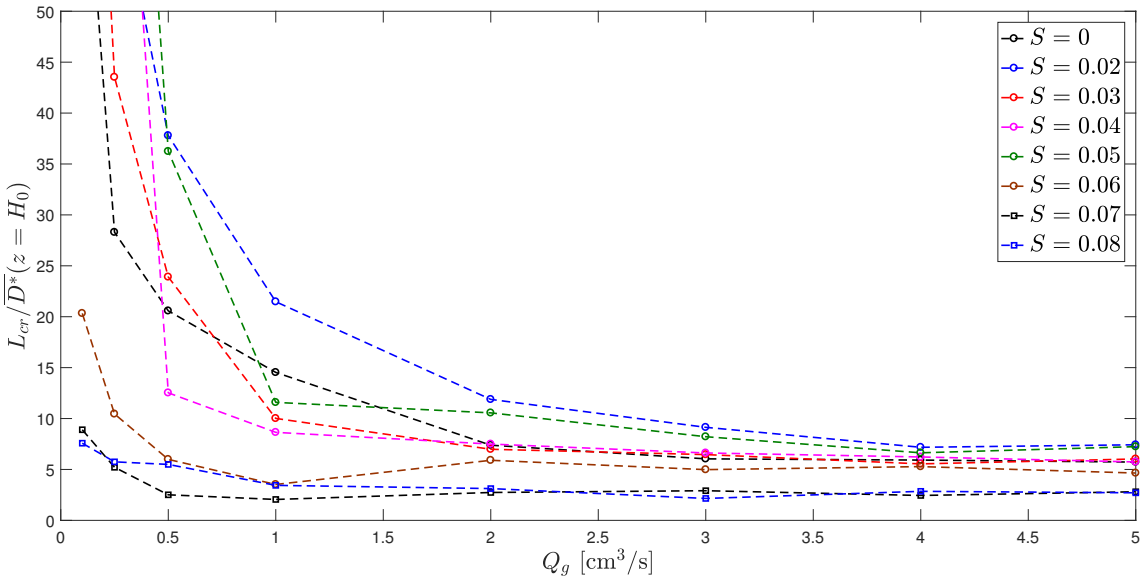


Fig. 3.8 Plot of the ratio of the distance ($L_{cr}$) between successive bubbles and their diameter $\overline{D^*}$ at the top of the domain ($z = h_0$). Increasing the gas flow rate causes the distance between bubbles to reduce to a minimum, below which the merging of bubbles commences.

is trapped in the wake of the preceding bubble, its rise speed increases leading to merger of the two gas volumes. It is also possible that the viscosity of clay may locally reduce because of the shear applied on the clay by the bubble passage. The data show that with a relatively high flow rate of gas bubbles rising through clay, bubble merging leads to a minimum distance $L_{cr}$ whereas, at low flow rate, there is less merging and a constant train of smaller bubbles develops.

The data suggest that, for $Q_g \leq Q_{cr}$, the bubble diameter $\overline{D^*}(z)$ is constant and possibly depends on the surface tension between the two fluids. In this case $f = 4Q_g/(\pi\overline{D^*}^2\tau)$ and $L_{cr} = W/f$ are constant independent of $z$, where $\tau$ is the cell gap. When $Q_g \geq Q_{cr}$ both frequency and diameter vary with height but the distance between bubbles tends to a minimum value given by $L_{cr} = W\pi\overline{D^*}^2_{cr}\tau/(4Q_g)$, where $\overline{D^*}^2_{cr}$ is the average diameter for gas flow rates lower than $Q_{cr}$. The final values of $f(z)$ and $\overline{D^*}(z)$ at the top of the flow cell are given by $f(h_0) = W/L_{cr}$ and $\overline{D^*}(h_0) = \sqrt{4Q_gL_{cr}/(W\pi\tau)}$. Figure 3.5b suggests that the merging becomes progressively more gradual with height in the cell and so these values may be close to the limit in the far field, although without a taller experimental system it is not possible to test whether the merging process continues. The bentonite content of the mud mixture in the liquid regime, $S \leq 0.05$, does not significantly affect the volume of

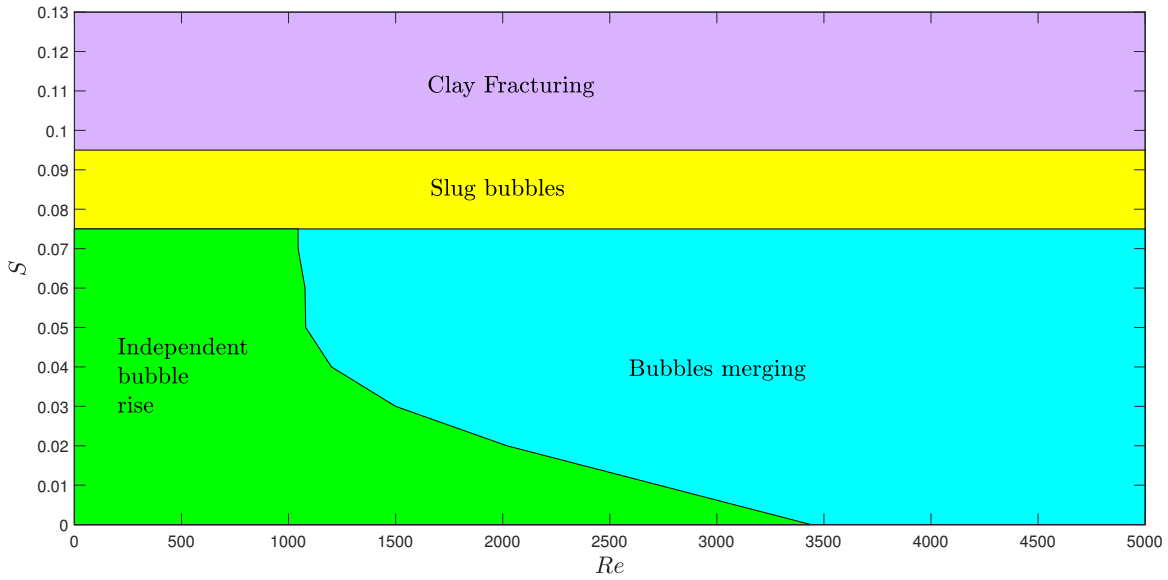


Fig. 3.9 Diagram illustrating the four regimes of gas flow through clay in the two-dimensional experimental apparatus. These depend on the consistency of the clay-water mixture ($S$) and the Reynolds number of the gas reaching the top of the clay ($Re$).

the bubbles (Figure 3.7b) but the increasing viscosity significantly reduces their rise speed (Figure 3.6a).

### 3.4.3 Conclusions

The experimental data suggest an approximate regime diagram (Figure 3.9) which describes the transitions in the gas flow through clay depending on the concentration of the clay-water mixture ($S$) and the Reynolds number of the bubbles bursting at the top of the clay column, given by

$$Re = \frac{\rho_c W \overline{D^*}(z = h_0)}{\mu}$$

For high water content clays in the liquid regime ($S < 0.075$) low Reynolds gas bubbles rise independently from the previous bubble. High Reynolds bubbles are affected by the wake of the former bubble rise and locally increase their speed causing the merging of bubbles. The transition between the two regimes has been obtained by measuring the Reynolds number for $Q = Q_{cr}$ for various $S$. Increasing the concentration of the clay-water mixture ($0.075 < S < 0.095$) increases the fracture strength of the material which deforms the bubbles into an elongated slug shape while rising through the clay.

High bentonite content mixtures show gel-like properties and gas flows through the material by forming a fracture-like channel.

These results describe the flow of gas through mud conduits depending on the gas flow rate at the source and the clay rheology. The data is consistent with observations from the Dashgil mud volcano in Azerbaijan (Hovland et al. [32]). This mud volcano conduit consists of a system of three salses and roughly 20 gryphons. Salses and gryphons are two different structures formed by the mud outflow. Salses resemble a pool - relatively flat and wide (between 4m and 9m in diameter) - filled with relatively low viscosity mud. Gryphons consist of a mud cone, up to 3 meters high, and a hole at the top of the cone. The holes are relatively narrow (less than 1m diameter) when compared with the size of the base of the cone, which typically range between 1 and 9 m in diameter.

The gas outflow from the gryphons varies depending on the viscosity of the mud. Low viscosity gryphons are characterised by small size bubbles (between 0.5 and 3 cm in diameter) erupting at the top of the conduit continuously and with an almost constant frequency. The gas eruptions from high viscosity gryphons consist of large size bubbles (between 1 and 40 cm in diameter) and the frequency of the eruptions has been defined as "highly erratic" (§2.3 in Hovland et al. [32]). The gas burst events in the high viscosity gryphons have 10 minute intervals and each bursting is followed by 3-5 large bubbles erupting shortly after the first one. Supposing a constant gas source for both types of eruption, the results suggest that the high viscosity clay leads to merger of bubbles and possibly the formation of bubble slugs which slowly emerge through the clay while the low viscosity muds are crossed by a train of gas bubbles with constant frequency.

In concluding we note that, using a higher clay column, in some cases the merging may continue resulting in the final bubble merging condition being different. Also the fracture-like channel may periodically close, as with the process described in chapter 2, but now driven by the large hydrostatic pressure.

## 3.5 Vertical conduit experiments

The discussion of a mud eruption through a vertical conduit starts by illustrating the results obtained from the experimental apparatus described in §3.3.3 (Figure 3.1b). The experiments are run using a range of initial conditions as discussed in §3.5.1. The results from the various experiments are then summarised and processed in §3.5.2. The interpretation of these results is followed by a description of the eruptive behaviour

of mud volcanoes §3.6.1 and the formulation of a numerical model in §3.6.2. The discussion is then concluded with a comparison of data from mud volcanoes and in particular from the Lusi mud eruptions in §3.7.

### 3.5.1 Experimental results

The description of the experimental results starts by considering the case of cyclic eruptions during one experiment where the reservoir pressure was gradually increased in order to generate an eruption. The mud outflow causes the reduction of the reservoir clay level until the eruption stops. The cycle is repeated by gradually increasing the pressure at the base of the conduit. The experimental procedure then evolved to include three different experiments aiming to study the evolution of an eruption starting from a steady state condition. (i) The over-pressured regime studies the evolution of the mud outflow as a function of the reservoir pressure starting from a steady eruption stage. (ii) The over-pressured gas regime investigates the effect of a steady gas flow supplied at the base of the conduit in addition to the effects of pressurisation of the source reservoir. (iii) The under-pressured gas regime studies the eruption caused by pure gas flow through stagnant mud in the conduit. These three experimental regimes are explored considering a systematic series of experiments with various clay mixtures ($S$), reservoir heights ($\Delta H_0$) and gas flow rates ($Q_g$) as listed in table 3.2.

#### Cyclic eruptions

Figure 3.10b shows the mass erupted ($M_c$, blue line in figure 3.10b) and the reservoir height ($\Delta H_0$, black dashed line in figure 3.10b) over time ($t$) for five cyclic eruptions ($A - E$ in figure 3.10b) obtained during an experiment with a relatively viscous clay ($S = 0.08$). The reservoir is initially held at a height ($\Delta H_0$, figure 3.10a) of 14 cm above the top of the conduit which is filled with clay but the clay does not erupt from the conduit. From this initial stable condition at $t = 0$ the reservoir is then lifted gradually by 1 cm every 30 seconds using a calibrated height adjustable base. Once the reservoir is lifted to a critical value of 28 cm the first eruption cycle ($A$) spontaneously starts and the reservoir height $\Delta H_0$ is then held constant. During the eruption the clay flows from the reservoir into the conduit and gradually empties the tank. The level of the clay in the reservoir reduces and the height between the top of the conduit and the height of the clay in the reservoir $\Delta H$ (black solid line in figure 3.10b) is given by $\Delta H(t) = \Delta H_0 - 4M_c(t)/(\pi D_r^2)$. The eruption stops once the actual height of the mud in the reservoir $\Delta H$ is lower than a second critical value (slightly above 25.7 cm). Once

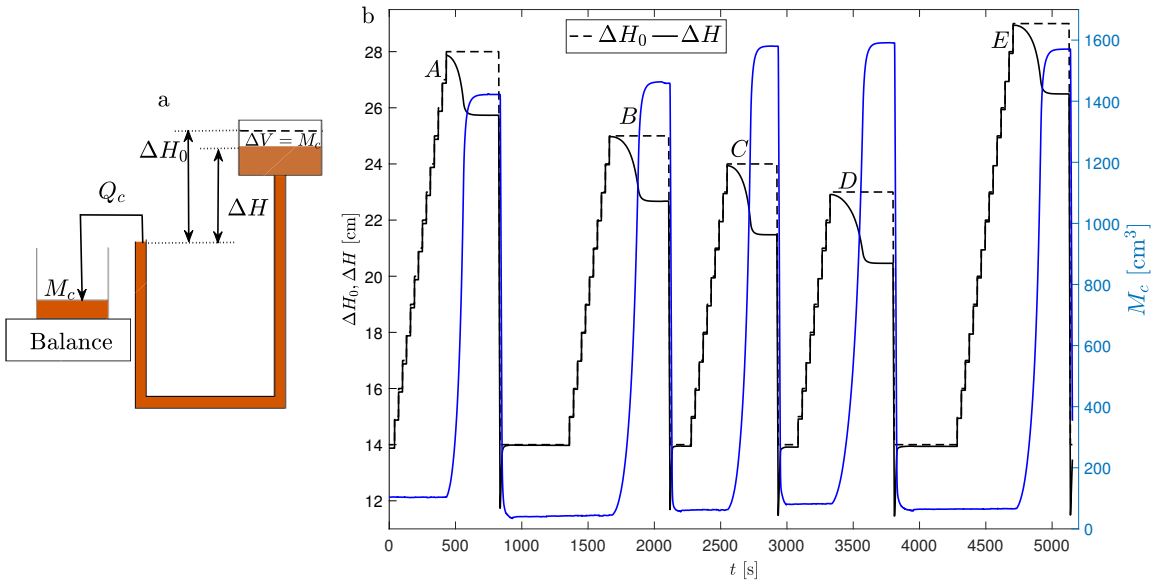


Fig. 3.10 (a) Schematic of the experimental apparatus for the cyclic eruption regime. (b) Plot of the reservoir height ($\Delta H_0$), the height of the clay level in the reservoir ($\Delta H$) and the volume erupted $M_c$ as a function of time $t$ during 5 eruption cycles marked by the letters $A - E$. The data were obtained during an experiment using a clay-water mixture in which $S = 0.08$.

the eruption stops the height of the reservoir $\Delta H_0$ is reduced down to the initial value of 14 cm and the reservoir is refilled with most of the erupted clay ($\Delta H \approx \Delta H_0$). The process is than repeated for four cycles ($B - E$) after a short rest of about five minutes between each cycle. The critical heights, which characterise the beginning and ending of the eruption, vary for each cycle (between 22 and 28 cm for the case shown in figure 3.10b) and gradually reduce for each cycle except from the last case where a longer rest was taken (about 8 minutes) before lifting the reservoir. This experiment was repeated for bentonite-water mixtures with different concentrations ($0 \leq S \leq 0.08$). The critical heights increase with the clay consistency, from lower than 0.5 cm for $S \leq 0.05$ to $6 \pm 2$ cm for $S = 0.06$ and $25 \pm 4.5$ cm for $S = 0.08$.

Lifting the reservoir tank increases the pressure gradient between the reservoir and the conduit. The results suggest that the yield stress of the clay stops the fluid from flowing in the tank while the pressure gradient between the reservoir and the top of the conduit is lower than the yield stress. For clarity the future discussion will define the height of the reservoir in terms of the hydrostatic pressure of the reservoir $\Delta P$ relative to the pressure at the top of the conduit, defined as:

$$\Delta P = \rho_c g \Delta H \tag{3.1}$$

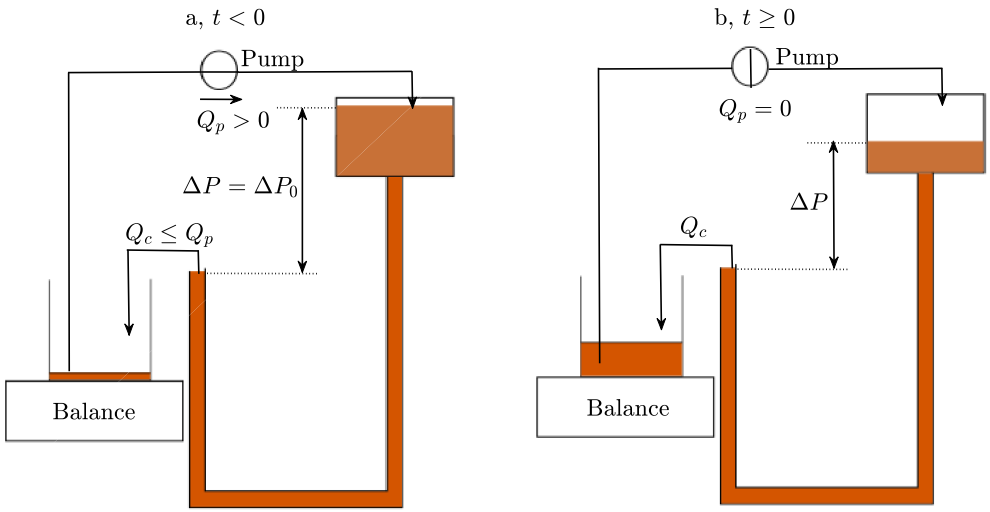


Fig. 3.11 Schematic of the steady clay eruption experiments in which a pump is used to refill the reservoir of erupted mud (a), and of the transient waning of the flow when the peristaltic pump is turned off and the eruption empties the reservoir tank (b).

where $\rho_c \approx 10^3$[kg/m$^3$] is the clay density and $g$ is the gravitational acceleration (Figure 3.10b). As described in the previous paragraph, the stress applied on the clay has to be higher than the yield stress in order to cause the clay to deform and flow. The critical heights which define the beginning and ending of the eruption, as described in the previous paragraph, will be defined as static yield stress $\sigma_{yS}$ and dynamic yield stress $\sigma_{yD}$. The static yield stress is considered as the height of the reservoir required to start the eruption multiplied by the clay density and acceleration due to gravity. In contrast the dynamic yield stress is defined as the height of the reservoir at which the eruption stops multiplied by the clay density and acceleration due to gravity.

### Over-pressured regime

The over-pressured regime considers the evolution of the mud eruption starting from a steady condition where both the reservoir pressure $\Delta P$ and the flow rate of the clay erupted $Q_c$ are constant. As discussed for the cyclic eruption regime the eruption starts by increasing the relative hydrostatic pressure beyond the point $\Delta P = \sigma_{yS}$. Once the pressure exceeds the static yield stress the clay flows from the reservoir into the pipe and out from the conduit as an eruption. The outflow is sustained while the pressure remains higher than the critical value $\sigma_{yD}$. In order to start the experiment from a steady condition it is necessary to use a peristaltic pump (Figure 3.11 a). Before

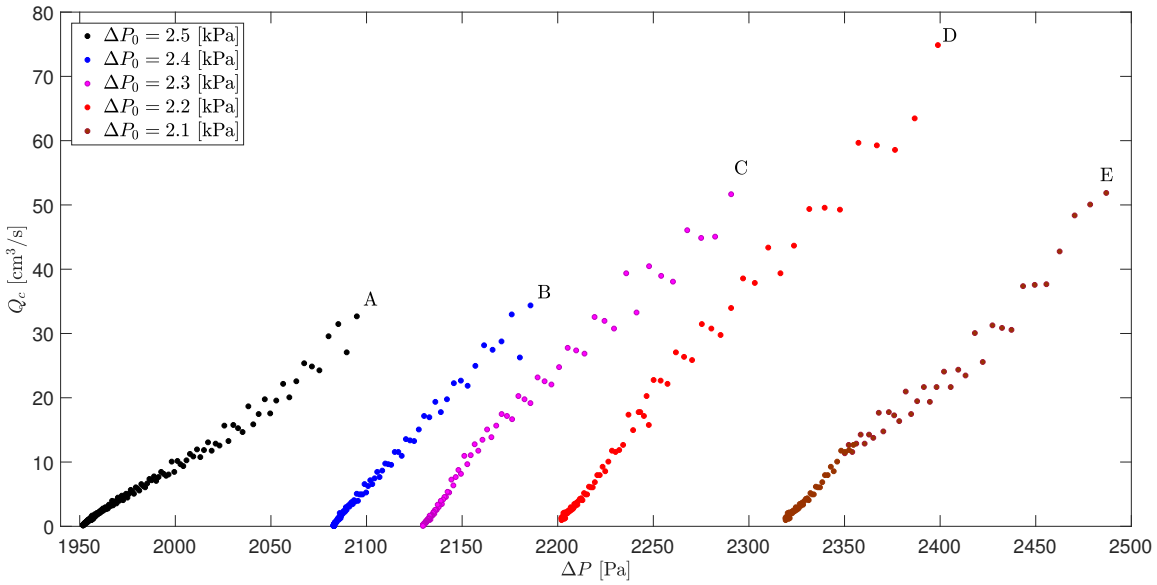


Fig. 3.12 Plot of the clay outflow rate $Q_c$ as a function of the reservoir pressure $\Delta P$ for 5 experiments (listed A-E) in the over-pressured regime with different initial conditions $\Delta P_0$ and $S = 0.08$.

starting the data acquisition, a peristaltic pump is used to move clay from the balance back into the reservoir with a maximum flow rate $Q_p = 80$ cm$^3$/s. The pump refills the reservoir with the clay ejected from the conduit and maintains a constant flow rate through the conduit. The experiment is initiated by lifting the tank to an overpressure of about 1 kPa in excess of the $\sigma_{yS}$ limit ($\Delta H - \sigma_{yS}/(\rho_c g) \approx 10$cm) and is then reduced to a lower initial value ($\Delta P_0 = \rho_c g \Delta H_0$), so that $0 \leq Q_c \leq Q_p$. The pressure $\Delta P_0$ is then kept constant for at least 5 minutes in order to allow the system to reach a steady flow condition. From the steady state condition the peristaltic pump is stopped ($t = 0$) and the data acquisition begins.

Figure 3.12 shows the clay flow rate $Q_c$ measured by the balance with the pressure $\Delta P$ during the eruption for five different experiments with $S = 0.08$. It is possible to consider the experiment D in figure 3.12 (red dots) as an example of the general behaviour of the experiments. Before starting the experiment the flow rate of the eruption is constant ($Q_c = 74.8$ [cm$^3$/s]) as is the pressure of the reservoir ($\Delta P = \Delta P_0 = 2.4$ kPa). When the pump is stopped the eruption gradually reduces the level of the clay in the reservoir $\Delta H$ causing a pressure reduction as given by equation 3.1. The flow rate $Q_c$ gradually reduces in proportion to the reservoir pressure $\Delta P$ and the eruption stops once the pressure reaches the dynamic yield stress $\sigma_{yD}$, which in this case is equal to 2.2 kPa. A systematic series of experiments (table 3.2) explored

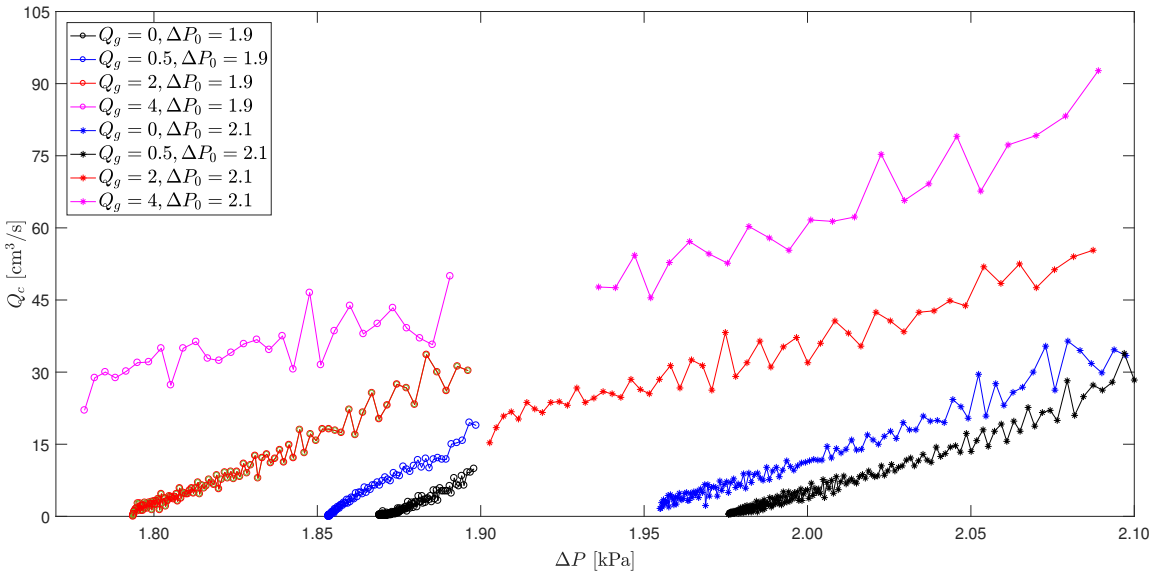


Fig. 3.13 Plot of the flow rate of clay erupted from the conduit $Q_c$ as a function of the reservoir pressure $\Delta P$ for 4 different values of gas flux $Q_g$ with $S = 0.08$ and $\Delta P_0 = 1.9$ and 2.1 kPa.

the behaviour of the flow-rate as a function of various initial conditions ($\Delta P_0$) and using clay-water mixtures with different concentrations ($S$). Figure 3.12 shows that the dynamic yield stress is not a constant value and the fluctuations in this critical value from cycle to cycle impact the variations in the flow rate from cycle to cycle. The behaviour of the dynamic yield stress will be subject of further discussion in §3.5.2 but the data suggest that $Q_c \propto (\Delta P - \sigma_{yD})$. The experiments were run for relatively high water content mixtures because for $S \geq 0.09$ the maximum height of the reservoir (approximately 60 cm), limited by the experimental apparatus, was not sufficient to start an eruption.

### Over-pressured gas regime

The over-pressured mud eruption is initiated with the same routine as described above in the over-pressured regime but now gas injection at the base of the conduit is started before stopping the peristaltic pump. After each experiment the routine is repeated and the gas flow rate is systematically increased ($0 \leq Q_g \leq 5$ cm$^3$/s). The gas flow is injected from two syringe pumps with a maximum capacity of 200 cm$^3$ of air at atmospheric pressure. Because of the finite gas volume, there is a maximum time for which it is possible to run the experiment and this depends on the gas flow rate $Q_g$. Once a series of experiments with various gas flow rates at the same initial height

$\Delta P_0$ is completed, a new series is started with a different initial condition $\Delta P_0$ (table 3.2). Figure 3.13 shows the measured clay outflow $Q_c$ for two series of experiments ($\Delta P_0 = 1.9$ and 2.1 kPa) and four different gas flow rates $Q_g$ for each series. The outflow $Q_c$ proportionally decays with the reservoir pressure $\Delta P$, as obtained in the over-pressured regime, and the gas injection systematically increases the clay outflow.

The bubble bursting on top of the conduit also causes fluctuations in the clay outflow. The oscillations in $Q_c$ increase with the gas flow rate from a value of $\pm 3.3$ cm$^3$/s, for $Q_g = 0.5$ cm$^3$/s, to $\pm 7.6$ cm$^3$/s, for $Q_g = 5$ cm$^3$/s (Figure 3.13). As discussed in §3.5.1, the clay outflow stops when the pressure is lower than the dynamic yield stress but the gas injection seems to reduce the value of the dynamic yield stress. Figure 3.13 shows that the reduction of the yield stress is dependent on the gas volume flow rate $Q_g$ for each set of experiments with the same initial condition $\Delta P_0$.

As discussed in the previous section the use of a dense clay ($S \geq 0.09$) with a high yield stress clogs the pipe connecting the reservoir to the vertical conduit and it is not possible to start an eruption as the static yield stress is higher than the maximum relative pressure allowed by the experiment (about 6 kPa). When gas is injected in the domain it increases the pressure at the injection point and cracks the clay horizontally near the base of the conduit. A continuous gas injection increases the pressure and lifts the clay as a solid block. As there is no flow of clay from the reservoir the experiments are over once the gas drives out the clay from the conduit. The main goal of this project is to achieve a better understanding of the clay flow through a conduit driven by a pressure gradient and the buoyancy force associated with a gas flux through the clay. For this reason the discussion of the vertical pipe results will focus on clays with $S \leq 0.08$.

The top of the conduit was recorded by a camera during each experiment in order to visualise the bubble bursting. By counting the number of gas eruptions through the whole duration of the experiment it was possible to measure the average frequency of the gas eruptions $f$. Figure 3.14a shows the variation of the frequency $f$ with the gas flow injected $Q_g$ for three experimental series with different initial pressure $\Delta P_0$. All the frequency data are used to produce an average frequency curve specific for each clay-water mixture (Figure 3.14b) in order to compare the effect of the clay consistency ($S$) on the bursting frequency. The data in figure 3.14a show that the frequency $f$ of the gas bubbles bursting at the top of the conduit is not significantly affected by the overpressure $\Delta P_0$. The frequency $f$ increases with the gas flow rate $Q_g$ before reaching a maximum when $0.5 \leq Q_g \leq 2$ cm$^3$/s. Increasing the gas flow rate beyond

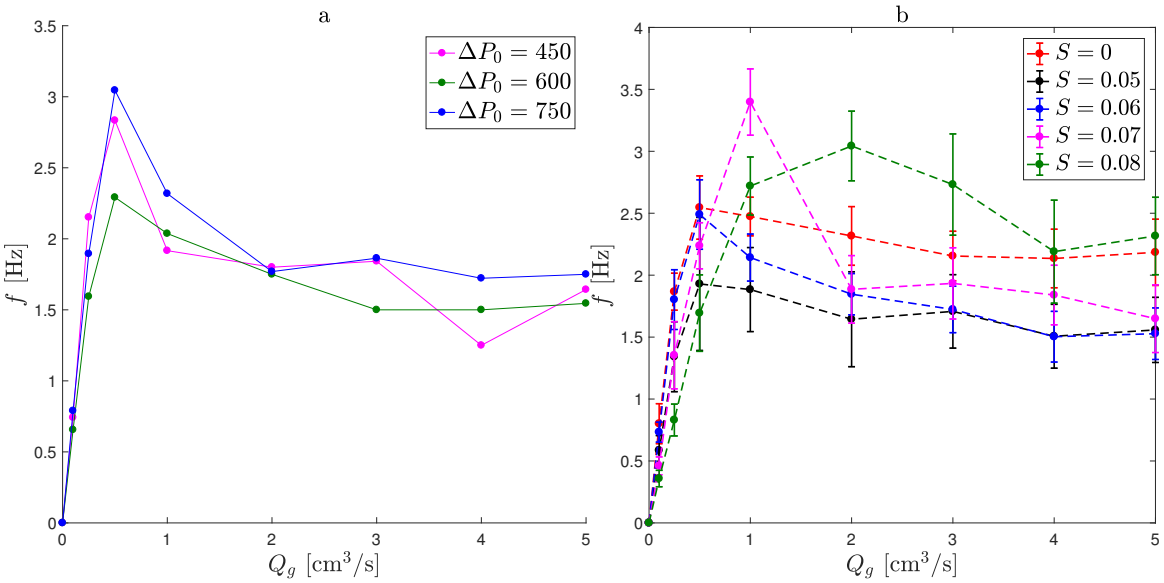


Fig. 3.14 (a) Plot of the average frequency of the gas bubbles bursting at the top of the conduit ($f$) as a function of the gas flow rate $Q_g$ for different values of the initial over-pressure $\Delta P_0$ and $S = 0.06$. (b) Mean value of the average frequency $f$ as a function of the gas flow rate ($Q_g$) for different water content mixtures ($S$).

the maximum value of $f$ shows a gradual decrease and reaches a plateau of about $f = 2 \pm 0.5$ Hz for flow rates higher than 4 cm$^3$/s.

### Under-pressured gas regime

During the under-pressure experiment the volume of the conduit is partially filled with clay and the distance between the top height of the clay in the conduit and the top of the conduit is defined as $\Delta H_c$ (Figure 3.1b). The description of this set of experiments considers the under-pressure $\Delta P^-$ in the conduit as given by $\Delta P^- = -\rho_c g|\Delta H_c|$ (Figure 3.15a). The experiment is started by injecting gas at the base of the conduit into the stagnant clay while the reservoir pressure is held at a constant value $\Delta P_0$. The gas injected rises through the clay in buoyant bubbles and the gas is released into the atmosphere once these bubbles burst at the top of the mud column. The total volume of the gas flowing through the clay lifts the mud column by a length $\Delta H_g$ (Figure 3.15b) and in some cases causes a mud outflow.

The quantity of mud erupted in this experimental regime is small and the variation in the reservoir pressure is negligible (lower than 30 Pa). A systematic series of experiments was run to explore the influence of the clay content of the clay-water mixture ($0 \leq S \leq 0.08$), and also the gas injection flow rates ($0.1 \leq Q_g \leq 5$ cm$^3$/s)

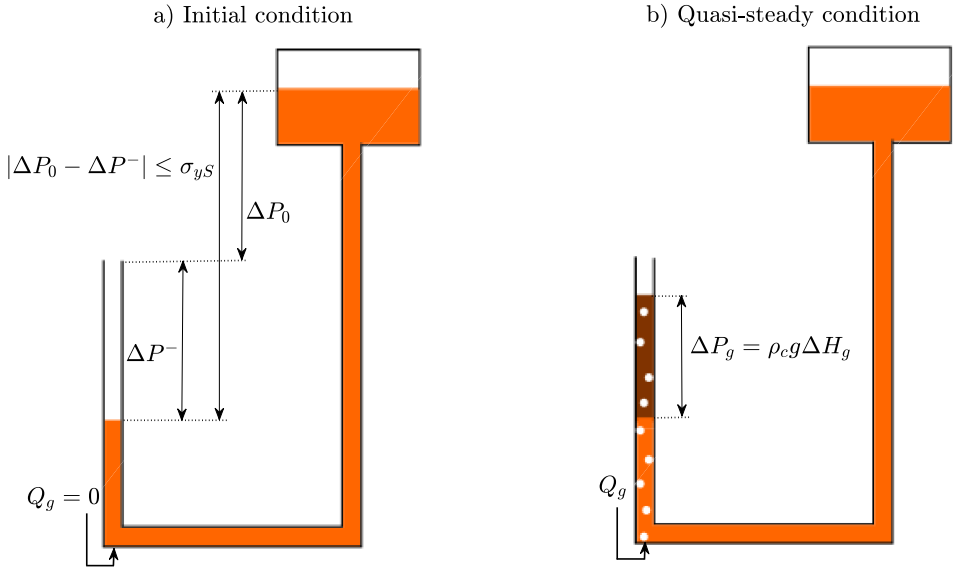


Fig. 3.15 (a) Schematic of the initial condition of the under-pressured gas-injection driven mud eruption. (b) Schematic of the under-pressured gas injection experiment in which the gas injection causes the mud height in the conduit to rise.

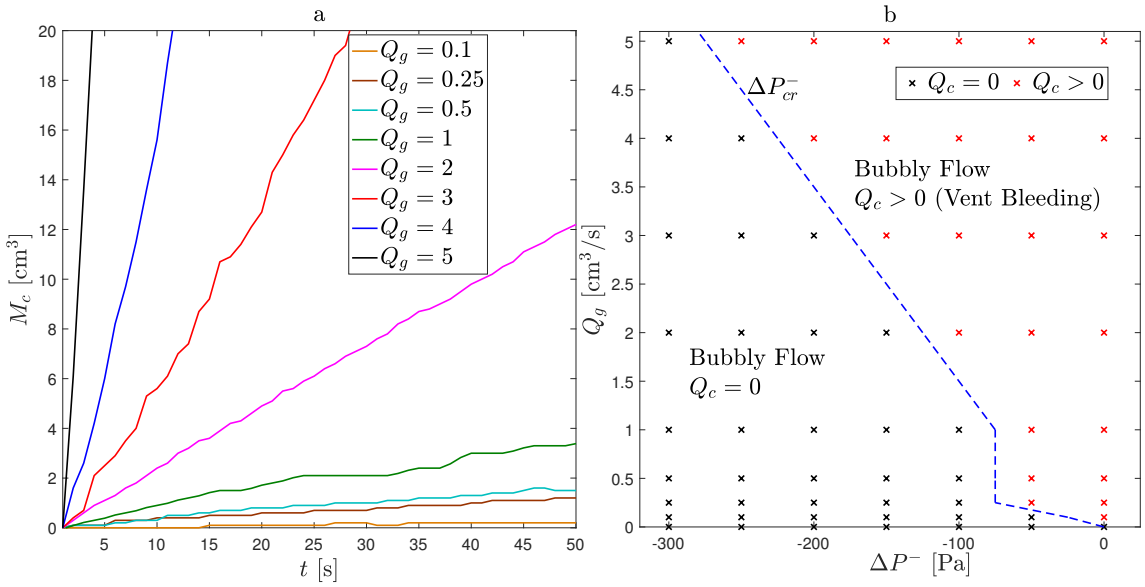


Fig. 3.16 (a) Plot of the mass erupted ($M_c$) from the conduit over time ($t$) during an under-pressured gas experiment with different gas flow rate ($Q_g$) injected in the conduit and $S = 0.05$. (b) Schematic of the under-pressure mud eruption highlighting the eruptive case ($Q_c > 0$, red crosses), the non-eruptive case ($Q_c = 0$, black crosses) and the boundary between these two cases given by $\Delta P^-_{cr}$ (blue dashed line) for $S = 0.06$.

and the different values of $\Delta H_c$ ($-5 \leq \Delta H_c \leq 0$ cm, table 3.2). It is important to remember that the yield stress clogs the clay in the tube connecting the reservoir to the vertical pipe which allows the clay in the reservoir to be maintained at a different height from the clay in the conduit (Figure 3.15a). In order to keep the clay clogged the pressure difference between the reservoir and the conduit has to be smaller than the static yield stress hence:

$$\mid \Delta P_0 - \Delta P^- \mid \leq \sigma_{yS} \tag{3.2}$$

The height difference between the reservoir and the clay level in the conduit, during experiments with a relatively high water content mixture ($S \leq 0.05$), is smaller that the size of the measurement errors (0.5 cm) and suggesting a negligible static yield stress (lower than 50 Pa). The gas injection in the liquid-like clay column lifts the clay level and causes an eruption in some cases. Figure 3.16a shows a plot of the mass erupted ($M_c$) during the eruptions caused by various gas injection rates for $S = 0.05$ and $\Delta P^- = -50$ Pa. The outflow is consistent over time and the eruption duration is limited by the capacity of the gas injection system. Increasing the bentonite concentration of the mixture clogs the experimental apparatus and the flow from the reservoir is stopped. Hence, when $0.06 \leq S \leq 0.08$, the eruptions caused by the gas injection last only a few seconds because the gas flow bleeds the conduit of a certain volume of clay but the reservoir does not refill the conduit of the erupted volume. Although there is little information about the flow rate during the eruption the data allow us to identify an eruption regime. The systematic set of experiments distinguish the eruptive experiments ($Q_c > 0$, red crosses in figure 3.16b) from the non-eruptive experiments ($Q_c = 0$, black crosses figure 3.16b) depending on the conduit under-pressure ($\Delta P^-$) and the gas flow ($Q_g$) through the conduit for different clay-water mixture. From this result it is then possible to define a critical pressure $P_{cr}^-$ (blue dashed line in figure 3.16b) acting as a boundary between the two regimes.

### 3.5.2 Interpretation of the experiments

We now analyse the flow of pure clay driven by a pressure gradient and then the effect of the fluctuations of the yield stress and its complex behaviour. The discussion finally investigates the effects of gas flow on such flow.

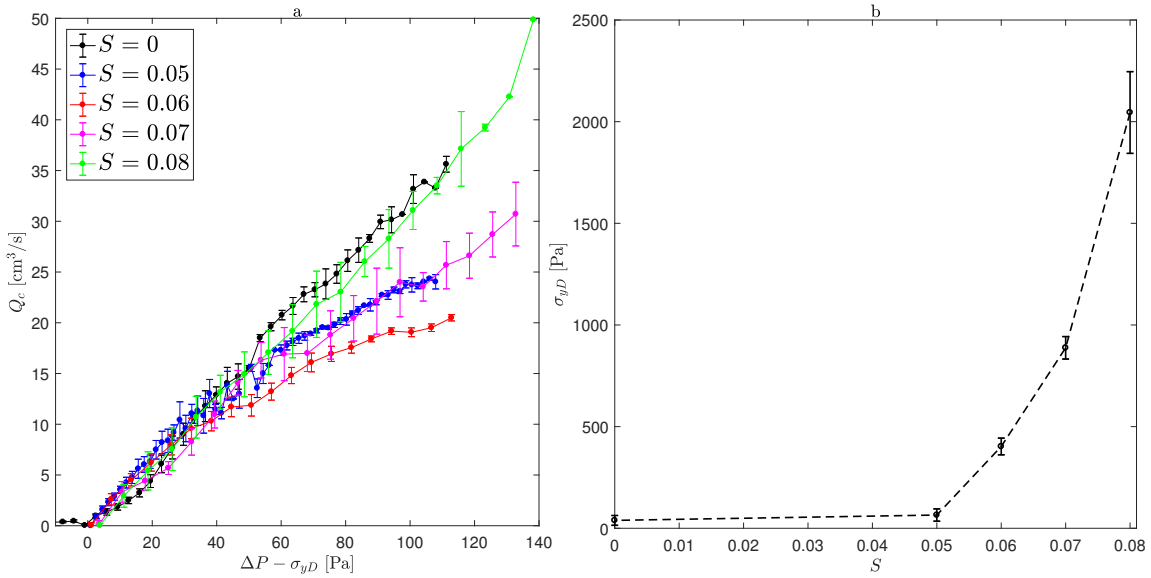


Fig. 3.17 (a) Plot of the average clay outflow $Q_c$ as a function of the difference between the reservoir pressure $\Delta P$ and the dynamic yield stress $\sigma_{yD}$ for different mixtures of clay ($S$). (b) Plot of the dynamic yield stress, measured for each experiment, as a function of the bentonite mass content in the clay-water mixture ($S$).

### Clay flow interpretation

Figure 3.17a shows the average data obtained from the over-pressured experiments comparing the outflow of clay ($Q_c$) with the reservoir pressure $\Delta P$ normalised by the dynamic yield stress for various clay-water mixture concentrations ($S$). The plot suggests a linear relationship between the clay flow rate $Q_c$, and the reduced reservoir pressure $\Delta P_T$, defined as the difference between the reservoir pressure and the dynamic yield stress $\Delta P_T = \Delta P - \sigma_{yD}$ (Figure 3.17a). This result is consistent with the flow of a Newtonian fluid through a narrow pipe as given by Haghen-Poiseuille equation

$$\Delta P_T = 8\mu L Q_c/(\pi R^4) \tag{3.3}$$

where $L$ is the tubing length, $R$ is the inner radius and $\mu$ is the dynamic viscosity of the fluid. Considering $L = 2.8$ m and $R = 1$ cm it results that the overall clay viscosity is $\mu = 5.2 \pm 0.6 \times 10^{-3}$ Pa s. The dynamic yield stress, given by the experimental pressure $\Delta P$ at which the eruptive flow stops, increases exponentially with the clay-water mixture concentration $S$ (Figure 3.17b) from 50 Pa for $S = 0.05$ to $2 \times 10^3$ Pa with $S = 0.08$. In our experiments the values $\sigma_{yS}$ and $\sigma_{yD}$ depend on the specific clay-water mixture and may vary during an experiment owing to dynamic changes in the clay.

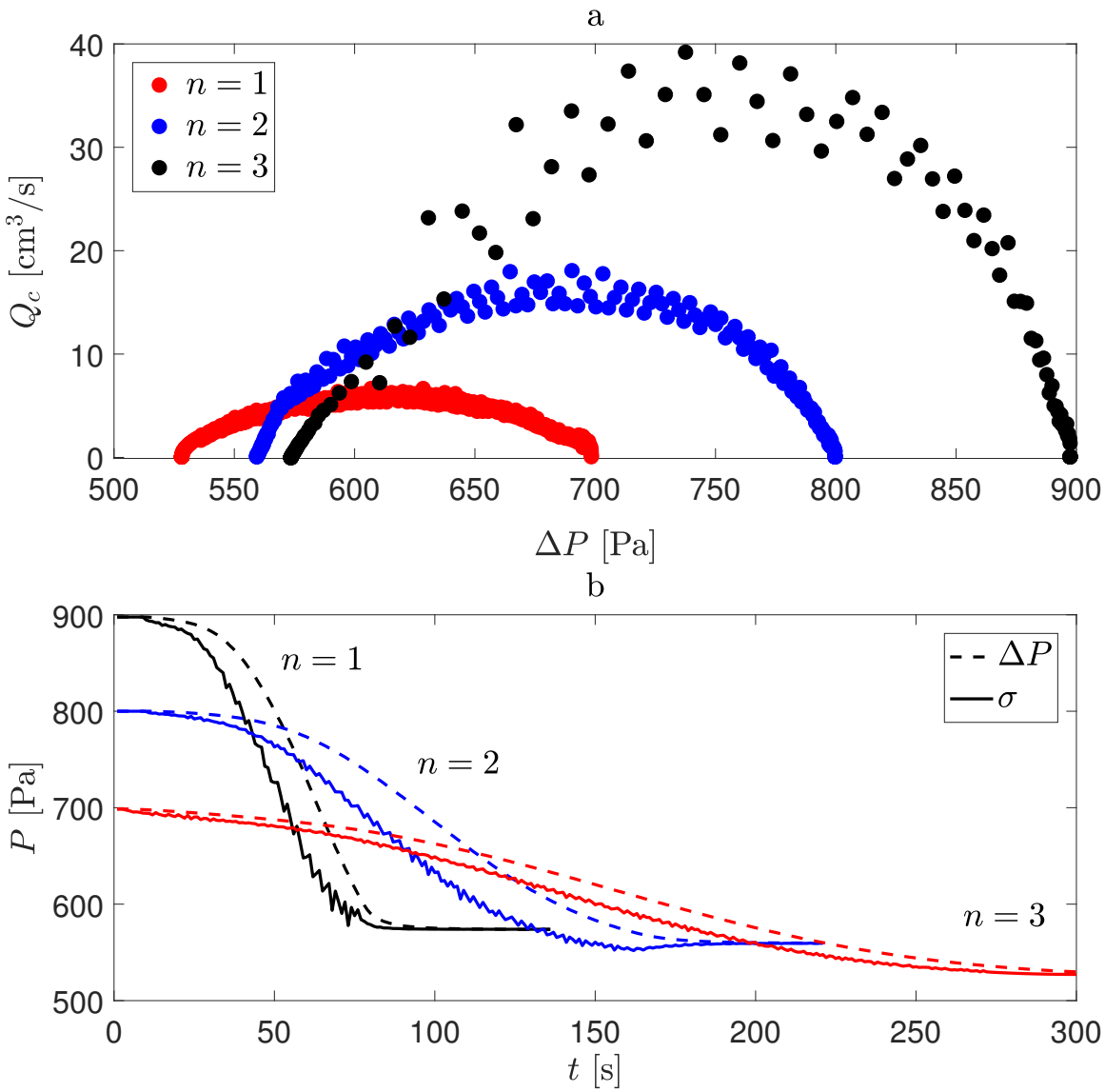


Fig. 3.18 (a) Plot of the mud flow rate erupted as a function of the reservoir pressure during a cyclic eruption (where $n$ is the number of the eruption during the cycle) obtained by gradually increasing the reservoir pressure as shown in figure 3.10 ($S = 0.06$ and $Q_g = 0$).(b) Plot of the yield stress measured during each eruption according to equation3.4.

The experiments reproducing a cyclic eruption suggest that the eruption starts once the total pressure is higher than the static yield stress and stops when it is lower than the dynamic yield stress. Gradually increasing the reservoir pressure may cause cyclic eruptions as shown in figure 3.10. Figure 3.18a shows the flow rate of clay ($Q_c$) during three cyclic eruptions in succession, where $n$ is the cycle number, with the reservoir pressure $\Delta P$. Once the eruption is started, during each cycle, the clay flow increases before reaching a maximum value and then reduces with the pressure as shown in figure 3.18a. The variation of $Q_c$ is possibly caused by a variation over time of the yield stress caused by the stress $\Delta P$. Supposing that the eruption flow rate instantly adjusts to the pressure gradient $\Delta P - \sigma_y$, then using equation 3.3 it is possible to obtain the gradual decrease of the yield stress from $\sigma_{yS}$ to $\sigma_{yD}$ for each eruption given by

$$\sigma_y = \Delta P - 8\mu L Q_c/(\pi R^4) \tag{3.4}$$

Figure 3.18b is a plot of the yield stress during the $n$th eruption of the cycle. The gradual reduction of the static yield stress after each eruption suggests that the clay strengthens after the clay flow stops but, because of the relatively fast pressurisation of the reservoir, the eruption is started before the clay has completely healed.

### Gas-clay flow results

As discussed in the over-pressured gas regime (§3.5.1), the gas flow added to the eruption increases the clay outflow $Q_c$ during the eruption. Supposing that $Q_c$ proportionally increases with $\Delta P$, as suggested by the experimental results, it is possible to predict the dynamic yield stress for all the experiments as the value of $\Delta P$ for which $Q_c = 0$. Figure 3.19b shows the variation of the yield stress with the gas-flow rate ($Q_g$) measured for one clay-water mixture. Consequently the dynamic yield stress seems to reduce with $Q_g$, but the overall behaviour $Q_c \propto \Delta P_T$ seems to be similar with and without the gas flow added to the clay (Figure 3.19a). The gas injection on the clay flow will be discussed in terms of an extra pressure $\Delta P_g$ given by:

$$\Delta P_g = \rho g H_0 \phi \tag{3.5}$$

where $\phi$ is the volume ratio of the gas in the clay. Supposing that the yield stress reduction for $Q_g > 0$ is equal to this pressure term then I predict that

$$\sigma_{yD}(Q_g) = \sigma_{yD}(Q_g = 0) - \Delta P_g(Q_g) \tag{3.6}$$

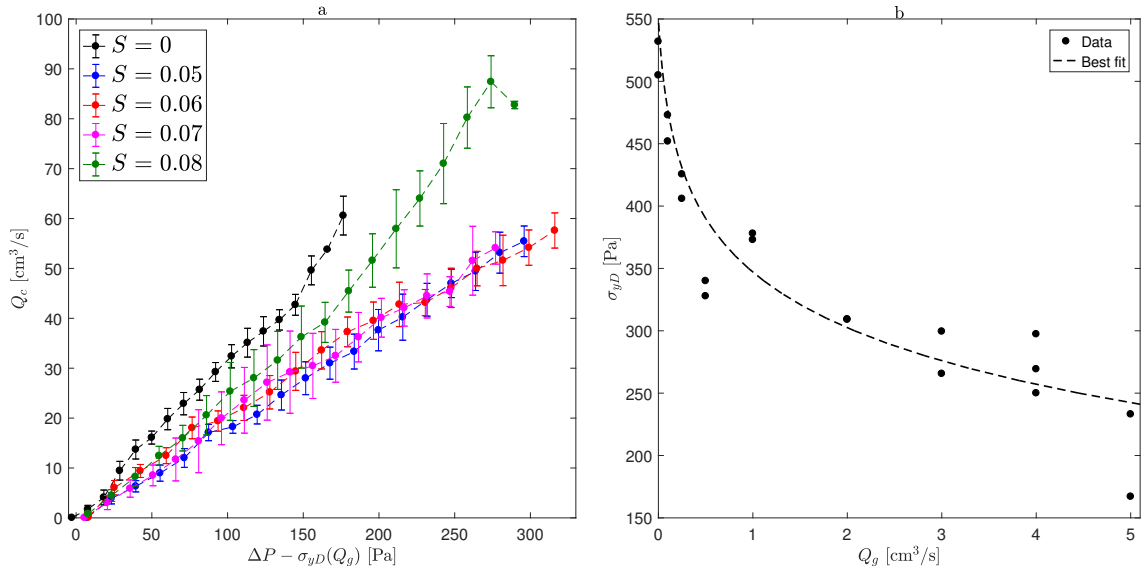


Fig. 3.19 (a) Results from the over-pressured and gas driven mud eruption regime showing the dependence of the clay flow rate $Q_c$ on the overpressure $\Delta P_T$ for $0 \leq S \leq 0.08$ and for gas flow rates in the range $0 \leq Q_c \leq 5$ [cm$^3$/s]. (b) Graph showing the variation of the dynamic yield stress with the gas flow rate $Q_g$ for $S = 0.06$.

Given the data for $\sigma_{yD}(Q_g)$ and equation 3.5, it is possible to define an experimental value of the volume fraction $\phi_1$, given by:

$$\phi_1 = (\sigma_{yD}(Q_g = 0) - \sigma_{yD}(Q_g))/(\rho_c g H_0) \tag{3.7}$$

The volume ratio tends to increase with the gas flow rate $Q_g$ but the fluctuations of the dynamic yield stress for $S > 0.06$ (Figure 3.20a) do not allow an accurate measurement of the gas volume ratio.

In the case that the clay is stagnant in the conduit (as in the under-pressured gas regime), the gas flow lifts the mud column by a length $\Delta H_g$ (Figure 3.15b). The gas flow is sufficient to cause an eruption when it lifts the clay level beyond the conduit height ($\Delta H_g > \Delta H_c$). Supposing the flow is steady state and both fluids are incompressible it follows that the volume increase of the clay ($\Delta V = \Delta H_g \pi R^2$) is equal to the volume of the gas bubbles flowing in the clay. $\Delta H_g$ is then given by solving the following equation

$$\Delta H_g = \phi_2(H_0 - \Delta H_c + \Delta H_g) \tag{3.8}$$

A similar discussion in terms of pressure suggests that the extra-pressure associated with the gas $\Delta P_g = \rho_c g \Delta H_g$ causes an eruption when it is greater than the under-pressure $\Delta P^-$. The eruption condition, according to equation 3.8 is then given by

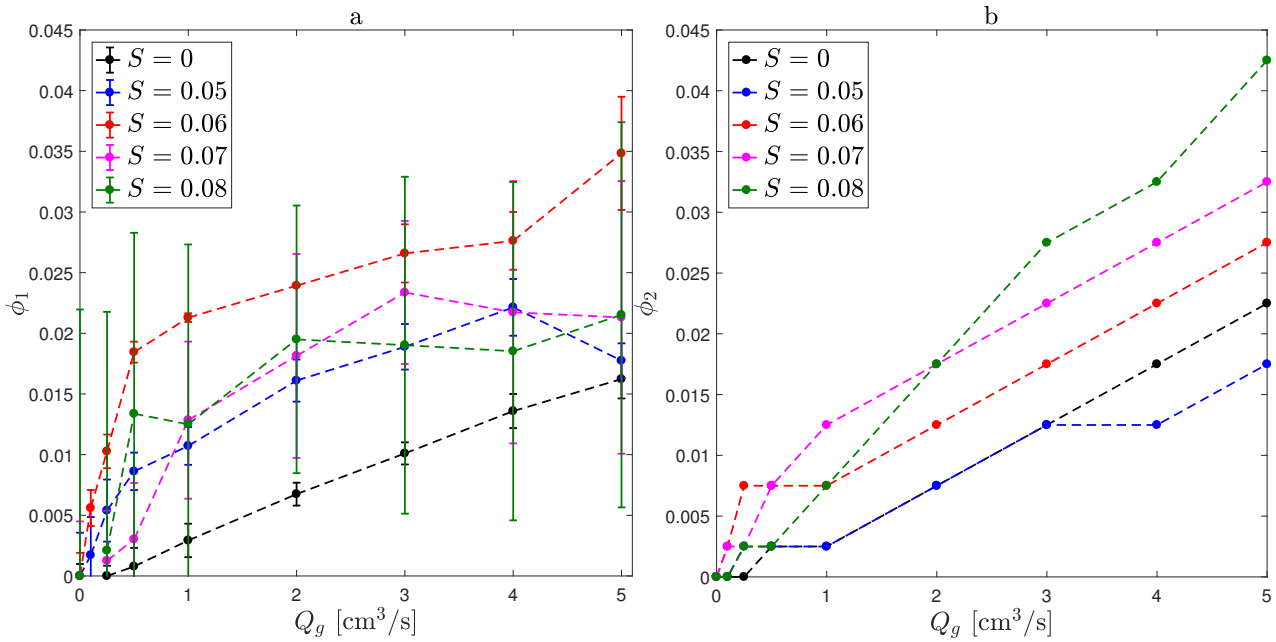


Fig. 3.20 (a) Plot of the gas volume ratio $\phi_1$, given by equation 3.7, compared to the gas injection flow rate $Q_g$ for various bentonite concentrations in the clay-water mixture $S$. (b) Plot of the gas volume fraction $\phi_2$ as a function of the gas volume flow-rate ($Q_g$)injected for $0 \leq S \leq 0.08$ given by equation 3.9 where $\Delta P^- = \Delta P^-_{cr}$.

$$\Delta P^- \geq -\rho_c g H_0 \phi_2 \tag{3.9}$$

The experimental results from the under-pressured regime provide a measurement of the critical under-pressure ($\Delta P^-_{cr}$, figure 3.16b) defined as:

$$\begin{cases} \Delta P^- > \Delta P^-_{cr} \Rightarrow Q_c > 0 \\ \Delta P^- < \Delta P^-_{cr} \Rightarrow Q_c = 0 \end{cases}$$

which, according to equation 3.9, allow measurement of the gas volume ratio with an under-pressured reservoir as given by $\phi_2 = -\Delta P^-_{cr}/\rho_c g H_0$. The volume ratio measured in the under-pressured case (Figure 3.20b) has been defined as $\phi_2$ in order to be distinguished from the volume ratio measured during the over-pressured gas case (equation3.7). As shown in figure 3.20b the volume fraction increases with the thickness of the clay and linearly increases with the gas flow rate. Both terms $\phi_1$ and $\phi_2$ are similar and they increase linearly with the flow rate but the fluctuation in $\phi_1$ due to the dynamic yield stress fluctuations do not allow a comparison for $S \geq 0.07$.

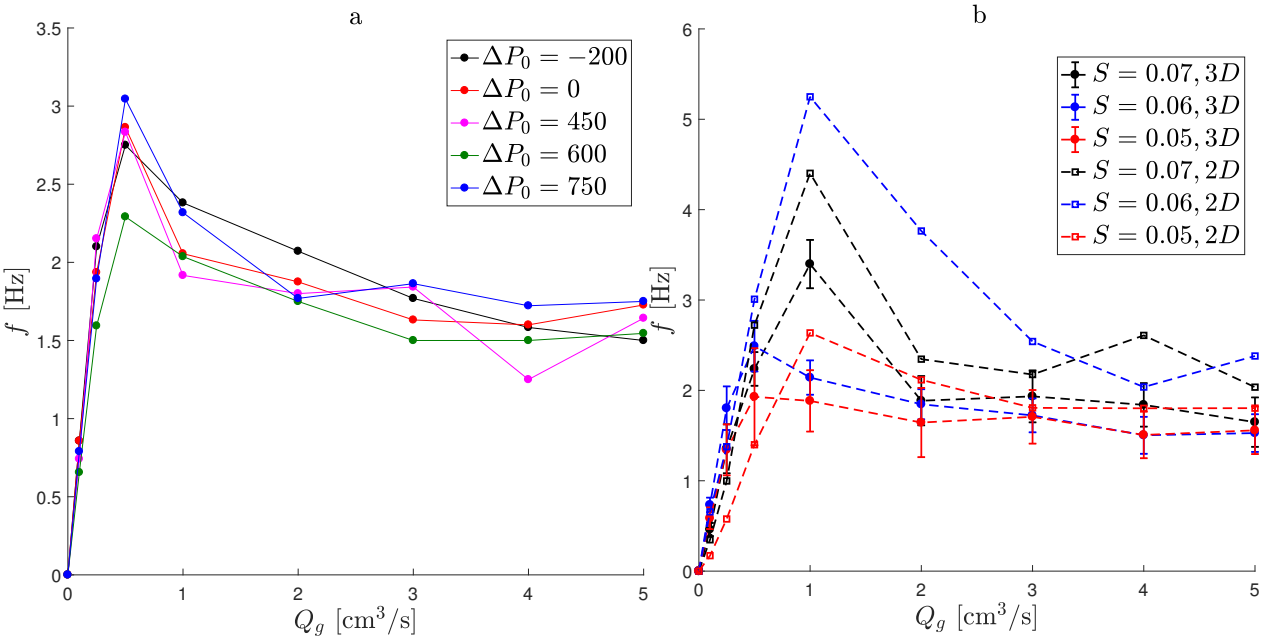


Fig. 3.21 (a) Plot of the average frequency ($f$) of the eruption of gas bubbles at the surface as a function of the gas injection rate ($Q_g$) comparing experiments with under-pressured reservoirs ($\Delta P_0 \leq 0$) and over-pressured reservoirs ($\Delta P_0 > 0$) for $S = 0.06$. (b) Plot of the average frequency of gas bursting events ($f$) as a function of the gas injection flow rate ($Q_g$) comparing the results for a vertical conduit ($3D$) with the results for a Hele-Shaw cell ($2D$).

Figure 3.21 shows the frequency ($f$) of the gas burst at the top of the conduit for different values of the reservoir pressure ($\Delta P_0$), allowing a comparison between the under-pressured case ($\Delta P_0 \leq 0$) and the over-pressured regime ($\Delta P_0 > 0$). The comparison demonstrates that the frequency of the bubble burst is not significantly affected by the reservoir pressure. The non correlation between $\Delta P_0$ and $f$ suggests that the gas rise speed is considerably higher than the clay rise speed. The strong similarity of the bubble bursting frequency ($f$) between the two-dimensional experiments and the axis-symmetric experiments (Figure 3.21b) also suggests the gas flow arranges the rising bubble train in a similar path as described in §3.4.3.

Supposing bubbles are rising through the vertical pipe as a bubble train, as shown for the two-dimensional experiments, with a diameter as wide as the conduit, it follows that:

$$\begin{cases} Q_g = \pi R_0^2 L_b f \\ \phi = L_b / L_c \\ W = L_c f \end{cases} \tag{3.10}$$

where $L_b$ is the length of the gas bubbles, $L_c$ the distance between consecutive bubbles and $W$ is the rising speed of bubbles. The rising speed of bubble slugs for a Newtonian fluid is given by former literature (Pioli et al. [59]) as $W = m\sqrt{2gR_0}$. From the values of $\phi$, measured from both the under-pressured and the over-pressured gas regime, it was found that $m = 0.24 \pm 0.08$ and $W = 18 \pm 5$ cm/s. This result for $m$ is consistent with the results in Pioli et al. [59] and confirms the hypothesis that $W$ is significantly higher than the clay flow speed $W_c$ ($W_c \leq 3$ cm/s). Under this condition it is then possible to neglect the effect of the clay outflow on the gas volume ratio.

## 3.6 Discussion

The results identify separate regimes describing the eruption of mud volcanoes considering the effects of reservoir pressure, gas flow and the yielding property of the material. I now build a numerical model for the eruption considering the compressibility of the gas flowing through the conduit.

### 3.6.1 Eruptive regimes

Consider a generic case of a mud volcano as shown in figure 3.22a, where the pressure in the reservoir is given by $\Delta P$ and the gas generated from a deeper source (either a

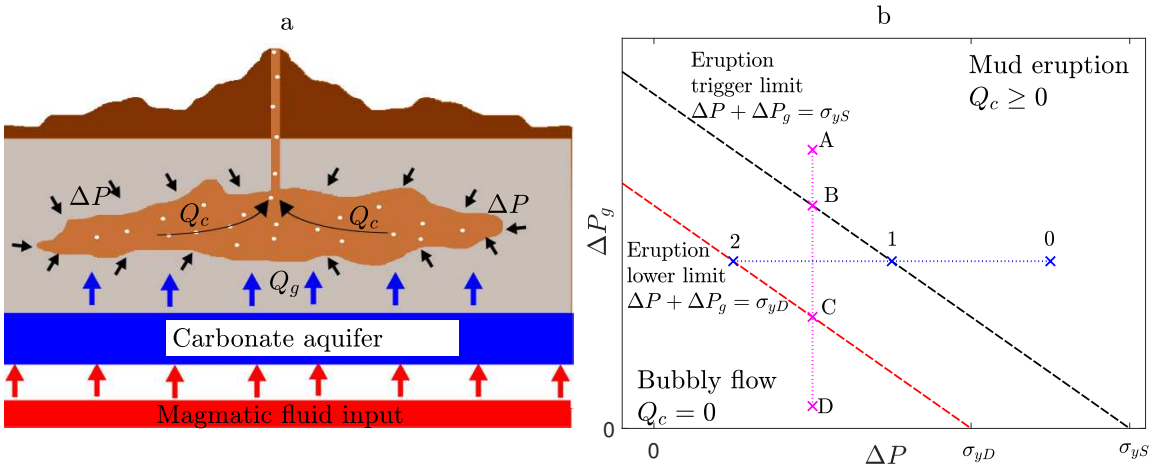


Fig. 3.22 (a) Schematic of the mud volcano Lusi (Indonesia) as described in the literature (Shirzaei et al. [73]). The pressure of the reservoir is given by the weight of the geological strata surrounding the mud reservoir while the gas is supplied to the reservoir from a deeper source. (b) Schematic of the different mud eruption regimes as a function of the pressure in the reservoir $\Delta P$ and the dynamic pressure associated with the gas flow $\Delta P_g$. In the under-pressured case ($\Delta P + \Delta P_g \leq \sigma_{yS}$) there is no clay outflow and the flow consists of a generic bubbly flow of gas through the conduit.In the over-pressured case ($\Delta P + \Delta P_g \geq \sigma_{yS}$, black dashed line) the mud eruption is continuous and the clay outflow is sustained until the total pressure decreases to the dynamic yield stress $\sigma_{yD}$ (red dashed line).

biogenetic gas, a deeper aquifer or a natural gas reservoir) flows through the reservoir and into the conduit with a flow rate $Q_g$. The mud outflow is affected by the sum of the reservoir pressure $\Delta P$ and the gas buoyancy derived pressure $\Delta P_g$ and it is possible to define two pressure domains which affect the resulting mud-volcano activity (figure 3.22b).

The necessary condition for an overpressure driven eruption is given by $\Delta P + \Delta P_g - \sigma_{yS} > 0$ (Eruption trigger limit, black dashed line in figure 3.22b). The resulting eruption (mud eruption regime in figure 3.22b) is continuous and the volumetric clay outflow (according to equation 3.3,3.5 and 3.6) is given by

$$Q_c = \frac{\pi R^4}{8\mu L} \left(\Delta P + \rho_c g H_0 \phi - \sigma_{yD}\right) \tag{3.11}$$

The eruption persists until the pressure resulting from the addition of the reservoir and the extra gas pressure is higher than the dynamic yield stress (Eruption lower limit, red dashed line in figure 3.22b). In case of $\Delta P + \Delta P_g \leq \sigma_{yS}$ the sum of the reservoir pressure and the gas pressure is not high enough to cause any outflow and the mud volcano is dormant even though gas still issues from the top of the conduit (Bubbly flow regime in figure 3.22b).

Figure 3.22b shows two possible evolutions of an eruption of a mud volcano (dotted blue and magenta lines) both starting from a high overpressure initial condition (points A and 0 in figure 3.22b). In the first case (purple vertical line) the pressure of the reservoir ($\Delta P$) is supposed constant during the eruption while the gas flow rate reduces. In this case the initial high pressure (point A) causes an eruption which allows the gas to escape from the reservoir. Supposing that the outflow of gas escaping the reservoir is higher than the inflow from deeper sources the gas pressure term ($\Delta P_g$) will gradually reduce. The mud outflow stops once the total pressure is below the dynamic yield limit $\sigma_{yD}$ (point C) but the gas may continue flowing in the conduit. This will cause a further reduction of the gas pressure. In this case gas bubbles burst at the top of the conduit and the gas pressure ($\Delta P_g$) continues to decrease as the gas flows through the conduit until reaching a steady state condition (point D). This type of eruption is representative of low gas flow rates penetrating the reservoir or large mud reservoirs so that the eruption of mud does not have a significant impact on the reservoir pressure. In the second case (blue horizontal line) the buoyancy derived pressure associated with the gas is supposed constant while the reservoir pressure reduces due to the mud driven from the reservoir during the eruption. Starting with the initial condition (point 0), the eruption causes a gradual reduction in the reservoir pressure while the gas flow remains constant until reaching the limit given by the dynamic yield stress (point

2). Subsequently, mud is not erupted and the reservoir pressure remains constant while bubbles of gas burst from the conduit without eruption of clay. In order to start a second eruption the pressure has to increase above the static yield limit for both eruption styles (point B and 1). The second type of eruption is representative of volcanoes with relatively small reservoirs or large gas inflow. In general, I envisage that eruptions involve a combination of these two eruption styles.

The historical recordings of mud eruptions (Mazzini et al. [50]) show an almost continuous outflow ($0.2 \leq Q_c \leq 2$ m$^3$/s) between the 27th of May and the 26th of September 2006 with random eruptions with similar $Q_c$ after that period. The description of the eruptions following the 26th of September described in Vanderkluysen et al. [80] ,with intermittent eruptions, may be similar to the intermittent eruptions we have found in the present experiments, and this suggests that gas may leak from the conduit with an under-pressured mud reservoir. It would be interesting to explore the role of earthquakes and environmental conditions which may also influence the results.

### 3.6.2 Numerical model

The extra-pressure given by the gas flow has been obtained by supposing that both the gas and the clay are incompressible fluids but in case of high pressure, such as mud volcano reservoirs, the compressibility of the gas must be considered. The fluid flow through a thin and long pipe assuming steady-state, incompressible and axis-symmetric flow is given by the balance between the inertia, the viscous drag and the pressure gradient and external forces on the flow (Oliemans et al. [55]). This leads to the relation

$$\frac{\partial P}{\partial z} - \bar{\rho} g = 8\mu \frac{W_c}{R^2} + c_D \rho_c \frac{{W_c}^2}{R^2} \tag{3.12}$$

where $c_D$ is the inertial drag coefficient, $W_c$ is the vertical speed of the clay in the conduit and $\bar{\rho}$ is the bulk density which is given by $\bar{\rho} = \rho_c(1-\phi) + \rho_g \phi$. The subscripts $c$ and $g$ are used to define clay or gas properties respectively.

According to the conservation of mass and the ideal gas law it follows that (Beggs and Brill [5]):

$$\begin{cases} W_c = Q_c / [\pi R^2 (1-\phi)] \\ \dot{M}_g = \phi \pi R^2 \rho_g \left(W_c + W_g\right) \\ \rho_g = \frac{P}{P_a} \rho_{g,a} \end{cases} \tag{3.13}$$

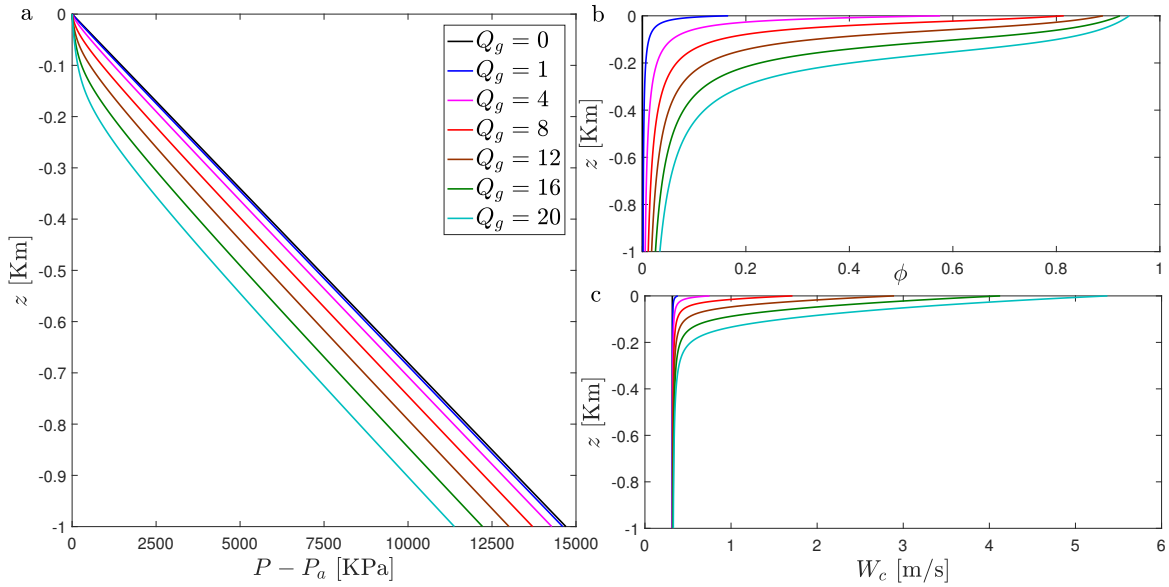


Fig. 3.23 (a) Plot of the fluid pressure as a function of the height in a vertical conduit for various gas flow rates given by equation 3.14. (b) Plot of the gas volume ratio $\phi$ as a function of the height of the vertical conduit for various gas flow rates obtained by numerically solving equations 3.14. (c) Plot of the speed of the clay $W_c$ as a function of the height in a vertical conduit for various gas flow rates obtained by numerical solution of equations 3.13. The data presented in both plots have been obtained for the case $R = 1$ m, $\mu = 10^{-2}$ Pa s, $\rho_{g,a} = 1$ kg/m$^3$, $\rho_c = 1500$ kg/m$^3$, $P_a = 101.3$ kPa, $Q_c = 1$ m$^3$/s and in which the length of the conduit is assumed to be $H_0 = 1$ km. If $\phi$ increases above values of 0.5-0.7, the flow regime may evolve from the slug regime to a high gas annular flow regime. At Lusi the system remains in the low gas regime, consistent with $Q_g \leq 2$ m$^3$/s in this plot.

where $Q_c$ is the volume eruption rate of clay, $\dot{M}_g$ is the mass flow rate of gas, $W_g$ is the speed of the gas relative to the clay, $P_a$ is the atmospheric pressure and $\rho_{g,a}$ is the density of gas at atmospheric pressure. We assume that the rise speed of gas bubbles ($W_g$) relative to the clay, is given by $W_g = m\sqrt{2Rg}$ (equation 13 in Pioli et al. [59]), where $m$ is a constant in the range $0.2 \leq m \leq 0.4$, for inertial flow of gas bubbles through the clay (as described in §3.4.1). It then follows from equations 3.12 and 3.13:

$$\begin{cases} \frac{\partial P}{\partial z} = A(1-\phi)^{-1} + B(1-\phi) + C\phi P + D(1-\phi)^{-2} \\ EP\phi^2 - (EP + Q_g + PQ_c/P_a)\,\phi + Q_g = 0 \end{cases} \tag{3.14}$$

where $A$,$B$, $C$, $D$ and $E$ are constant values given by

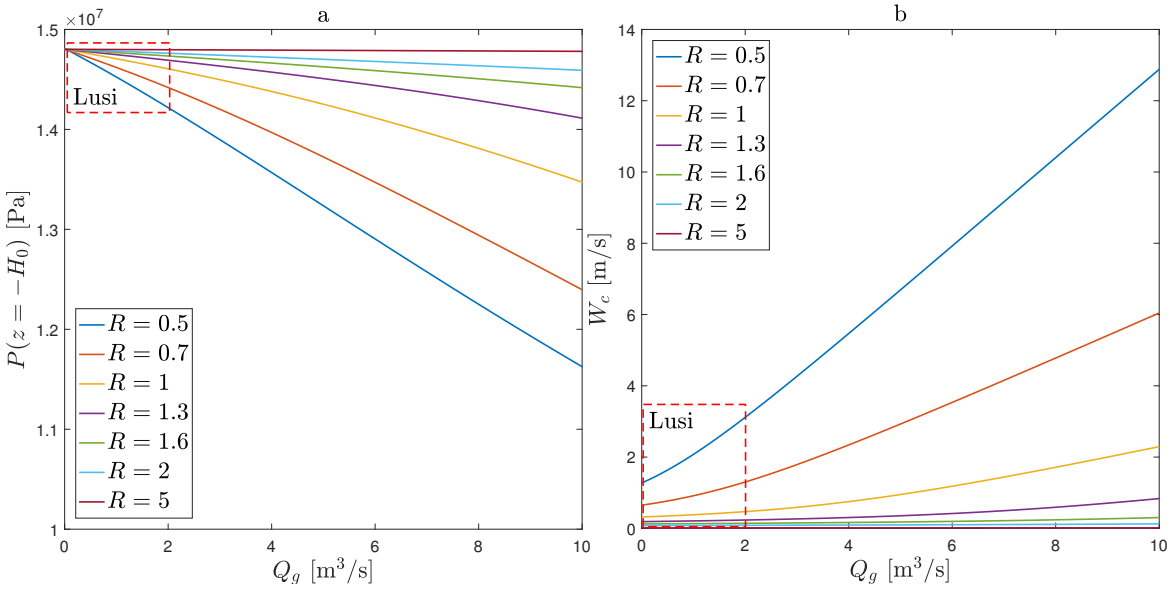


Fig. 3.24 (a) Plot of the reservoir pressure ($z = -H_0$) as a function of the gas flow rate $Q_g$ for various radii of the conduit $R$. (b) Plot of the vertical speed of the gas-clay mixture at the top of the conduit ($z = 0$) as a function of the gas flow rate $Q_g$ for various values of $R$. Both plots have been obtained by numerical solution of equation 3.14 and imposing that $P(z = 0) = P_a$, the atmospheric pressure. The other variables are the same as given in the caption of figure 3.23. The red dashed perimeter in both figures includes values of the reservoir pressure $P(z = -H_0)$ and flow speed ($W_c(z = 0)$) for gas flow rates in the range $0.2 \leq Q_g \leq 2$ (as measured from Lusi eruptions).

| $H_0$ (m) | $R$ (m) | $\mu$ (Pa s) | $\rho_{g,a}$ (Kg/m$^3$) | $\rho_c$ (Kg/m$^3$) | $P_a$ (KPa) | $Q_c$ (m$^3$/s) | $Q_g$ (m$^3$/s) |
|---|---|---|---|---|---|---|---|
| $500-2000$ | 1.5 | $10^{-2}$ | 1 | 1500 | 101.3 | 0.2-2 | 0.2-2 |

Table 3.3 Table of values of the Lusi mud volcano (Shirzaei et al. [73], Vanderkluysen et al. [80] and Mazzini et al. [50])

$$\begin{cases} A = -8\mu Q_c/(\pi R^4) \\ B = -g\rho_c \\ C = -g\rho_{g,a}/P_a \\ D = -c_D Q_c^2 \rho_c/\left(2\pi^3 R^5\right) \\ E = \pi R^2 m\sqrt{2Rg}/P_a \end{cases} \tag{3.15}$$

and $Q_g$ is the gas volume flow rate from the conduit ($Q_g = \dot{M}_g/\rho_{g,a}$). Solving the system numerically allows a prediction of the pressure in the conduit given its geometry as shown in figure 3.23. The values for the constants defined in equation 3.15 were obtained using data from the Lusi mud volcano eruptions in Indonesia (Table 3.3). The assumption of a constant rise speed for the gas is accurate as long as the volume ratio $\phi$ is small. For $\phi \to 1$ the gas flow through the conduit may evolve from a series of rising slugs/bubbles into a high speed, continuous gas flow through a narrow conduit, which forms a fountain at the surface. Supposing the pressure at the top of the conduit is equal to the atmospheric pressure, it is possible to measure the reservoir pressure $P(z = -H_0)$ (Figure 3.24a), where $H_0 = 1$ km, and the gas volume ratio at the top of the conduit $\phi(z = 0)$ (Figure 3.24b) according to the gas flow rate erupted from the conduit. According to this model the extra-pressure $\Delta P_g$, given by the Lusi mud eruptions (Table 3.3) and supposing $5 \leq Q_g \leq 10$ m$^3$/s, is approximately $0.5 \leq \Delta P_g \leq 1.5 \times 10^6$ Pa.

## 3.7 Conclusions

A series of experiments were carried out in order to study the flow of mud through a vertical conduit caused by the joint effect of a high pressure reservoir and gas flow. From this experimental work we found that the pressure difference between the reservoir and the atmosphere has to overcome the yield stress in order to cause the eruption. When pressure is higher than the yield limit the mud outflow is proportional to the

pressure gradient, the yield stress reduces and the eruption is sustained until the reservoir pressure is lower than the yield stress. While the conduit is inactive the yield stress increases and the reservoir has to rebuild the pressure to cause a second eruption and the fluctuations in the difference between yield stress and reservoir pressure cause cyclic eruptions. The gas flow affects the flow of clay along the conduit as a result of the buoyancy force according to equation 3.14. When the reservoir is over-pressured this extra gas pressure adds to the reservoir pressure increasing the mud flow-rate while in under-pressured conditions it may cause an out-flow of clay; however the eruption rate varies intermittently depending on the bubble frequency.

Considering the case of the Lusi mud volcano in Indonesia (Table 3.3) and supposing a constant gas flow at the conduit given by $0.2 < Q_g < 2$ m$^3$/s (Vanderkluysen et al. [80]) the numerical model (equation 3.14) suggests that the buoyancy force leads to an effective pressure in the range $0.2 < \Delta P_g < 3 \times 10^5$ Pa. The buoyancy pressure significantly increases considering a smaller radius of the vertical conduit ($0.2 < \Delta P_g < 7 \times 10^5$ Pa when $R = 0.5$ m).

The numerical model represents a simple description of the fluid dynamics involved in volcanoes. It allows for a prediction of the pressure and rise speed of a two-phase fluid along the vent of a volcano. This model treats both the width of the conduit and the viscosity of the mud as constant along the entire height of the volcano. Mud volcanoes systems are extremely complex and in order to improve the accuracy of this model further analysis on the impact of variability in the fluid rheology and the conduit geometry on the eruption should be carried out.

# Chapter 4

# Dispersion in two-dimensional turbulent plumes

## 4.1 Abstract

Eddy-driven mixing within a two dimensional turbulent buoyant plume was investigated using high resolution imaging and dye studies. Instantaneously, the plume consists of a series of eddies, and at each point along the centreline of the plume, the along-plume speed of the leading edge of the eddies, $w_e \approx 1.3f^{1/3}$, where $f$ is the specific buoyancy flux, while the product of the length-scale, $A$, and frequency, $\omega$, of the eddies $\omega A \approx 0.15f^{1/3}$. The circulation and flow associated with the eddies leads to longitudinal mixing relative to the mean flow. To illustrate this mixing, the evolution of the horizontally-averaged dye front produced by adding a constant flux of dye to a steady plume for times $t > 0$ was analysed. The centre of mass of the horizontally-averaged dye front has along-plume speed $w_e \approx 1.04f^{1/3}$. This is consistent with the predictions of a time averaged model for the evolution of the horizontally-averaged mass, momentum and buoyancy flux in the plume. The data also shows that the longitudinal spreading of the horizontally-averaged dye front can be described in terms of a dispersivity $B_z f^{1/3} z$, where $z$ is the vertical distance below the source and $B_z$ is the diffusion coefficient in the $z$-direction. This model of longitudinal mixing enables calculation of the distribution of the residence time of material in the plume, which permits predictions of the evolution of a reaction in the plume where the reaction time is comparable to the travel time in the plume.

## 4.2 Introduction

Mixing and shear dispersion in turbulent flows is important in many natural and industrial processes (Pope [61] and Prandtl [63]). Amongst the many different types of turbulent flow, jets and plumes, which arise from localised sources and are driven by momentum or buoyancy, are especially intriguing (Turner [78] and Carazzo et al. [12]). Applications include volcanic plumes in the atmosphere, hydrothermal plumes in the ocean (Woods [83]), effluent spreading in shallow estuaries and river outflows into shallow lakes (Daoyi and Jirka [19] and Dracos et al. [23]). In the latter cases, the flow may be confined leading to development of an effectively two-dimensional flow. Daoyi and Jirka [19] and Dracos et al. [23] have described the motion of two-dimensional jets both experimentally and theoretically, using integral modelling techniques, and have applied this modelling to understand formation and growth of large eddies in river outflows and the ensuing transport of pollutants into shallow lake environments. As well as modelling the mean properties of the flow, it is of interest to quantify the longitudinal dispersion in such flows, especially if they involve reactions or if chemicals are added to the flow and then become diluted through mixing (Ai et al. [1] and Chen and Jirka [15]). Recent experiments measuring the longitudinal dispersion within two-dimensional jets (Landel et al. [42]) suggest that the local turbulent diffusivity is proportional to the product of the local size and speed of the eddies. By adopting this model, accurate predictions of the longitudinal mixing of a dye front, produced by adding a constant flux of dye to an established jet, can be obtained.

In this work the complementary problem of quantifying the mixing in a two-dimensional turbulent plume, driven by a buoyancy flux ($f$), was explored. In contrast to a jet, the buoyancy flux causes the momentum flux to increase with distance from the source. I characterised the eddies in such two-dimensional plumes, and explored how they influence the longitudinal dispersion in the flow. Although there have been a number of experiments which explore the dynamics of three-dimensional line plumes produced by a uniform line source of buoyancy, in which the scale of the line source exceeds the vertical scale of the flow (Paillat and Kaminski [56] and Bremer and Hunt [9]), the dynamics of a (confined) two-dimensional turbulent plume is different as the eddies can only grow in the along and cross plume direction (as shown in figure 4.1).

First the experimental system is described, and the physics and mathematical modelling of the time averaged steady-state phenomenon is presented. After reporting some measurements of the plume width as a function of distance from the source and the time-averaged salinity of the plume over the domain, I measure the speed of the leading edge of the eddies in the along-plume direction and explore the variation with

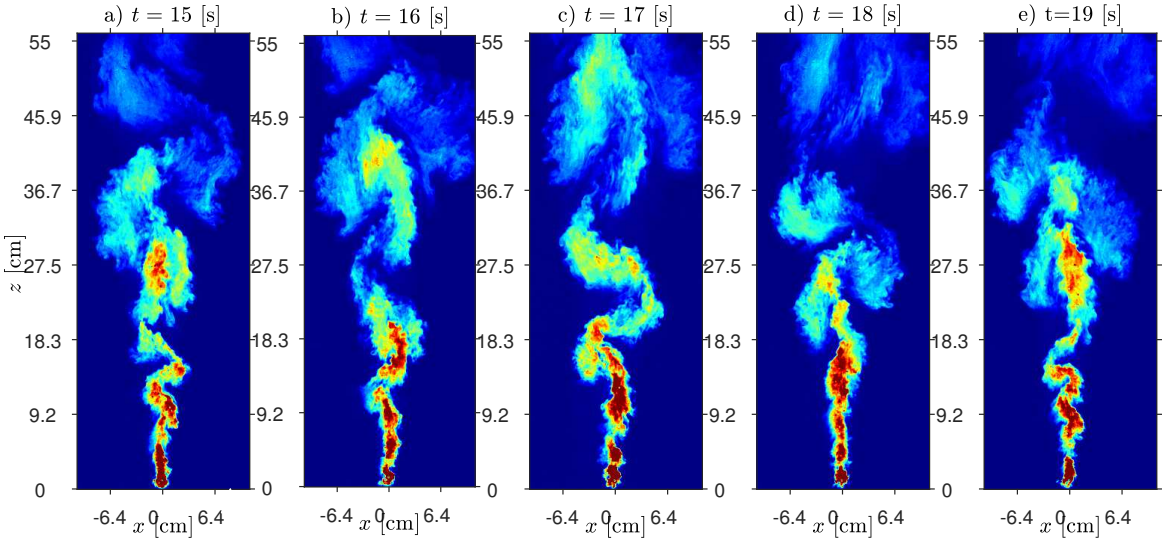


Fig. 4.1 Series of five images illustrating the structure of a two-dimensional plume, and its evolution with time, using a false colour mapping of concentration to highlight the eddies. As the plume advances from the source, eddies develop which mix with ambient fluid, leading to dilution of the plume fluid. In this experiment $s_0 = 17\ wt\%$ and $q_0 = 4.4\ cm^2/s$, where $s_0$ is the initial salinity and $q_0$ is the initial volume flux.

position of the product of the frequency and size of the eddies. The data was used to motivate a phenomenological model of the salinity concentration in the domain and hence the mixing occurring between the two fluids. The results of this model were used to analyse the longitudinal dispersion produced by the eddies.

A comparison of the predictions of the model with the dispersion of the dye front in a series of experiments during which a steady flux of dye was added to the source of a steady plume, for $t > 0$ is introduced. I conclude with a discussion about the implications of this work for calculating the residence time distribution of material in a two-dimensional plume, which is key for understanding the rate of dilution by a plume or reactions in which the reaction time is comparable to or longer than the mean travel time through the plume.

## 4.3 Physics of the Plume

In developing a model of mixing in a two-dimensional plume it is necessary to define the following qualities ( Morton et al. 53 ):

$$Q(z) = \int_{-\infty}^{+\infty} \rho w \mathrm{d}x \quad ; \quad M(z) = \int_{-\infty}^{+\infty} \rho w^2 \mathrm{d}x \quad ; \quad F(z) = \int_{-\infty}^{+\infty} g' w \mathrm{d}x \tag{4.1}$$

where $Q$ is the streamwise mass flux, $M$ is the momentum flux and $F$ is the buoyancy flux. Also, $z$ is the streamwise direction, $x$ the spanwise direction (figure 4.2), $\rho$ is the density of the plume fluid over the domain, $w$ is the speed of the fluid in the $z$-direction and $g'$ is the local buoyancy which is related to the salinity by the relation $g' = (s/s_0)g'_0$. The buoyancy of the source fluid is given by $g'_0 = (\rho_0 - \rho_e)/\rho_e$, where $\rho_0$ and $\rho_e$ are the densities of the aqueous saline solution (the source fluid) with concentration $s_0$, and the environmental fluid, respectively.

Under the hypothesis that the mixing between the two fluids involved does not cause a significant change in the plume fluid density compared to the background density, then we can write the specific mass flux ($q$), specific momentum flux ($m$) and specific buoyancy flux ($f$) per unit length as

$$\begin{cases} q(z) = \bar{w}\bar{b} = \int_{-\infty}^{+\infty} w \mathrm{d}x \\ m(z) = \bar{w}^2\bar{b} = \int_{-\infty}^{+\infty} w^2 \mathrm{d}x \\ f(z) = \bar{g'}\bar{w}\bar{b} = \int_{-\infty}^{+\infty} g' w \mathrm{d}x \end{cases} \tag{4.2}$$

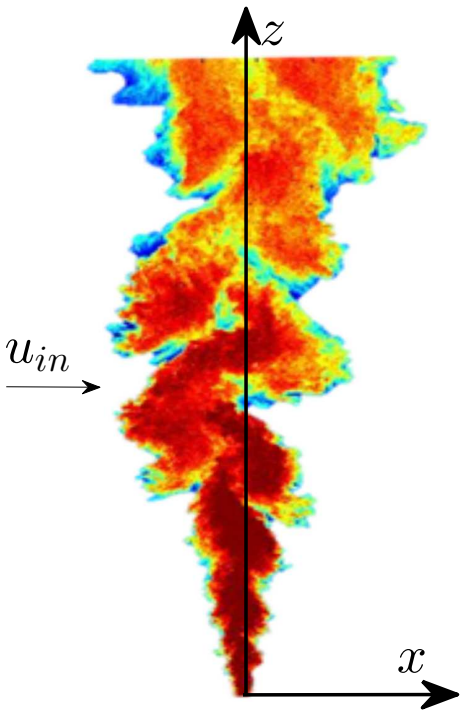


Fig. 4.2 Plume image illustrating the orientation of the axes.

where $\bar{b}$ is the effective width of the plume, $\bar{w}$ is the horizontally-averaged vertical speed, and $\bar{g'}$ is the horizontally-averaged buoyancy.

In the case that the fluids are incompressible and the density difference between the two fluids is small, Boussinesque approximation may be adopted in which we assume the density changes are only important in determining the buoyancy force (Ai et al. [1]). For such a turbulent flow the volume flux increases with height as a result of the entrainment and mixing of the ambient fluid by the plume. The detailed process of entrainment involves the engulfment of finite parcels from the ambient that are then incorporated into the plume by the mixing, as eddies overturn within the plume. However, on timescales long enough compared with the eddy-turnover time, the entrainment process can be modelled in terms of a mean horizontal inflow velocity ($u_{in}(z)$) of the surrounding fluid that is proportional to the vertical speed in the plume by an entrainment coefficient ($\epsilon$), $u_{in}(z) = \epsilon\bar{w}(z)$. Applying the equations of conservation of mass, momentum and buoyancy, we obtain the following modelling equations for the plume:

$$\begin{cases} \frac{\mathrm{d}q}{\mathrm{d}z} = 2\epsilon\bar{w} \\ \frac{\mathrm{d}m}{\mathrm{d}z} = kf/\bar{w} \\ \frac{\mathrm{d}f}{\mathrm{d}z} = -N^2 q \end{cases} \tag{4.3}$$

where $k$ is a constant depending on the horizontal structure of the ensemble time-averaged velocity and buoyancy, and $N$ is a term that quantifies the stratification of the environmental fluid, defined as $N^2 = \frac{-g}{\rho_e}\frac{\mathrm{d}\rho_e}{\mathrm{d}z}$, which in the case of my experiments, where $N = 0$, suggests that the specific buoyancy flux is constant. In the cases considered the equations 4.3 can be written as

$$\begin{cases} q\frac{\mathrm{d}q}{\mathrm{d}z} = 2\epsilon m \\ m\frac{\mathrm{d}m}{\mathrm{d}z} = kfq \\ f = f_0 = const \end{cases} \tag{4.4}$$

with solution

$$q = [q_0^3 + \frac{2\epsilon}{kf}(m^3 - m_0^3)]^{1/3} \tag{4.5}$$

Far from the plume source the solution can be written as

$$\begin{cases} \bar{w} = (\frac{kf}{2\epsilon})^{1/3} \\ \bar{b} = 2\epsilon z \\ q = q_0 + (2\epsilon)^{2/3}(kf)^{1/3}z \\ m = m_0 + (2\epsilon)^{1/3}(kf)^{2/3}z \end{cases} \tag{4.6}$$

This solution applies once the buoyancy-driven momentum flux, as given by $(2\epsilon)^{1/3}z(kf/)^{2/3}$, exceeds the initial momentum flux $m_0$; this corresponds to $z \gg L_j$, where the jet length $L_j = m_0/(2\epsilon)^{1/3}(kf)^{2/3}$. In the experimental cases it was also needed to assess the $L_{j0} = m_0/f^{2/3}D_0$ which represents the length scale over which the initial momentum of the source fluid dominates the flow over rather than the buoyancy of the flow. For most of the experiments tabulated in table 4.1, I estimate that $L_{j0}$ has a value smaller than 15 cm, while the tank is 70cm deep. Beyond this adjustment region the ensemble-averaged flow speed is expected to be constant, and the plume width to increase linearly with height. In fact, in addition to the jet length, in our experimental system, the diameter of the source is one half of the width of the tank, and so in the immediate vicinity of the source, the plume is three dimensional; however, within $2-3$ cm it evolves into a two-dimensional plume following rapid entrainment and mixing.

## 4.4 Experimental Apparatus

A series of experiments was conducted to analyse the mixing involved in a two-dimensional turbulent buoyant plume, during which an aqueous saline solution was injected from a 5mm nozzle ($D_0$) into the $1 \pm 0.1$cm width gap between two rectangular plexiglass plates of dimension 70cm×70cm. The system was immersed in a larger reservoir tank so that plume fluid could leave the domain on reaching the base, and ambient fluid could enter the sides as fluid was entrained by the plume as shown in figure 4.3. A systematic series of experiments was carried out, in which the aqueous solution supplied to the plume had flow rates in the range 1-20 cm$^3$/s and salinities which ranged from 1-17 wt % (Table 4.1). This led to flows with Reynolds numbers, $Re = \frac{\rho_0 w_0 D_0}{\mu}$, of order 100-2000, where $\rho_0$ is the density of the fluid injected and $w_0$ is the speed of the outflow at the source. As shown by Landel et al. [43] for such flow rates, the frictional stress on the walls of the tank is small over the vertical extent of the plume, and so the frictional effects may be neglected.

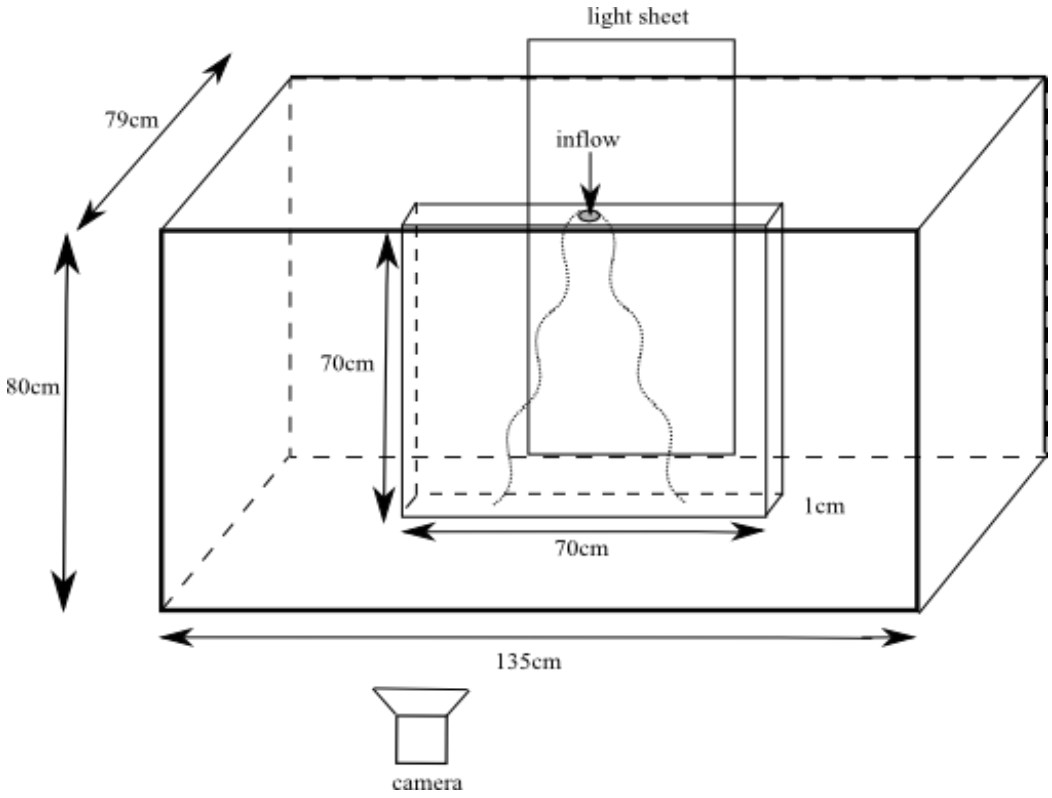


Fig. 4.3 Schematic of the experimental apparatus

| Exp. | $s_0$ (wt%) | $q_0$ ($cm^2/s$) | $f$ ($cm^3/s^3$) | $L_{j0}$ (cm) | $Ri$ | $Re$ |
|---|---|---|---|---|---|---|
| 1 | 1 | 1 | 6.9 | 0.55 | 1.7 | 99.8 |
| 2 | 1 | 2 | 13.9 | 1.35 | 0.4 | 199.6 |
| 3 | 1 | 3 | 20.8 | 2.35 | 0.2 | 299.4 |
| 4 | 1 | 5 | 34.7 | 4.65 | 0.1 | 499 |
| 5 | 1 | 9.9 | 69.4 | 11.7 | 0.0 | 998 |
| 6 | 1 | 14.9 | 104.1 | 20.1 | 0.0 | 1497 |
| 7 | 1 | 19.9 | 138.8 | 29.55 | 0.0 | 1996 |
| 8 | 2.9 | 1 | 20 | 0.25 | 5.1 | 99.8 |
| 9 | 2.9 | 2 | 39.9 | 0.65 | 1.3 | 199.6 |
| 10 | 2.9 | 2.9 | 59.9 | 1.15 | 0.6 | 299.4 |
| 11 | 2.9 | 4.9 | 99.8 | 2.25 | 0.2 | 499 |
| 12 | 2.9 | 9.8 | 199.7 | 5.65 | 0.1 | 998 |
| 13 | 2.9 | 14.7 | 299.5 | 9.7 | 0.0 | 1497 |
| 14 | 4.8 | 1 | 32.7 | 0.2 | 8.5 | 99.8 |
| 15 | 4.8 | 1.9 | 65.5 | 0.45 | 2.3 | 199.6 |
| 16 | 4.8 | 2.9 | 98.2 | 0.8 | 1.0 | 299.4 |
| 17 | 4.8 | 4.8 | 163.7 | 1.55 | 0.4 | 499 |
| 18 | 4.8 | 9.7 | 327.4 | 3.95 | 0.1 | 998 |
| 19 | 4.8 | 14.5 | 491.1 | 6.8 | 0.0 | 1497 |
| 20 | 9.1 | 0.9 | 60.8 | 0.1 | 20.0 | 99.8 |
| 21 | 9.1 | 1.9 | 121.6 | 0.3 | 4.5 | 199.6 |
| 22 | 9.1 | 2.8 | 182.3 | 0.5 | 2.1 | 299.4 |
| 23 | 9.1 | 4.7 | 303.9 | 1 | 0.7 | 499 |
| 24 | 9.1 | 4.7 | 303.9 | 1 | 0.7 | 499 |
| 25 | 9.1 | 9.4 | 607.8 | 2.45 | 0.2 | 998 |
| 26 | 9.1 | 14.1 | 911.6 | 4.25 | 0.1 | 1497 |
| 27 | 9.1 | 18.8 | 1215.5 | 6.2 | 0.0 | 1996 |
| 28 | 17 | 0.9 | 110 | 0.05 | 38.2 | 99.8 |
| 29 | 17 | 1.8 | 220 | 0.15 | 9.5 | 199.6 |
| 30 | 17 | 2.7 | 330 | 0.3 | 4.2 | 299.4 |
| 31 | 17 | 4.4 | 550 | 0.6 | 1.6 | 499 |
| 32 | 17 | 8.9 | 1099.9 | 1.5 | 0.4 | 998 |
| 33 | 17 | 13.3 | 1649.9 | 2.55 | 0.2 | 1497 |
| 34 | 17 | 17.8 | 2199.9 | 3.75 | 0.1 | 1996 |

Table 4.1 A summary of the experiments carried out specifying the initial salt concentration ($s_0$), the initial volume and specific buoyancy fluxes per unit length ($q_0$ and $f$), the jet length ($L_{j0}$) and the source Richardson ($Ri = \frac{D_0 g \Delta\rho}{\rho_0 w_0^2}$)and Reynolds numbers.

The flow was recorded by a 3Hz series of photographs using a computer controlled Nikon D90 camera placed 2.5m far from the tank which was backlit by an electroluminescent sheet (W&Co LED panel 100 x 60 cm) in an otherwise dark room. The experiments were run by initially injecting a clear saline solution and, once a quasi steady plume was established, the source fluid was switched to a dyed mixture of saline solution with the same density as the previous one. The execution of this method required a double-head-pump, able to circulate both fluids at the same speed concurrently with one supplying the tank and one bypassing the tank. A switch was also used allowing the supply fluid to be interchanged. In each experiment, the plume fluid was dyed with a uniform initial intensity of red food dye (3g/l). Prior to the actual experiment, a series of calibration experiments were carried out in which mixtures of the aqueous saline solution, fresh water and dye at different concentrations were photographed. These were used to generate a calibration curve relating the light intensity recorded by the camera with the dye content and hence the salinity of the fluid. With this calibration, it was possible to measure the salinity ($s$) of the fluid in the tank domain and, during the course of each experiment, this was within 4-5 % of the known supply of salt in the aqueous saline solution.

In all subsequent images the plume fluid is shown rising from the bottom to the top of the image, as would be the case for a positively buoyant flow. This is for consistency and to help in interpretation with the existing literature (*c.f.* Morton et al. [53] and Papanicolaou and List [57]). In actual practice the flow was of negatively buoyant aqueous saline solution, and descended to the base of the tank, and so the images are shown upside-down.

## 4.5 Time averaged concentration

The ensemble-averaged concentration ($\bar{c} = (\int_0^T s(x,y,t)/s_0 \mathrm{d}t)/T$) was measured by averaging 150 frames from a quasi-steady period of flow corresponding to approximately 50 s ($T$). The diameter of the plume increases proportionally with $z$, as shown in figure 4.4, suggesting, according to equation 4.6b, that the entrainment coefficient is constant (Morton et al. [53]).

In previous literature $\bar{c}$ is described by the empirical law

$$\bar{c}(x,z) = \bar{c}(0,z)e^{-(\frac{x}{\lambda z})^2} \tag{4.7}$$

where $\lambda$ is an arbitrary constant; this description is consistent with the data obtained, as shown in figure 4.5. From the time-averaged data it was possible to track the horizontal

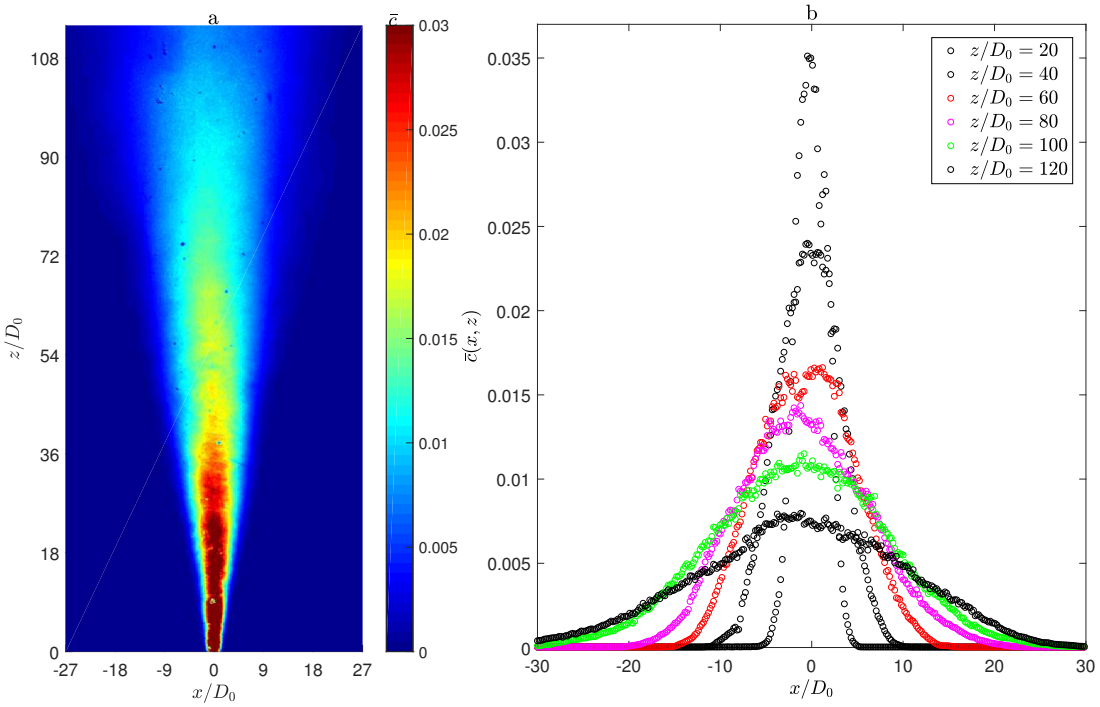


Fig. 4.4 (a) Time averaged concentration over the domain. (b) Time averaged concentration in the spanwise direction ($x$) at different distances from the source. The data in this figure were obtained from experiment number 32

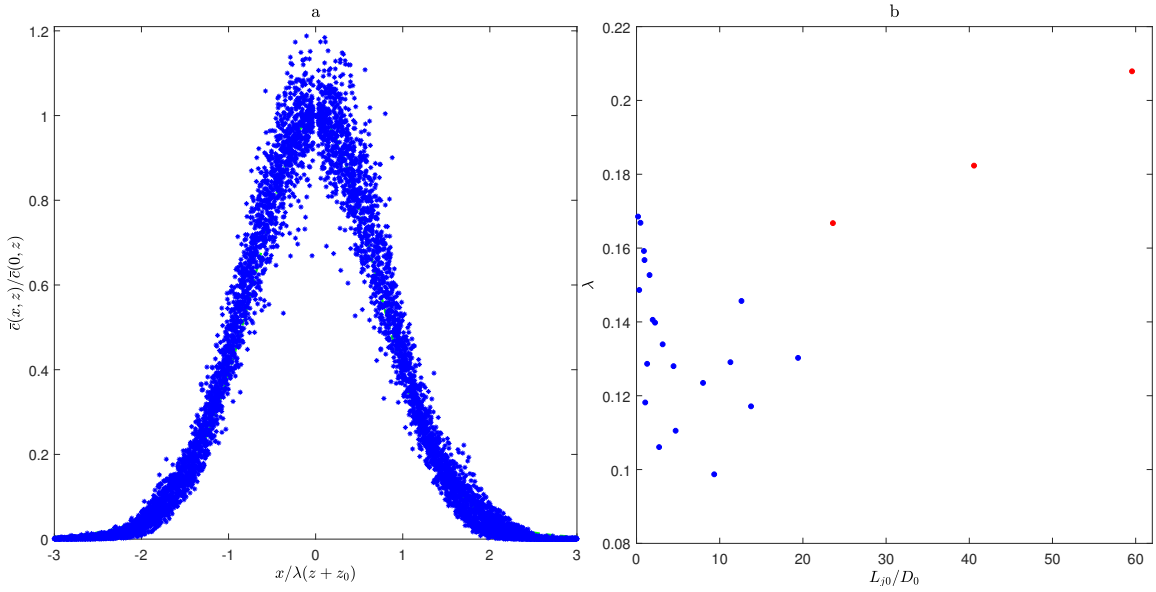


Fig. 4.5 (a) time averaged concentration scaled according eq 4.7 showing data obtained from experiment number 32. (b) Plot of the ratio $d/z$ over the jet length $L_{j0}$ for each experiment.

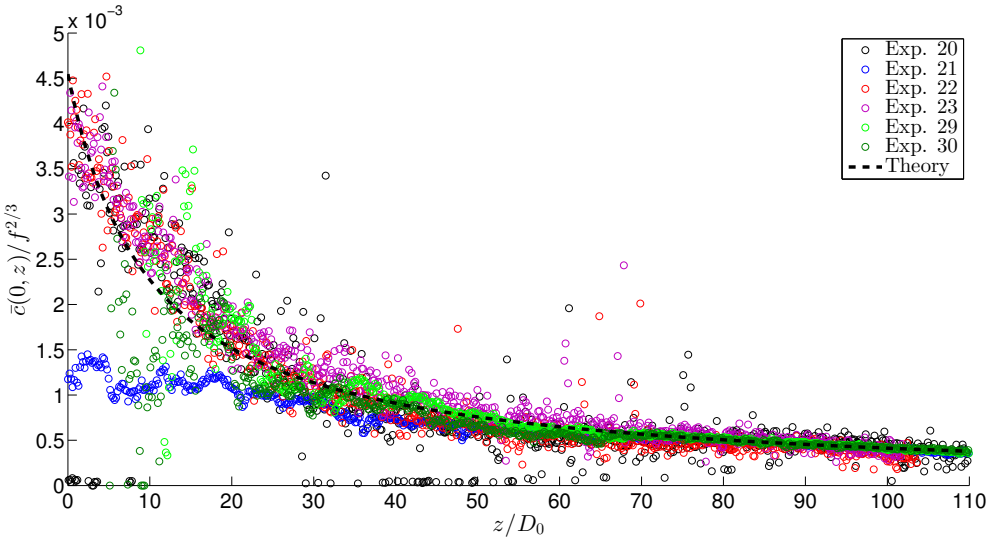


Fig. 4.6 Plot of the time averaged concentration along the symmetry axis $x = 0$ for a series of different experiments which are listed in the figure legend.

distance $d(z)$ over which the concentration $\bar{c}$ falls by a factor $e$. $d$ scales linearly with height above the source, independently of the buoyancy flux, according to the relation $d = \lambda z$, where $\lambda = 0.142 \pm 0.016$ (figure 4.5b). This result is consistent with values obtained in previous 3D line source plume studies: Kotsovinos [38] found $\lambda = 0.13$ while Yih [84] and Paillat and Kaminski [56] report $\lambda = 0.15$. The experiments show that $\lambda$ is approximately constant for distances $z > L_{j0}$ and since the tank extends a distance $120 * D_0$ from the source, I analyse experiments in which $L_{j0}/D_0 \leq 20$. For $L_{j0}/D_0 \geq 20$ the apparent value of $\lambda$ increases since, for such large jet length, the flow is influenced by both initial momentum and buoyancy.

Remembering that the time-averaged concentration is related to the buoyancy by the relation $f = \bar{w}\bar{b}g_0'\bar{c}$ and according to the results in equation 4.6a it follows that

$$\bar{c}(0,z) \propto \frac{f^{2/3}}{z} \tag{4.8}$$

This result is consistent with the experimental data, (Fig. 4.6) but it is important to note that the data have been shifted along the z-axes to correct for the virtual origin associated with the flow in the region $z \leq L_{j0}$ and the limits imposed by the experimental apparatus.

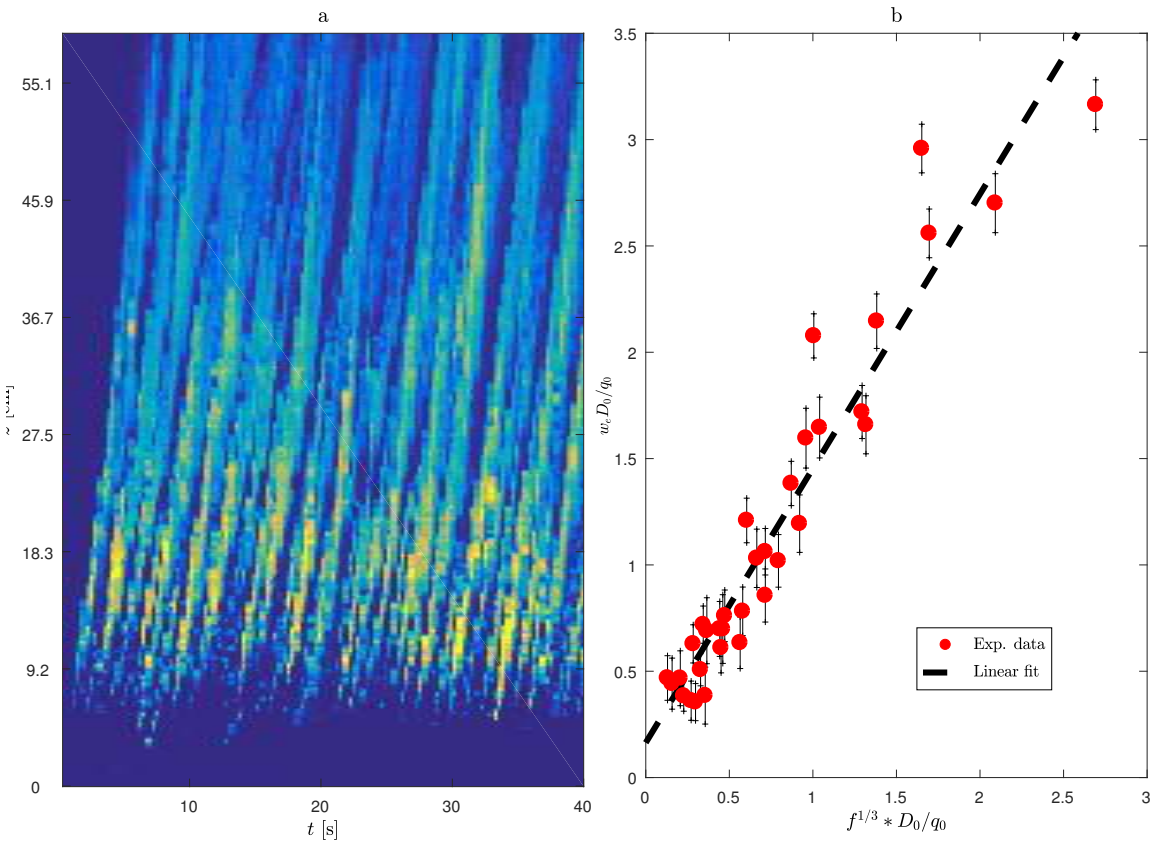


Fig. 4.7 (a) Time series of a vertical line of pixels located at $x = 3D_0$ from the centerline of the plume. The image is shown in false colour, to illustrate the passage of the front of successive eddies. The data in these figures was collected from experiment 31. (b) Variation of the speed of the front of the plume ($\bar{w}$) for a large number of different buoyancy fluxes, as determined from figures such as 4.7a for $x = 0$. The data collapse to the simple relation $w_e(0, z) \approx 1.30 f^{1/3}$.

## 4.6 Model of the Dispersive Mixing

In order to model the dispersion of the dye it was appropriate firstly to characterise the properties of the eddies. The speed of the front of the eddies was tracked as they advanced through the tank by constructing a vertical time series along a line close to the centreline ($x = 3D_0$) of the plume (Fig. 4.7a). This line is shown in false colour to enhance the contrast between the background and the plume fluid which is dyed red at source. The image illustrates that there is a regular series of fronts which migrate through the tank, and that as each front migrates, the colour contrast across the front decreases; these correspond to the leading edge of successive eddies, which mix and become diluted with ambient fluid. The speed of these fronts can be found by using a Hough transform which estimates the gradient of the lines. The measurements of the rise speed show that the eddies attain a nearly constant speed within 10 cm of the source. The measured rise speed then remains nearly constant along the final 50 cm. The procedure has been repeated for a series of experiments with different buoyancy fluxes $f$ (Table 4.1), and in Fig. 4.7b it is shown the measured speed of the front of the plume ($w_e$) as a function of the buoyancy flux at the source, illustrating that the data collapse to the relation

$$w_e = (1.3 \pm 0.1) f^{1/3} \tag{4.9}$$

It was then important to characterise the horizontal fluctuations in the position of the eddies. Fig. 4.8 illustrates a time series showing the variation with time of the concentration of the fluid along a horizontal line through the plume at a distance $z = 42$cm below the source. This false colour image illustrates how, as the plume evolves, the location of successive eddies passing this point oscillates to the left ($x > 0$) and right ($x < 0$) of the source. Using the information of the concentration ($c(x, z, t)$) it was possible to track the centre of the plume defined as $X_c = (X_1 + X_2)/2$, where $X_1 : c(x \leq X_1, z, t) \leq \frac{max(c(x,z,t))}{e^1}$ and $X_2 : c(x \geq X_2, z, t) \leq \frac{max(c(x,z,t))}{e^1}$. It was possible to measure the frequency of the passage of the vortices ($\omega$), by measuring the frequency of the horizontal oscillation of the plume around the centerline ($X_c$). I also measured the horizontal distance $d^* = X_2 - X_1$ at a specific time instant. I then find a time-average of $d^*$, defined as $d^*_m(z)$, for each value of the vertical distance $z$ from the source.

Figure 4.9d shows the variation of $d^*_m$ as a function of $z$. $d^*_m$ is considerably smaller than $d$, the width of the ensemble time averaged flow (figure 4.9d). This reflects the difference between the actual dilution of the fluid, as measured by $d^*_m$, and the width

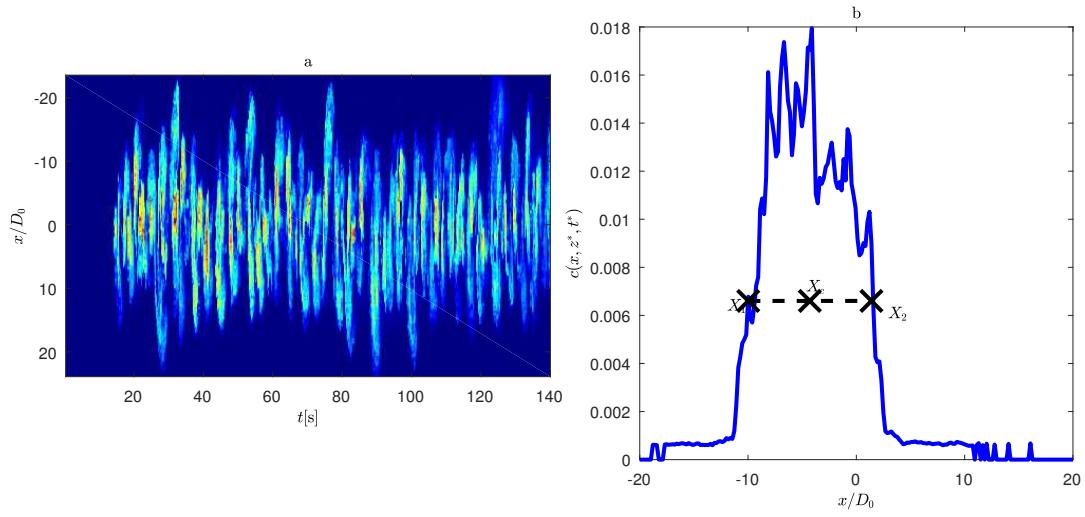


Fig. 4.8 (a) Time series of a horizontal line in the plume ($z^* = 42$ cm), using false colour to show how the stream of eddies pass by this line, with successive eddies migrating left or right relative to the source. (b) Plot of the concentration along a horizontal line ($z^* = 42$ cm $t^* = 40$ s) with evidence of the limits of the diameter of the plume (both the plots are constructed from data obtained in experiment 31).

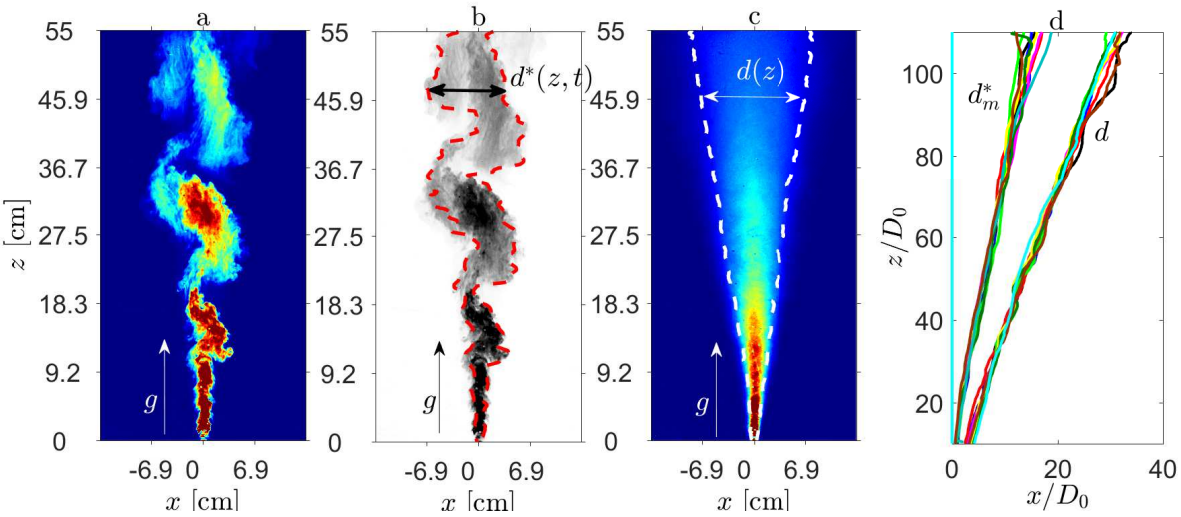


Fig. 4.9 (a) Photograph of the instantaneous structure of a typical two dimensional plume, in steady state. (b) Location of the two bounding lines defining the local diameter $d^*(z,t)$. (c) Time averaged concentration profile. (d) Horizontal distance $d(z)$ from the centreline as a function of the distance from the source. Also shown is a characteristic cross-plume length scale ($d^*_m$). At each height, this scale is determined as a time average of the data $d^*(z,t)$. Fig 4.9(a), 4.9(b) and 4.9(c) shows data for experiment 31.

of the time-averaged concentration field $d$, which captures the combined effect of the dilution plus the horizontal oscillation of the position of the flow. If the horizontal variation of concentration, relative to the centre of the plume, and the position of the centre of the plume relative to the centre of the tank, both follow a normal distribution, with variance $\sigma_{d^*_m}$ and $\sigma_o$ then the variance of the joint distribution, $\sigma_d$ is the sum of the variance of each distribution, $\sigma_d = \sigma_o + \sigma_{d^*_m}$, with the $e$-folding distances given by $\sqrt{\sigma_{d^*_m}}$, for the actual dilution of the fluid, and $\sqrt{\sigma_d}$ for the time-averaged concentration field. Given the $e$-folding distances $d \sim 0.28z$ and $d^*_m \sim 0.14z$ (Fig 4.9d) it follows that $\sigma_o \approx 3\sigma_{d^*_m}$, so the variance in concentration associated with the oscillations is about 3 times that of the actual dilution.

Since the plume flow is essentially composed of eddies, it was expected that the frequency of the eddies, $\omega$, times their characteristic length scale, $d^*_m$, should scale with the mean speed of the flow. Since the speed is a constant proportional to $f^{1/3}$ (Fig 4.7), it results that $\omega d^*_m$ will be independent of distance from the source. Figure 4.10 illustrates the value of $\omega d^*_m / f^{1/3}$ as a function of the distance from the source. Similar data was collected for experiments with different buoyancy fluxes (Table 4.1) and suggest that, beyond a flow adjustment zone which extends over a region of about

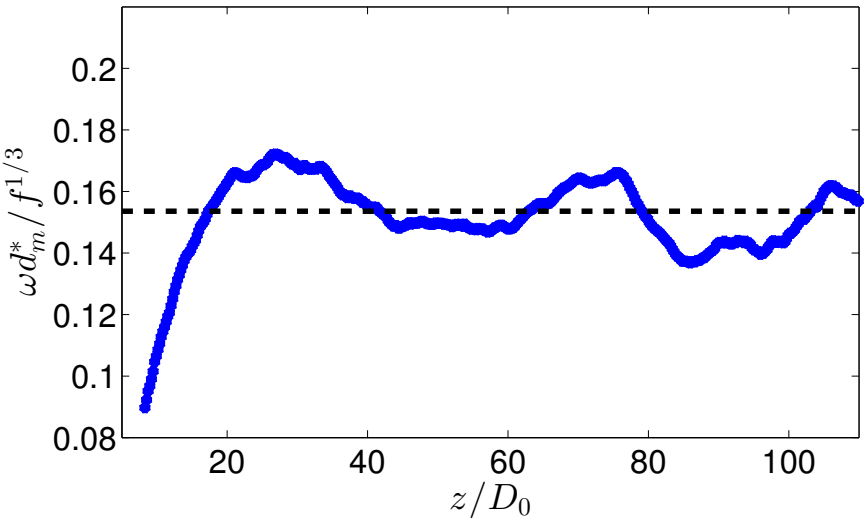


Fig. 4.10 Time average of the product of frequency and the length-scale of the eddies as a function of distance from the source, $z$. Data from one experiment is shown illustrating how the data collapse to a common limit away from the source (exp. 31).

15 cm ahead of the source, the quantity $\omega d_m^*/f^{1/3} \approx 0.16 \pm 0.01$. This result is also consistent with dimensional analysis.

### 4.6.1 Horizontally averaged longitudinal mixing.

It is possible to model the influence of the dispersive mixing on the horizontal integral of concentration along the plume by assuming that the mixing is produced by the interaction of the time-dependent eddies with the mean flow. Using the results relating to the speed, frequency and length-scale of the eddies, and adopting concepts from classical models of mixing length theory (Prandtl [62]) and turbulent dispersion (Taylor [75]) it is expected that over time scales long compared to the eddy turnover time, the eddies lead to an effective dispersivity which scales as $zf^{1/3}$. It is possible to make the hypothesis that the horizontal-integral $C(z,t) = \int_{-\infty}^{\infty} c(x,z,t)\mathrm{d}x$ of the ensemble-averaged concentration evolves according to the phenomenological conservation law (Fischer [25])

$$\frac{\partial C}{\partial t} + \alpha f^{1/3}\frac{\partial C}{\partial z} = \frac{\partial}{\partial z}\left(\alpha B_z z f^{1/3}\frac{\partial C}{\partial z}\right) \tag{4.10}$$

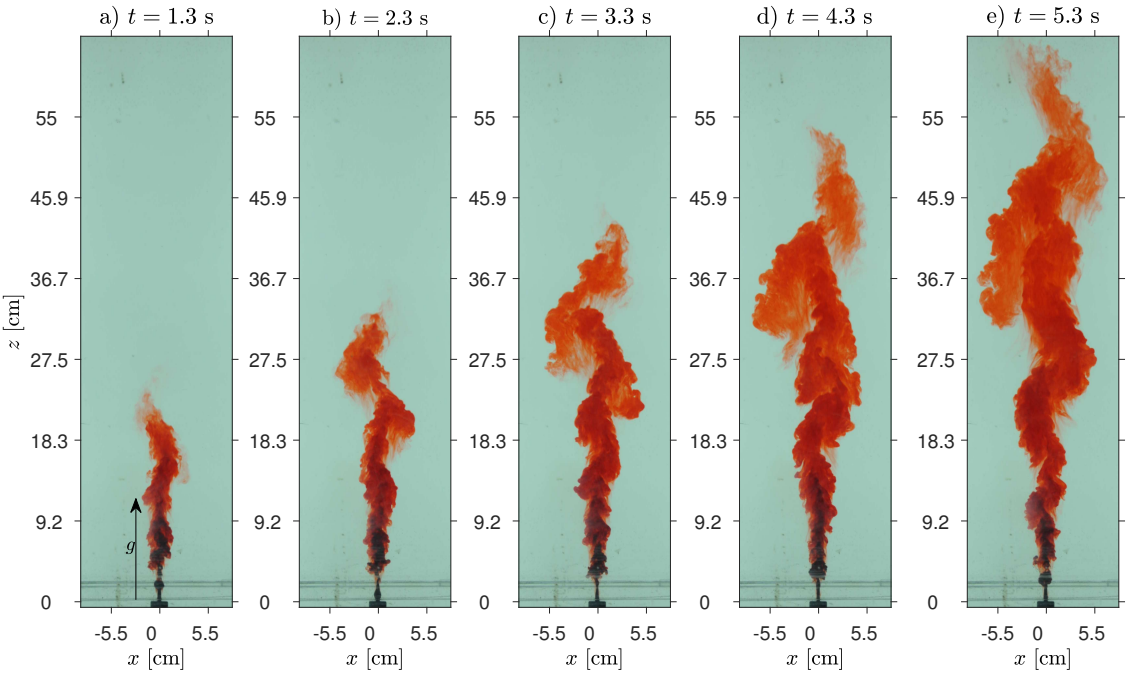


Fig. 4.11 Photograph of an evolving two-dimensional line plume, illustrating how red dye, injected into the established steady plume evolves with time. Pictures are shown for experiment 30.

where $\alpha$ is the constant which determines the mean speed of the dye front. By comparing the solutions of this equation with our experimental data (Fig. 4.12), it is possible to estimate values for $\alpha$ and $B_z$.

Equation 4.10 can be used to describe the advance of a front of dye within a steady plume of buoyancy flux $f$ (Fig. 4.11). If there is a flux of dye $Q_c$ released into the plume at $z = 0$ for $t \geq 0$, then the horizontally averaged concentration may be written as

$$C(z,t) = \frac{Q_c}{f^{1/3}} \mathcal{H}\left(\frac{z}{f^{1/3}t}\right) \tag{4.11}$$

where $\eta_2 = \frac{z}{f^{1/3}t}$ and $\mathcal{H}$ satisfies the relation

$$-\eta_2 \frac{d\mathcal{H}}{d\eta_2} + \alpha \frac{d\mathcal{H}}{\mathrm{d}\eta_2} = \alpha B_z \frac{d}{d\eta_2}\left(\eta_2 \frac{d\mathcal{H}}{d\eta_2}\right) \tag{4.12}$$

and the expression for the global conservation of dye

$$\int_0^\infty \mathcal{H}(\eta_2) d\eta_2 = 1 \tag{4.13}$$

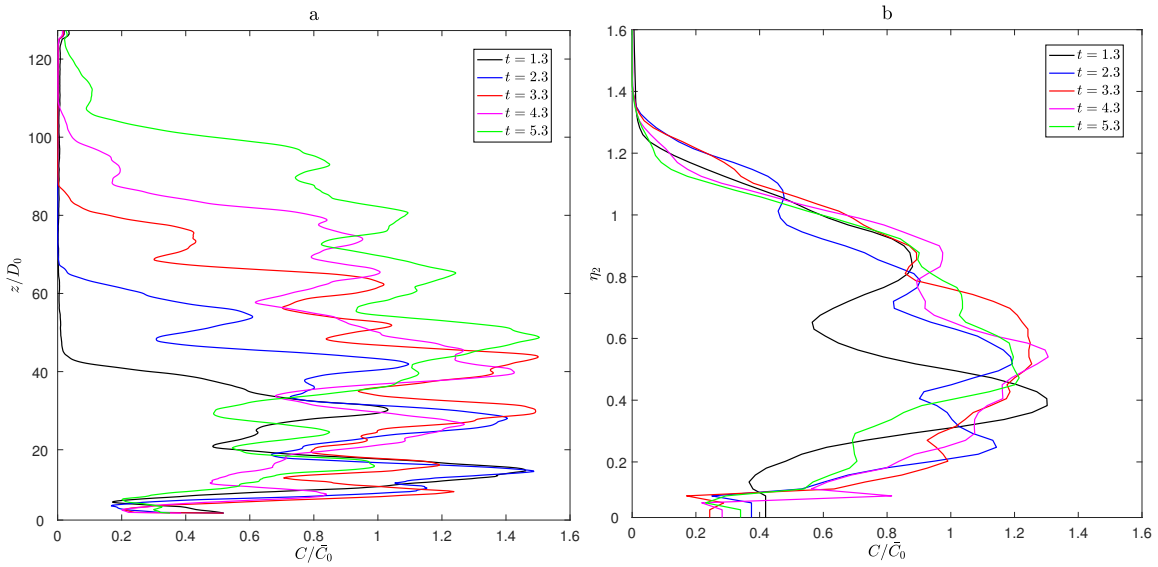


Fig. 4.12 (a) Experimental data showing the horizontally-integrated concentration of dye in the plume as a function of $z$ at five times after the start of steady injection of red dye into the plume at $t = 0$. (b) Integral of the concentration at different time steps as a function of $\eta_2 = z/(t * f^{1/3})$; exp31

This leads to the solution

$$\mathcal{H}(\eta_2) = \frac{\int_{\eta_2}^{\infty} \zeta^{(1/B_z)-1} \exp\left(-\frac{\zeta}{\alpha B_z}\right) \mathrm{d}\zeta}{\int_{o}^{\infty} \zeta^{1/B_z} \exp\left(-\frac{\zeta}{\alpha B_z}\right) \mathrm{d}\zeta} = \frac{\Gamma\left(\frac{1}{B_z}, \frac{\eta}{\alpha B_z}\right)}{\Gamma\left(\frac{1}{B_z} + 1, 0\right)} \tag{4.14}$$

where it is required that $\mathcal{H} \to 0$ as $\eta_2 \to \infty$ and $\Gamma(a, b)$ is the incomplete Gamma function.

The solution in equation 4.14 for the horizontally-integrated concentration was compared with experimental data in which a steady flux of dye is added to an established plume at $t = 0$ (Fig. 4.11). As the dye spreads downstream, the horizontal integral of concentration was measured as a function of the scaled distance $z/f^{1/3}t$ (Fig. 4.12) for each experiment. By taking the ensemble average of 15 experiments, the best fit model (equation 4.14) was estimated corresponding to the parameters $\alpha = 1.04 \pm 0.11$ and $B_z = (1.93 \pm 0.22) \times 10^{-2}$ (Fig. 4.13a), where $\alpha f^{1/3}$ corresponds to the speed of the centre of mass of the front, and $\alpha B_z f^{1/3} z$ the dispersivity relative to this point.

Using this model it was also found the residence time distribution of a finite pulse of dye added to the system at $t = 0$ (Danckwerts [18]); the residence time distribution provides information about the variation with time of the horizontally-averaged concentration of tracer passing a horizontal plane above the source. Such

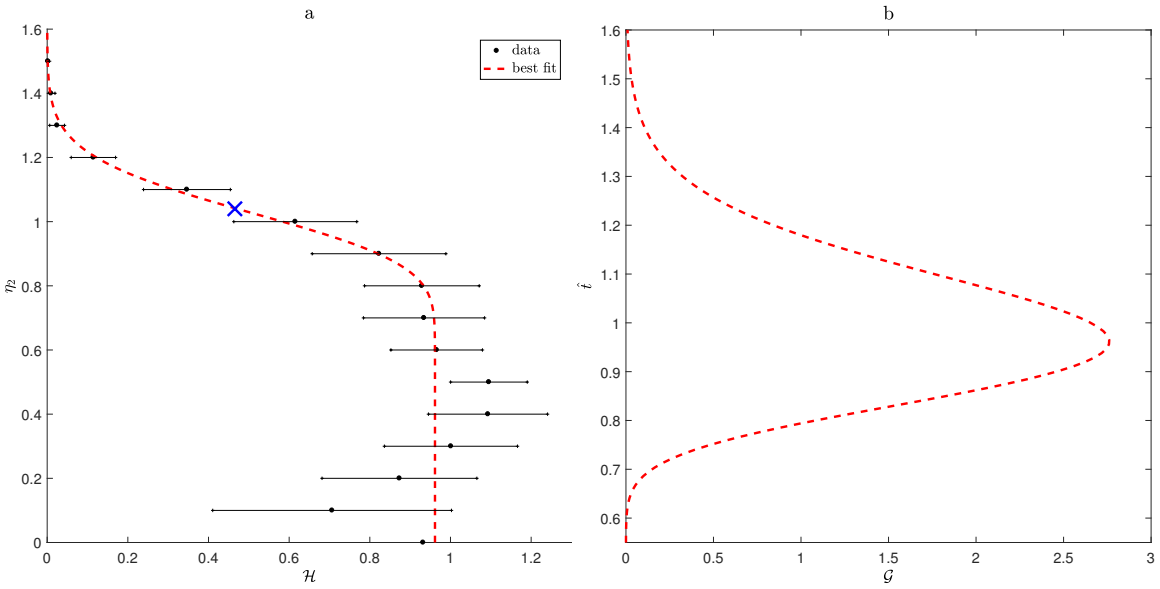


Fig. 4.13 (a) Mean integral of the concentration obtained by averaging the mean integral concentrations of 15 experiments as a function of $z/(tf^{1/3})$, the position of the center of mass has been identified with a blue cross. (b) Variation of the horizontally averaged concentration as a function of time, passing the point $z_o = 1$, which results from an instantaneous release of a finite mass of tracer at $z = 0$, as obtained from equation 4.18.

information can be key for modelling the products of chemical reactions in the plume produced, especially when the reaction time is comparable to the travel time through the plume, so that the distribution of travel times lead to different degrees of partial reaction. With a point release of tracer of finite mass $V_c$ (per unit distance in the y direction), the horizontal integral of concentration follows a solution of the form

$$C(z,t) = \left(\frac{V_c}{f^{1/3}t}\right)\mathcal{G}(\eta_2) \tag{4.15}$$

where the global conservation of mass requires

$$\int_0^\infty \mathcal{G}(\eta_2)\mathrm{d}\eta_2 = 1 \tag{4.16}$$

and $\mathcal{G} \to 0$ as $\eta_2 \to 0$. With these conditions, $\mathcal{G}(\eta_2)$ satisfies the equation

$$-\frac{\mathrm{d}}{\mathrm{d}\eta_2}(\eta_2\mathcal{G}) + \alpha\frac{\mathrm{d}}{\mathrm{d}\eta_2}\mathcal{G} = \alpha B_z\frac{\mathrm{d}}{\mathrm{d}\eta_2}\left(\eta_2\frac{\mathrm{d}}{\mathrm{d}\eta_2}\mathcal{G}\right) \tag{4.17}$$

and has solution

$$\mathcal{G}(\eta_2) = \frac{\left[\eta_2^{1/B_z} \exp\left(-\eta_2/\alpha B_z\right)\right]}{\left[\int_0^\infty \eta_2^{1/B_z} \exp\left(-\eta_2/\alpha B_z\right) \mathrm{d}\eta_2\right]} = \frac{\left[\eta_2^{1/B_z} \exp\left(-\eta_2/\alpha B_z\right)\right]}{(\alpha B_z)^{\frac{\alpha}{\alpha B_z+1}} \Gamma\left(\frac{1}{B_z}+1\right)} \tag{4.18}$$

If an observer at position $z_o$ records the concentration with time, then the distribution of horizontally-integrated concentration passing $z_o$ has time dependence $C(z_o, t)$ as illustrated in figure 4.13b as a function of the dimensionless time $\hat{t} = tf^{1/3}/z_o$. The mean time, $\tau$, and the variance in time, $\sigma$, of the concentration pulse passing $z_o$ are given by

$$\tau = \frac{\int_0^\infty tC(z_o,t)\mathrm{d}t}{\int_0^\infty C(z_o,t)\mathrm{d}t} \quad ; \quad \sigma = \frac{\int_0^\infty t^2 C(z_o,t)\mathrm{d}t}{\int_0^\infty C(z_o,t)\mathrm{d}t} - \tau^2 \tag{4.19}$$

Using the values for $\alpha$ and $B_z$ based on the experimental data, it was found that the dimensionless mean residence time is approximately 1.0 and the dimensionless standard deviation $\sqrt{\sigma} \sim 0.15\tau$. In dimensional variables, the mean residence time and standard deviation in residence time at a point $z_o$ then have values $z_o/f^{1/3}$ and $0.15z_o/f^{1/3}$.

### 4.6.2 Cross flow mixing.

I can generalise the analysis of the longitudinal mixing in terms of the cross-flow and longitudinal mixing to determine the distribution of the time averaged properties across the plume. According to the balance equation of $\bar{c}$ in steady-state conditions (Fischer [25])

$$\frac{\partial \bar{c}}{\partial t} + \underline{\bar{V}} \cdot \underline{\nabla}\bar{c} = \underline{\nabla} \cdot (\underline{\underline{K}} \cdot \underline{\nabla}\bar{c}) \tag{4.20}$$

where $\underline{\bar{V}} = \left\{ \begin{array}{c} \bar{u} \\ \bar{w} \end{array} \right\}$ is the average speed vector with $\bar{u}$ and $\bar{w}$ as horizontal and vertical components of the speed, $\underline{\underline{K}} = \begin{bmatrix} B_x\bar{w}z & 0 \\ 0 & B_z\bar{w}z \end{bmatrix}$ and $B_x$ and $B_z$ are the diffusion coefficients in the $x$ and $z$ direction. In steady state, the concentration of tracer decreases with distance along and across the plume in a self-similar fashion and this may be seen by writing:

$$\bar{c} \propto \frac{\bar{c_2}(\eta)}{z} \quad , \quad \eta = x/z \quad , \quad \zeta = B_x/B_z \quad ,$$

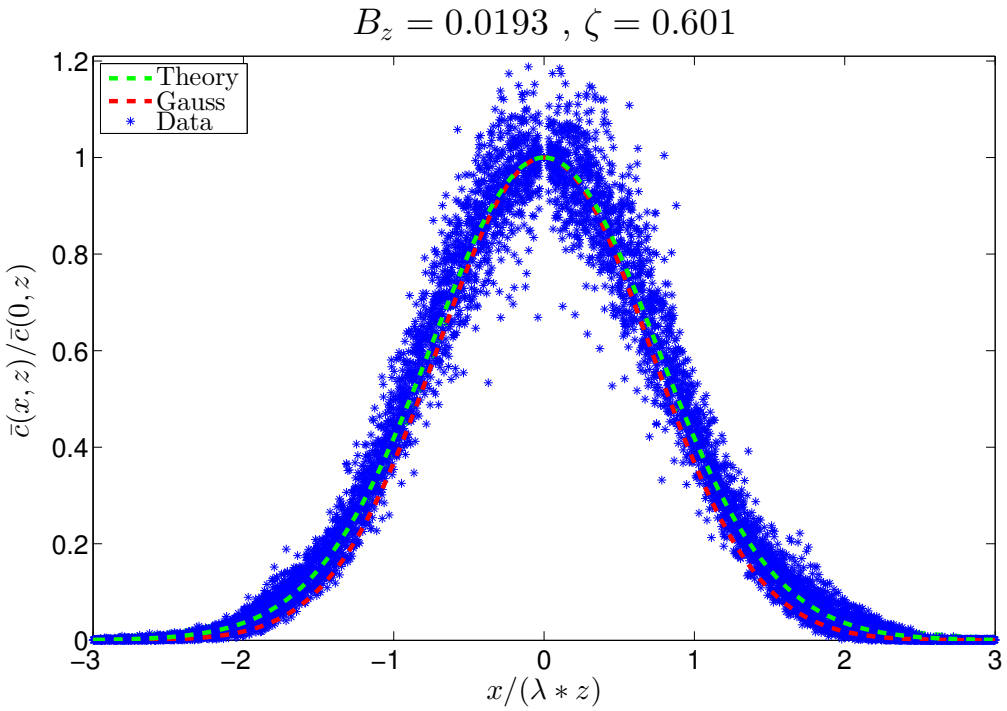


Fig. 4.14 Time averaged concentration along horizontal lines and comparison with the Gaussian and theoretical curve of equation 4.21. Data for exp.30

and imposing the following boundary conditions on $\bar{c_2}(\eta)$:

$$\begin{cases} \bar{c_2}(0) = 0 \\ \bar{c_2}'(0) = 0 \\ \bar{c_2}'(\eta \to \infty) = 0 \end{cases}$$

leading to the solution

$$\bar{c_2}(\eta) = \zeta^{\frac{1+B_z}{2B_z}} (\eta^2 + \zeta)^{-\frac{1+B_z}{2B_z}} \tag{4.21}$$

As shown in figure 4.14 this idealised model is in good accord with the experimental data obtained from measurements of the time averaged concentration across the plume. This result is important as it is a model predicting the mixing and the steady state concentration based on the transverse and longitudinal mixing laws. The Gaussian model, so far used in previous studies, was based on a curve fitting of the experimental data with no theoretical justification. This solution, obtained from the comparison of longitudinal and transversal mixing, using the amplitude and frequency data from eddies, represent an important prediction to agree with the time averaged data.

## 4.7 Conclusions

This chapter investigated mixing within a two dimensional turbulent plume confined between two parallel plates. The flow is controlled by the dynamics of large eddies which form in the plume and migrate downstream, stirring and mixing ambient fluid into the plume. The turbulent dispersion produced by these meandering eddies was explored. This chapter initially focused on the time averaged mixing driven by the turbulence of the rising plume. The time-averaged rise speed and concentration profiles are consistent with results described in previous experimental studies (Kotsovinos and List [39] and Paillat and Kaminski [56]). The investigation of the cross flow mixing has allowed the formulation of a physical law predicting the time-averaged concentration profile of a steady state plume along the streamwise and spanwise direction. This law is consistent with the Gaussian experimental law extensively used in previous literature (Kotsovinos [38] and Morton et al. [53]).

The investigation has then focused on the case of reactive plumes where the reaction time between the two fluids is comparable to the turnover time of the eddies. By parametrising the mixing of the horizontally-averaged concentration of tracer in terms of a longitudinal dispersion coefficient, which depends on the length scale and speed in the flow, $0.02f^{1/3}z$ it was possible to formulate a model for the mixing. This has been tested with experimental data for the horizontal integral of concentration, and in the case that a steady flux of dye is added to a steady plume at $t = 0$, the advance of the dispersing dye front is well modelled by the phenomenological relation. In developing models of reacting plumes in which the reactions may be passive, or may in fact generate buoyancy, for example through the release of thermal energy or production of small bubbles or particulate, quantification of the longitudinal mixing may be key. Equation 4.19 leads to a prediction of the residence time distribution of a passive tracer carried by the plume: the model shows that the standard deviation in the residence time may be a fraction 0.15 of the mean. The results of this project are new and I am not aware of similar studies.

# Chapter 5

# Conclusions

This chapter summarises the main results following my investigation on clay flows (5.1) and on turbulent mixing occurring within plumes (5.2) and proposes some possibilities for future work.

## 5.1 Clay flow

§5.1.1 discuss the main contribution resulting from the study described in chapters 2 and 3 before considering some possible topics for future studies in §5.1.2.

### 5.1.1 Main Contribution

The project develops the current literature with the following outcomes.

**Chapter 2** investigates the gas flow within a non-Newtonian gel, between the liquid and plastic regime. The analysis is based on experimental results where gas (or water) is injected into a two-dimensional domain that is filled with a clay-water mixture and topped by an elastic plate. The flow is strongly affected by both the nature of the fluid injected and the water content of the mixture. Fluid injection into the domain pressurises the clay and thus deforms the domain. However, the yield stress of the clay acts as a threshold, which needs to be overcome by the injection pressure, before the material is deformed.

The deformation of clay during gas injection is initially stable. The pressure deforms the elastic plate and the gas injected is contained within a circular hole at the centre of the domain. Continuous gas injection increases the pressure and expands the size of the central hole, while deforming the elastic top plate. When the pressure overcomes a critical limit ($P_{cr}$, figure 2.12), which depends on the water content within the clay-

water mixture, the deformation becomes unstable. For relatively high water content mixtures, the gas injection forms finger-like channels, which grow in the direction of the boundary. However in low water content mixtures fracture-like channels form. The pressures measured during experiments using compacted clays are significantly higher than the pressures recorded when using high water content mixtures. When a channel opening reaches the boundary of the domain the gas is quickly released, the pressure falls and allows the elastic boundary to relax and the channel to close. The de-pressurisation behaviour depends on the time-scale of the pressure release as compared to the elastic relaxation time of the domain. A relatively slow decrease in pressure allows the system to adjust rapidly to the pressure changes and reach the steady state condition with a constant outflow of gas from the domain. On the other hand, a very fast pressure drop causes a drastic relaxation of the domain which, in the case of compacted clays, causes sealing or clogging of the channel. Once the channel clogs, further gas injection increases the pressure and the phenomenon repeats causing cyclic gas release.

When water is injected the deformation soon becomes unstable forming either finger-like or fracture like channels. The fracturing pressure is similar to the gas injection case, however the fracture and clogging cycle is more frequent and the area involved by the erosion of the material is much wider. The elastic deformation law along with the conservation of mass allow the formulation of a physical model, which is in good agreement with the experimental results (equation 2.8). The model is able to predict the pressurisation of the gas, but is limited to relatively high water content mixtures. Further investigations are required to consider highly compacted material but the results shown using water-rich clay are consistent with other studies where the volume ratio of the clay-water mixture was significantly higher ($S \approx 0.8$). Donohew et al. [22] presents a series of experiments in which gas is injected into several different clay-water samples (including Bentonite) with $0.3 \leq S \leq 0.7$. The gas entry pressure measured during these experiments rises from 11.7 kPa for $S = 0.23$ to 1615 kPa for $S = 0.72$; however, with each successive gas injection cycle they find the gas entry pressure reduces. This data suggests that, as for the case with high water content clays, the high gas pressure fractures the clay and increases the bulk porosity of the sample. When the gas injection is stopped and the pressure decreases the material relaxes and seals the fractures. Future gas injections repeat the fracturing cycle but the gas entry pressure required to expand the fracture channels is lower; this is due to the imperfect resealing of the material as shown in §2. The sealing property of the clay

is of significant interest for waste repository engineering. Furthermore, the cyclic gas release from a clay-water mixture plays a strong role in the eruption of mud volcanoes.

**Chapter 3** explores the flow of clay-water mixtures between the liquid and plastic regime. The flow is driven by pressurisation of the fluid and buoyancy forces from gas injection. This topic is divided into two projects. In the first project, gas is injected at the bottom of a two-dimensional domain filled with clay, and the flow of gas through a wide vertical domain is studied. The second project investigates the flow of clay and gas in a narrow vertical conduit driven by the pressurisation of the mud and gas injected at the base.

The results of the first project are strongly dependent on the water content of the mixture. A relatively high water content clay shows liquid-like properties and the bubbles form a continuous train. The bubbles have similar volumes and rise speed, which remain constant throughout the height of the domain and depend on the water content of the clay. Higher gas injection rates increase the frequency of bubbles and reduce the vertical distance between consecutive bubbles. The passage of a bubble softens the clay and locally reduces its viscosity. This causes an increase in the gas rise speed. Increasing the injection rate above a critical value significantly reduces the vertical distance between bubbles to the point they can be affected by the wake of the preceding bubbles. When a bubble is trapped in the wake of a previous bubble its rise speed increases until the bubbles coalesce. The resulting gas volume is increased but the rise speed is not affected by the coalescence. Relatively low water content mixtures show gel-like properties. The bubbles rising through this type of clay are defined as slugs because of their shape, which is elongated along the vertical direction. A further decrease in the water content of the clay increases the gel-like property of the material. The gas injection requires relatively high pressure for gas to flow through the clay. The gas pressure forms a fracture-like channel which, with constant inflow of gas in the domain, rises from the source and releases the pressure once it reaches the top of the domain. The different regimes of the gas flow through the clay are dependent on the Reynolds number of the gas and the water content of the clay. This description is analogous to some observations of gas bursting eruptions from mud volcanoes.

The second project studies mud eruptions from a narrow conduit driven by pressurisation of clay (reservoir pressure) and the flow of gas at the base of the conduit. The yield stress of the clay impedes the flow along the conduit and the reservoir pressure has to be higher than the yield stress to start an eruption (over-pressured reservoir). The pressure applied on the clay during the eruption softens the clay and the yield stress gradually reduces. Meanwhile the outflow of clay during the eruption

reduces the reservoir pressure. The mud outflow is proportional to the difference between the reservoir pressure and the dynamic yield stress. The eruption persists while the driving pressure is greater than the yield stress. When the pressure reduces below the dynamic yield stress (under-pressured reservoir) the eruption stops and the yield stress increases. The fluctuations of the yield stress and the pressurisation of the reservoir cause cyclic eruptions similar to the eruption pattern of natural mud volcanoes. The gas flow through the conduit generates buoyancy forces which may cause an eruption of clay (under-pressured case) or increase the outflow of clay during an eruption (over-pressured case). The experimental results have shown that in the case that there is a gas flux supplied to the base of the conduit the buoyancy force of the gas acts in addition to the reservoir pressure in determining the driving force for an eruption. The experimental results motivate a numerical model (equation 3.14) which predicts the combined effect of the buoyancy force and the reservoir pressure in driving eruptions of mud volcanoes. My calculations suggest that the gas flow recorded during the eruptions of Lusi (a mud volcano in Indonesia) causes a buoyancy force in the conduit in the range of $10^5 \leq \Delta P_g \leq 10^6$ Pa which almost doubles the rise speed of the mud at the top of the conduit relative to the case in which the reservoir pressure alone drives the eruption.

### 5.1.2 Further Work

Some possible plans for studies following this thesis are listed below:

- Radioactive waste barriers use clay-water mixture with much lower water content compared to the experiment analysed ($S \geq 0.8$). It would be of significant interest to study the pneumatic and hydraulic fracturing of clay mixtures with low water content. It would also be interesting to measure the clay displacement by applying the PTV (Particle tracking velocimetry) technique. The deformation of clay allows to measure the distribution of stress in the mixture, which would be of value when modelling the fracturing processes and the sealing of clay.

- The water content of clay in both nuclear waste barriers and mud volcanoes is frequently inhomogeneous. This thesis has shown the influence of the rheology of clay on the evolution of hydraulic and pneumatic fracturing. It would also be interesting to study the behaviour of a fracture within a stratified environment or through layers of clay with different water content. Further work could also be focused on the joint injection of water and gas into clay media.

- The episodic gas release described in §2 is strongly affected by the elastic relaxation of the top plate once the high gas pressure reduces. In my experiments the volume occupied by the gas expands by elastically deforming the top plate and driving the clay out of the domain. It would be interesting to run some experiments in a rigid cell with an enclosed volume in order to study the evolution of gas penetration in a clay sample, where the volume expansion is hampered by the rigid experimental boundaries.

- The relaxation of the domain and the properties of the clay allow the material to seal once the fracturing pressure is released. The seal is not complete after the pressure is released since a residual fracture remains open in the material. This suggests that it would not be possible to recover the total fluid injected into clay by extraction from the injection point. Cyclic injection and extraction of fluid from the domain would allow to study the fraction of the clay which may be recovered. This result would be relevant for $CO_2$ management and environmental engineering.

- The yield stress of clay has a key control on cyclic gas release and on eruptions from mud volcanoes. Further investigation should focus on the variability of the yield stress depending on the applied stress and time. The yield stress affects both the eruptive and quiescent stages of a mud volcano and would allow more accurate predictions of the eruptive frequency and gas release. The yield stress variations are also a topic of significant interest to measure the longevity and efficiency of the clay engineered shield for waste management solutions.

## 5.2 Turbulent plumes

**Chapter 4** studies the mixing between fluids generated by a buoyancy driven plume. The plume is experimentally reproduced by injecting a dense fluid from the top of a two dimensional domain filled with a lower density fluid. The buoyancy force drives the injected fluid through the domain but the flow is unstable and generates eddies which cause the mixing between the ambient fluid and the plume. The mixing is studied by first colouring the injected fluid with a passive dye, and then measuring the concentration of dye as it evolves throughout the domain. The eddies enlarge and merge while rising and cause the plume to oscillate along the streamwise direction. The time averaged concentration of the plume fluid is the result of the combined effect of the actual mixing and the oscillation caused by the eddies. Hence the frequency and

amplitude of the oscillations allow to track the evolution of eddies along the height of the plume. Finally I process measurements of the horizontally averaged dye concentration to predict the longitudinal mixing caused by the eddies, which is described in terms of a diffusion coefficient in the vertical direction. The steamwise diffusion coefficient is measured by comparison between experimental data and a numerical model. This allows prediction of the residence time of fluid particles within the plume. This value is necessary to predict the result of mixing two relatively slow reagents.

Some possible future work may consider the following topics:

- Chapter 4 analyses the mixing of a plume bounded in a two-dimensional domain. The limits of the experimental apparatus restrict the growth of the eddies to the spanwise/streamwise plane. In a three dimensional domain the eddies would be able also to evolve in the direction normal to the plane. The different evolution of the eddies may affect the speed and mixing coefficients of the plume. The result of a three dimensional apparatus would allow results more representative of volcanic plumes and oceanic flows.

- Buoyancy driven mixing is a subject of interest in reactor engineering, which aims to maximise the efficiency of the mixing between two or more fluids. The products of a chemical reaction depend on the concentration of the reagents and the reaction time. It would be interesting to study the products resulting from mixing two reagents with reaction time comparable to the mixing time of the plume. A ph indicator added to the experimental apparatus in chapter 4 would allow measurement of the extent of the mixing between the two fluids.

- By injecting gas from the bottom of an experimental apparatus similar to the one described in §4 it would be possible to use the dye attenuation technique to measure the turbulent mixing generated by a gas plume. This experimental procedure would allow investigation of the gas-fluid interaction in a turbulent gas plume and modelling of the buoyancy driven rise of particles placed at the bottom of the experimental apparatus. This study would have relevance for topics such as gas plumes from the ocean bed (Woods [83]) and storage of $CO_2$ beneath aquifers (Cevatoglu et al. [13])

# References


[1] Ai, J., Law, A. W.-K., and Yu, S. C. M. (2006). On Boussinesq and non-Boussinesq starting forced plumes. *Journal of Fluid Mechanics*, 558:357–386.

[2] Alfaro, M. C. and Wong, R. C. (2001). Laboratory studies on fracturing of low-permeability soils. *Canadian Geotechnical Journal*, 38(2):303–315.

[3] Baik, M.-H., Cho, W.-J., and Hahn, P.-S. (2007). Erosion of bentonite particles at the interface of a compacted bentonite and a fractured granite. *Engineering Geology*, 91:229–239.

[4] Barry, M. a., Boudreau, B. P., and Johnson, B. D. (2012). Gas domes in soft cohesive sediments. *Geology*, 40(4):379–382.

[5] Beggs, D. H. and Brill, J. P. (1973). A study of two-phase flow in inclined pipes. *Journal of Petroleum technology*, 25(5):607–617.

[6] Besq, A., Malfoy, C., Pantet, A., Monnet, P., and Righi, D. (2003). Physicochemical characterisation and flow properties of some bentonite muds. *Applied Clay Science*, 23(5-6):275–286.

[7] Bonini, M., Rudolph, M. L., and Manga, M. (2016). Long- and short-term triggering and modulation of mud volcano eruptions by earthquakes. *Tectonophysics*, 672-673:190–211.

[8] Boudreau, B. P. (2012). The physics of bubbles in surficial, soft, cohesive sediments. *Marine and Petroleum Geology*, 38(1):1–18.

[9] Bremer, T. S. V. D. and Hunt, G. R. (2014). Two-dimensional planar plumes and fountains. *Journal of Fluid Mechanics*, 750:210–244.

[10] Brown, R. C. (1999). A multiple front propagation model for gas migration through clay. *Engineering Geology*, 54:151–158.

[11] Buffett, B. A. (2000). Clathrate hydrates. *Annual review of earth and planetary sciences*, 28(1):477–507.

[12] Carazzo, G., Kaminski, E., and Tait, S. (2008). On the rise of turbulent plumes: Quantitative effects of variable entrainment for submarine hydrothermal vents, terrestrial and extra terrestrial explosive volcanism. *Journal of Geophysical Research*, 113(B9):1–19.

[13] Cevatoglu, M., Bull, J. M., Vardy, M. E., Gernon, T. M., Wright, I. C., and Long, D. (2015). Gas migration pathways, controlling mechanisms and changes in sediment acoustic properties observed in a controlled sub-seabed $CO_2$ release experiment. *International Journal of Greenhouse Gas Control*, 38:26–43.

[14] Chang, M. and Huang, R.-c. (2015). Observations of hydraulic fracturing in soils through field testing and numerical simulations. *Canadian Geotechnical Journal*, 52:1–17.

[15] Chen, B. D. and Jirka, G. H. (1999). LIF study of plane jet bounded in shallow water layer. *Journal of Hydraulic Engineering*, 125(August):817–826.

[16] Cramer, J. J. and Smellie, J. A. (1994). Final report of the AECL/SKB Cigar Lake analog study. Technical Report 17, Atomic Energy of Canada Ltd. (AECL–10851). Canada, Chalk River.

[17] Cui, Y. J., Yahia-Aissa, M., and Delage, P. (2002). A model for the volume change behavior of heavily compacted swelling clays. *Engineering Geology*, 64:233–250.

[18] Danckwerts, P. V. (1953). Continuous Flow Systems, Distribution of Residence Times. *Chemical Engineering Science*, 2(1):1–13.

[19] Daoyi, C. and Jirka, G. H. (1998). Linear stability analysis of turbulent mixing layers and jets in shallow water layers. *Journal of Hydraulic Research*, 36(5):815–830.

[20] Delage, P., Cui, Y., and a.M. Tang (2010). Clays in radioactive waste disposal. *Journal of Rock Mechanics and Geotechnical Engineering*, 2(2):111–123.

[21] Dimitrov, L. I. (2002). Mud volcanoes-the most important pathway for degassing deeply buried sediments. *Earth-Science Reviews*, 59(1-4):49–76.

[22] Donohew, A., Horseman, S. T., and Harrington, J. F. (2000). Gas entry into unconfined clay pastes at water contents between the liquid and plastic limits. *Environmental Mineralogy: Microbial Interactions, Anthropogenic Influences, Contaminated Land and Waste Management.*, pages 81–106.

[23] Dracos, T., Giger, M., and Jirka, G. H. (1992). Plane turbulent jets in a bounded fluid layer. *Journal of Fluid Mechanics*, 241:587–614.

[24] Feseker, T., Boetius, A., Wenzhöfer, F., Blandin, J., Olu, K., Yoerger, D. R., Camilli, R., German, C. R., and de Beer, D. (2014). Eruption of a deep-sea mud volcano triggers rapid sediment movement. *Nature communications*, 5:5385:1–8.

[25] Fischer, H. B. (1973). Longitudinal dispersion and turbulent mixing in open-channel flow. *Annual Review of Fluid Mechanics*, 5:59–78.

[26] Graham, J., Halayko, K. G., Hume, H., Kirkham, T., Gray, M., and Oscarson, D. (2002). A capillarity-advective model for gas break-through in clays. *Engineering Geology*, 64:273–286.

[27] Gutierrez-Rodrigo, V., Villar, M. V., Martin, P. L., Romero, F. J., and Barcala, J. M. (2015). Gas-breakthrough pressure of FEBEX bentonite. In Shaw, R., editor, *Geological Society, London, Special Publications*, volume 415, pages 47–57.

[28] Haberman, W. L. and Morton, R. K. (1953). An experimental investigation of the drag and shape of air bubbles rising in various liquids. Technical report, Defence Technical Information Center, Washington DC.

[29] Harrington, J. F. and Horseman, S. T. (1999). Gas transport properties of clays and mudrocks. In Aplin, A. C., Fleet, A. J., and MacQuaker, J. H. S., editors, *Geological Society, London, Special Publications*, volume 158, pages 107–124.

[30] Holtzman, R., Szulczewski, M. L., and Juanes, R. (2012). Capillary fracturing in granular media. *Physical review letters*, 108(26):264504.1–264504.4.

[31] Horseman, S. T., Harrington, J. F., and Sellin, P. (1999). Gas migration in clay barriers. *Engineering Geology*, 54:139–149.

[32] Hovland, M., Hill, A., and Stokes, D. (1997). The structure and geomorphology of the Dashgil mud volcano, Azerbaijan. *Geomorphology*, 21(1):1–15.

[33] Kawatra, S. K. and Ripke, S. J. (2001). Developing and understanding the bentonite fiber bonding mechanism. *Minerals Engineering*, 14(6):647–659.

[34] Komine, H. and Ogata, N. (1996). Prediction for swelling characteristics of compacted Bentonite. *Canadian Geotechnical Journal*, 33(1):11–22.

[35] Komine, H. and Ogata, N. (1999). Experimental study on swelling characteristics of sand-bentonite mixture for nuclear waste disposal. *Soils and foundations*, 39(2):83–97.

[36] Kopf, A., Delisle, G., Faber, E., Panahi, B., Aliyev, C. S., and Guliyev, I. (2010). Long-term in situ monitoring at Dashgil mud volcano, Azerbaijan: A link between seismicity, pore-pressure transients and methane emission. *International Journal of Earth Sciences*, 99(SUPPL. 1):227–240.

[37] Kopf, A. J. (2002). Significance of mud volcanism. *Reviews of Geophysics*, 40(2):1–52.

[38] Kotsovinos, N. E. (1977). Plane turbulent buoyant jets . Part 2 . Turbulence structure. *Journal of Fluid Mechanics*, 81:45–62.

[39] Kotsovinos, N. E. and List, E. J. (1977). Plane turbulent buoyant jets . Part 1 . Integral properties. *Journal of Fluid Mechanics*, 81(1):25–44.

[40] Krishna, R. and Van Baten, J. M. (1999). Rise characteristics of gas bubbles in a 2D rectangular column: VOF simulations vs experiments. *International Communications in Heat and Mass Transfer*, 26(7):965–974.

[41] Lagaly, G. (1989). Principles of flow of kaolin and bentonite dispersions. *Applied Clay Science*, 4(2):105–123.

[42] Landel, J. R., Caulfield, C. P., and Woods, A. W. (2012a). Meandering due to large eddies and the statistically self-similar dynamics of quasi-two-dimensional jets. *Journal of Fluid Mechanics*, 692:347–368.

[43] Landel, J. R., Caulfield, C. P., and Woods, A. W. (2012b). Streamwise dispersion and mixing in quasi-two-dimensional steady turbulent jets. *Journal of Fluid Mechanics*, 711:212–258.

[44] Li, Y. (2000). Buoyancy-driven natural ventilation in a thermally stratified one-zone building. *Building and Environment*, 35(3):207–214.

[45] List, E. J. (1982). Turbulent Jets and Plumes. *Annual Review of Fluid Mechanics*, 14(1):189–212.

[46] Madsen, F. T. (1998). Clay mineralogical investigations related to nuclear waste disposal. *Clay Minerals*, 33:109–129.

[47] Manga, M. and Bonini, M. (2012). Large historical eruptions at subaerial mud volcanoes, Italy. *Natural Hazards and Earth System Science*, 12(11):3377–3386.

[48] Marques, F. O. (2001). Flow and fracturing of clay: Analogue experiments in bulk pure shear. *Memoirs-Geological Society of America*, 193:261–270.

[49] Marschall, P., Horseman, S., and Gimmi, T. (2005). Characterisation of gas transport properties of the opalinus clay, a potential host rock formation for radioactive waste disposal. *Science And Technology*, 60(1):121–139.

[50] Mazzini, A., Svensen, H., Akhmanov, G. G., Aloisi, G., Planke, S., Malthe-Sørenssen, A., and Istadi, B. (2007). Triggering and dynamic evolution of the LUSI mud volcano, Indonesia. *Earth and Planetary Science Letters*, 261(3-4):375–388.

[51] Milkov, A. V., Sassen, R., Apanasovich, T. V., and Dadashev, F. G. (2003). Global gas flux from mud volcanoes: A significant source of fossil methane in the atmosphere and the ocean. *Geophysical Research Letters*, 30(2):17–20.

[52] Morton, B. R. (1959). Forced plumes. *Journal of Fluid Mechanics*, 5(01):151–163.

[53] Morton, B. R., Taylor, G., and Turner, J. S. (1956). Turbulent Gravitational Convection from Maintained and Instantaneous Sources. *Proceedings of the Royal Society A: Mathematical, Physical and Engineering Sciences*, 234(1196):1–23.

[54] Murton, B. J. and Biggs, J. (2003). Numerical modelling of mud volcanoes and their flows using constraints from the Gulf of Cadiz. *Marine Geology*, 195(1-4):223–236.

[55] Oliemans, R. V., Pots, B. F., and Trompé, N. (1986). Modelling of annular dispersed two-phase flow in vertical pipes. *International Journal of Multiphase Flow*, 12(5):711–732.

[56] Paillat, S. and Kaminski, E. (2014). Entrainment in plane turbulent pure plumes. *Journal of Fluid Mechanics*, 755:R2.1–R2.11.

[57] Papanicolaou, P. N. and List, E. J. (1988). Investigations of round vertical turbulent buoyant jets. *Journal of Fluid Mechanics*, 195(-1):341–391.

[58] Paterson, L. (1985). Fingering with miscible fluids in a Hele Shaw cell. *Physics of Fluids*, 28(1):26–30.

[59] Pioli, L., Bonadonna, C., Azzopardi, B. J., Phillips, J. C., and Ripepe, M. (2012). Experimental constraints on the outgassing dynamics of basaltic magmas. *Journal of Geophysical Research: Solid Earth*, 117(3):1–17.

[60] Poletto, F. B. and Miranda, F. (2004). *Seismic while drilling: Fundamentals of drill-bit seismic for exploration.* vol 35, Elsevier, Amsterdam.

[61] Pope, S. B. (2000). *Turbulent flows*. Cambridge University Press, Cambridge.

[62] Prandtl, L. (1925). Bericht uber Untersuchungen zur ausgebildeten Turbulenz. *Zeitschrift fur angewandte Mathematik und Mechanik*, 5(2):136–139.

[63] Prandtl, L. (1954). *Essentials of fluid dynamics*. Blackie, London.

[64] Pusch, R. (1992). Use of Bentonite for isolation of radioactive waste products. *Clay Minerals*, 27:353–361.

[65] Pusch, R., Kasbohm, J., and Thao, H. T. M. (2010). Chemical stability of montmorillonite buffer clay under repository-like conditions — A synthesis of relevant experimental data. *Applied Clay Science*, 47(1):113–119.

[66] Rudolph, M. L. and Manga, M. (2012). Frequency dependence of mud volcano response to earthquakes. *Geophysical Research Letters*, 39(14):1–5.

[67] Rudolph, M. L., Shirzaei, M., Manga, M., and Fukushima, Y. (2013). Evolution and future of the Lusi mud eruption inferred from ground deformation. *Geophysical Research Letters*, 40(6):1089–1092.

[68] Saffman, P. G. and Taylor, G. (1958). The Penetration of a Fluid into a Porous Medium or Hele-Shaw Cell Containing a More Viscous Liquid. *Proceedings of the Royal Society A: Mathematical, Physical and Engineering Sciences*, 245(1242):312–329.

[69] Sellin, P. and Leupin, O. X. (2013). The Use of Clay as an Engineered Barrier in Radioactive-Waste Management – A Review. *Clays and Clay Minerals*, 61(6):477–498.

[70] Shao, H., Wenjie, X., Marschall, P., Kolditz, O., and Hesser, J. (2015). Numerical interpretation of gas-injection tests at different scales. In Shaw, R. P., editor, *Geological Society, London, Special Publications*, volume 415, pages 203–212.

[71] Shaw, R. P. (2015). *Gas generation and migration in deep geological radioactive waste repositories*, volume 415. Geological Society of London, London.

[72] Shen, S.-L. and Miura, N. (1999). Soil Fracturing of the Surrounding Clay during Deep Mixing Column Installation. *Soils and foundations, Japanese Geotechnical Society*, 39(5):13–22.

[73] Shirzaei, M., Rudolph, M. L., and Manga, M. (2015). Deep and shallow sources for the Lusi mud eruption revealed by surface deformation. *Geophysical Research Letters*, 42(13):5274–5281.

[74] Talaia, M. A. R. (2007). Terminal Velocity of a Bubble Rise in a Liquid Column. *World Academy of Science, Engineering and Technology*, 1(4):220–224.

[75] Taylor, G. (1954). The dispersion of matter in turbulent flow through a pipe. *Proc. R. Soc. Lond.*, 223:446–468;.

[76] Timoshenko, S. and Woinowsky-Krieger, S. (1959). *Theory of Plates and Shells*. Mc Graw-Hill, 2 edition.

[77] Tran, A., Rudolph, M. L., and Manga, M. (2015). Bubble mobility in mud and magmatic volcanoes. *Journal of Volcanology and Geothermal Research*, 294:11–24.

[78] Turner, J. S. (1979). *Buoyancy Effects in Fluids*. Cambridge University Press, Cambridge.

[79] Turner, J. S. (1986). Turbulent entrainment: the development of the entrainment assumption, and its application to geophysical flows. *Journal of Fluid Mechanics*, 173:431–471.

[80] Vanderkluysen, L., Burton, M. R., Clarke, A. B., Hartnett, H. E., and Smekens, J. F. (2014). Composition and flux of explosive gas release at LUSI mud volcano (East Java, Indonesia). *Geochemistry, Geophysics, Geosystems*, 15(7):2932–2946.

[81] Vanderwel, C. and Tavoularis, S. (2014). Measurements of turbulent diffusion in uniformly sheared flow. *Journal of Fluid Mechanics*, 754:488–514.

[82] Vona, A., Giordano, G., De Benedetti, A. A., D'Ambrosio, R., Romano, C., and Manga, M. (2015). Ascent velocity and dynamics of the Fiumicino mud eruption, Rome, Italy. *Geophysical Research Letters*, 42(15):6244–6252.

[83] Woods, A. W. (2010). Turbulent Plumes in Nature. *Annual Review of Fluid Mechanics*, 42(1):391–412.

[84] Yih, C.-S. (1977). Turbulent Buoyant Plumes. *Physics of Fluids*, 20(8):1234–1237.

[85] Zoporowski, A. and Miller, S. A. (2009). Modelling eruption cycles and decay of mud volcanoes. *Marine and Petroleum Geology*, 26(9):1879–1887.